UM HE 77-32

NEUTRAL STRANGE PARTICLE PRODUCTION FROM NUCLEAR TARGETS BY 300 GEV PROTONS

by
Patrick Louis Skubic

A dissertation submitted in partial fulfillment
of the requirements for the degree of
Doctor of Philosophy
(Physics)
in The University of Michigan
1977

Doctoral Committee:

Professor Oliver E. Overseth, Chairman
Professor Michael J. Longo
Professor Richard H. Sands
Professor Richard L. Sears
Professor Yukio Tomozawa

TABLE OF CONTENTS

ABSTRACT

NEUTRAL STRANGE PARTICLE PRODUCTION

FROM NUCLEAR TARGETS BY 300 GEV PROTONS

by

Patrick Louis Skubic

Chairman: Oliver E. Overseth

300 GeV protons were used to produce Λ^0 and $\bar{\Lambda}^0$ hyperons and K^0_S mesons from beryllium, copper, and lead targets in the Fermilab neutral hyperon beam. The Lorentz invariant inclusive cross sections ($Ed^3\sigma/d\vec{p}^3$) in the projectile fragmentation region, $0.2<x<1.0$, $0<p_T<2$ GeV/c, are presented as functions of $x=p^*_L/p^*_{max}$, p_T and target.

The neutral strange particles were detected by a conventional magnetic spectrometer and the data sample consisted of 1.1×10^6 Λ^0's, 9.4×10^4 K^0_S's, and 1.7×10^4 $\bar{\Lambda}^0$'s.

The target dependence of the invariant cross section was found to be consistent with a power law which was used to perform an extrapolation to A=1. Significant differences were observed in the x distributions for the three targets.

The data were fit to a function of x and p_T to facilitate comparison with other experiments. Fits were also performed to a phenomenological function predicted by the triple Regge Model. The model calculation was found to be consistent with the lambda production data in the region of phase space where the calculation is expected to be valid.

ACKNOWLEDGEMENTS

I would like to thank Oliver Overseth for his continuous support and advice during my research work at Michigan. His encouragement has aided considerably in my development in physics.

Many people have worked on this experiment and all have made valuable contributions. Our co-workers were G. Bunce, R. Handler, R. March, P. Martin, M. Sheaff, and L. Pondrom from the University of Wisconsin; T. Devlin, B. Edelman, R. Edwards, J. Norem, L. Schachinger, and P. Yamin from Rutgers University; and K. Heller from Michigan. G. Ott and E. Behr from Wisconsin were responsible for the design and construction of much of the apparatus.

The experiment would not have been possible without the cooperation and support of the Meson Laboratory personel at Fermilab. I would like to thank C. Brown and the members of the operations crew and all the people at the Meson Laboratory.

I also wish to thank D. Gustafson, L. Jones, and M. Longo here at Michigan for the opportunity to obtain valuable experience in preparation for my thesis project.

I would like to express my deep appreciation to A. R. Long for invaluable aid in the preparation of this manuscript.

LIST OF FIGURES

LIST OF TABLES

LIST OF APPENDICES

CHAPTER I

INTRODUCTION

The collection of known subnuclear particles includes baryons with non-zero strangeness, called hyperons. The historical trend in high energy physics has been to use electron, muon, and neutrino beams to probe weak and electromagnetic interactions while using non-strange baryon and meson beams to probe strong interactions. The advent of higher energy particle accelerators has now made possible the construction of secondary hyperon and antihyperon beams which can be used as strangeness carrying particle probes.

A hyperon beam is practical at current high energy particle accelerators because the relativistic Lorentz time dilation becomes substantial in the laboratory frame. Thus a typical hyperon with a lifetime of the order of 10^{-10} seconds, a mass of the order of 1 GeV, and a laboratory momentum of 200 GeV/c will travel an average distance of 6 meters in the laboratory before decaying. Traversal of some of this distance in a magnetic field allows the hyperons to be physically separated from other stable charged particles and on decay their identity can be determined. The requirements for constructing a hyperon beam are:

1) A high energy (>20 GeV), high intensity (>10^6 particles/pulse) primary hadron beam which is well localized

in cross sectional area.

2) A collimator system and sweeping magnet which separates produced hyperons from other produced particles.

3) A detector system which determines the identity of the hyperon particles.

The construction of a neutral hyperon beam has several technical advantages over a charged hyperon beam. A magnetic field can be used to sweep all charged particles out of the neutral beam. The neutral hyperons can easily be distinguished from other neutral particles such as neutrons, K^0 mesons, and gamma rays by the observation of their decay products. The neutral beam contains the entire momentum spectrum of produced neutral hyperons and neutral K mesons.

The existence of hyperon beams offers the opportunity to investigate the roles of strangeness and baryon number in strong, weak, and electromagnetic interactions. The following experiments could be done in the realm of strong interactions:[1]

1) measurement of the energy dependence of hyperon-nucleon cross sections,

2) tests of relations between hyperon-nucleon total cross sections which are predicted by the additive quark model,

3) searches for missing strange resonances predicted by SU(3) symmetry,

4) investigation of the role of strangeness in high

transverse momentum processes by inclusive experiments,

5) searches for new particles such as charmed baryons.

Many experiments in weak interactions could be performed with hyperon beams such as:

1) the measurement of decay parameters in the weak decay of hyperons,

2) tests of empirical selection rules such as $\Delta S<2$ and $|\Delta I|=1/2$ in weak decays, and

3) the measurement of weak interaction coupling constants in semileptonic decays.

In addition polarized hyperon beams could be used to measure hyperon magnetic moments.

A short lived neutral beam designed to study CP violation in K_S^0 decay has been constructed at CERN. Neutral particles were produced by an external proton beam with a momentum of 24 GeV/c and were observed at a production angle of 75 milliradians(mr). Hyperon experiments performed were a search for $\Delta S=2$ decays of neutral Ξ hyperons,[2] measurement of the $\Lambda^0 p^3$ and $\bar{\Lambda}^0 p^4$ total cross sections, a measurement of the Σ^0 lifetime via the Primakoff effect,[5] and a measurement of the Λ^0 and Ξ^0 lifetimes.[6]

Charged negative hyperon beams have been constructed at CERN with a 24 GeV/c incident proton beam and at Brookhaven National Laboratory with an incident proton beam momentum of 29 GeV/c. These beams have been used to measure negative

hyperon production cross sections,[7-10] elastic and total cross sections of negative hyperons on protons and deuterons,[11-13] and to study leptonic decays of negative hyperons.[14,16] A charged hyperon beam is now running at CERN with 200 GeV/c incident protons and at Fermi National Accelerator Laboratory (FNAL) a 400 GeV/c beam has been proposed.

The first results from a neutral hyperon facility at FNAL will be presented here. The first step in the use of a new particle beam is to measure the yield of produced particles. This type of measurement is useful not only to determine rates and backgrounds for future experiments but also for theoretical reasons. It is generally difficult to observe all the particles involved in a high energy reaction where the average multiplicity is large (≈10 at 200 GeV). Therefore knowledge about "inclusive" reactions of the type a+b→c+X, where X stands for unobserved particles, can be used in conjunction with "exclusive" reactions, where all particles in the final state are observed, in order to make more rapid progress. The study of inclusive reactions has increased our knowledge of particle interactions considerably.

From observation of particle production in pp and πp interactions, the following results have emerged:[17]

1) Most produced particles are pions.

2) The average transverse momentum of secondaries is

limited (<400 MeV/c) and the transverse momentum distribution is approximately independent of longitudinal momentum and energy.

3) The average multiplicity of secondaries increases slowly with energy.

4) When the produced particle is the same as the projectile, the longitudinal momentum distribution exhibits a "leading particle effect" and extends up to the incident momentum.

The charged particle multiplicity in π^--nucleus collisions at 100 and 175 GeV/c has been observed to increase only slowly with the atomic mass number (A) of the target nucleus with the increase occurring almost exclusively at large production angles.[18] This result is in disagreement with a naive intranuclear cascade model which would predict a rapid increase in the multiplicity with A.[19] The importance of hadron-nucleus collisions in obtaining information about the space-time structure of high energy particle collisions was emphasized by K. Gottfried in his attempt to explain the weak dependence of the multiplicity on A.[20] A number of other models have also been suggested to explain this result.[21-23] In hadron production in proton-nucleus collisions at energies from 200 to 400 GeV the cross section was observed to become more nearly proportional to the number of nucleons present in the nucleus as the transverse momentum increases.[24] This suggests that processes at high transverse momentum might be

associated with rare short-time constituent interactions.[24]

The longitudinal momentum distribution of the secondary in inclusive production can be qualitatively separated into three regions for the purpose of interpreting experimental results. The forward (backward) region near the maximum (minimum) longitudinal momentum can be associated with fragmentation of the projectile (target) into a relatively small number of secondary particles.[17] The "central" region near zero longitudinal momentum is typically populated by a pion cloud of relatively high multiplicity. The process which produces the low energy pion cloud in the central region is often called "pionization." If these ideas are correct one might expect that the projectile (target) fragmentation region distribution is independent of target (projectile) particle and that the central region distribution is independent of either projectile or target particle.[17]

Certain theoretical analyses have led to the "scaling" hypotheses by Feynman[25] that in the limit of high energy the Lorentz invariant differential cross section becomes independent of energy and is a function only of the transverse momentum of the produced particle, p_T, and of $x=p_L^*/p_{max}^*$. Here p_L^* is the center of mass (CM) longitudinal momentum of the produced particle and p_{max}^* is the CM momentum of the incident particle. Recent data on pp interactions indicates that at 24 GeV/c the scaling limit

has been reached for π^+, π^-, K^+, and p production but not for K^- or $\bar{p}$ production.[26]

Many theoretical models have been proposed to explain particle production. The main classes of theoretical models can be summarized as follows:[26]

1) Models incorporating bremsstrahlung-like emission of low energy particles have been discussed.[27]

5) The statistical model of Fermi[28] has led to thermodynamic models such as that of Hagedorn and Ranft.[29] The hydrodynamical approach initiated by Landau[30] has been further investigated.[31]

3) Multiperipheral models have been proposed[32] and Regge pole analyses[33] have been applied to inclusive reactions. The application of a generalized optical theorem by Mueller[34] relates the inclusive cross section to a discontinuity in the forward three-body scattering amplitude and leads to interesting predictions.

4) Two component models[35] which apply both diffractive[36] and multiperipheral processes to multiparticle production have been discussed.

5) Field theoretical models have been investigated by Cheng and Wu.[37]

6) Parton models have evolved from the interpretation of hadrons as composite entities made up of constituents such as quarks.[38]

Although there are many theoretical models which deal with inclusive reactions, none give a completely satisfactory

explanation of the data.[26]

The results which will be presented here include the first high statistics measurement of the x and p_T dependence of the inclusive cross section for Λ^0 and K_S^0 production by 300 GeV/c protons incident on Be, Cu, and Pb targets in the kinematic range $p_T<2$ and $0.2<x<1.0$. The first high statistics, high energy measurement of $\bar{\Lambda}^0$ production and an investigation of the dependence of the Λ^0 and K_S^0 inclusive cross section on nuclear target as a function of x and p_T will also be presented. Fits of the data to an empirical function were performed to aid in its presentation and the data will be interpreted with the help of fits to phenomenological functions including one predicted by a Mueller-Regge analysis.[39]

CHAPTER II

THE APPARATUS

A. Incident Proton Beam

The experiment was done in the diffracted proton beam in the Meson Laboratory at FNAL. The primary 300 GeV/c proton beam was transported to the Meson Laboratory production target and diffracted protons were used to form one of the secondary beams at a production angle of 1 mr.

The hyperon production target was located at the second focus which was 1480 feet from the Meson Laboratory production target. The size of the proton beam spot at the first focus was monitored by a segmented wire ion chamber with 1 mm wire spacing and at the second focus by two scintillation counters which were 1.27 cm and 0.635 cm in diameter. Adjacent to the proton counters was a halo counter with a hole in its center which was 0.635 cm in diameter. The proton and halo counters were held together in an aluminum frame to maintain their relative alignment and were located 1.59 meters upstream of the hyperon production target. They were centered on the 4 mm diameter defining collimator and served as a monitor of the number of incident protons which hit the hyperon production target which was also 0.635 cm in diameter. For most runs 85% to 90% of the beam was contained within the area of the 0.635

cm proton counter.

The intensity of the incident proton beam was monitored by an argon filled ion chamber with an active area of 8 cm which was located 1.42 meters upstream of the target. The ion chamber was calibrated with the proton counters at low beam intensities.

Two dipole bending magnets with a vertex plane 5.47 meters upstream of the target were used to deflect the incident proton beam to give non-zero production angles. The incident proton beam direction was monitored by two multi-wire proportional chambers which were located between the neutral production target and the two bending magnets. During the course of the experiment, the proton beam was deflected both horizontally and vertically and data were taken at production angles between -2 mr and +9 mr.

B. The Neutral Beam

The hyperon production targets, 0.635 cm in diameter cylinders, were made of Be, Cu, and Pb, and were 1/2 interaction length long (15.32, 4.64, and 4.92 cm respectively). Some data were taken with 1/4 interaction length Be and Cu targets to determine the target absorption correction for the production data. The centers of the targets were aligned with the center of the defining collimator in a rotatable styrofoam holder and the targets were lengthwise centered 14 cm upstream of the entrance of

the collimator system.

The collimator system was housed in a 5.4 meter sweeping magnet which deflected the incident proton beam, charged secondaries and muons out of the neutral channel. The magnetic field in the sweeper was 23 kilogauss during most data taking and pointed either up or down.

The collimator system which was made of steel, brass, and hevimet consisted of three sections, a 254 cm long precollimator, a 56 cm long defining collimator, and a 217 cm long shadow collimator. The collimator system is shown in Figure 1. The defining collimator was 4 mm in diameter and its downstream end was 3.23 meters from the production target so the solid angle acceptance defined by the collimator was:

$\pi(0.002)^2/(3.23)^2$=1.20 microsteradians.

The result of a Monte Carlo calculation showing the variation of the solid angle with lateral displacement from the beam line axis at a point 20 cm upstream from the precollimator entrance is shown in Figure 2. The solid angle calculated from geometry is expected to be inaccurate due to penetration of produced particles through the edge of the defining collimator. The error in the solid angle due to this effect was estimated to be less then 10%.

The neutral beam consisted of γ's, neutrons, $\bar{n}$'s, Λ^0's, K_S^0's, K_L^0's, Ξ^0's, $\bar{\Lambda}^0$'s, and $\bar{\Xi}^0$'s. At a proton beam intensity of 10^7 protons/pulse, the hyperon yields

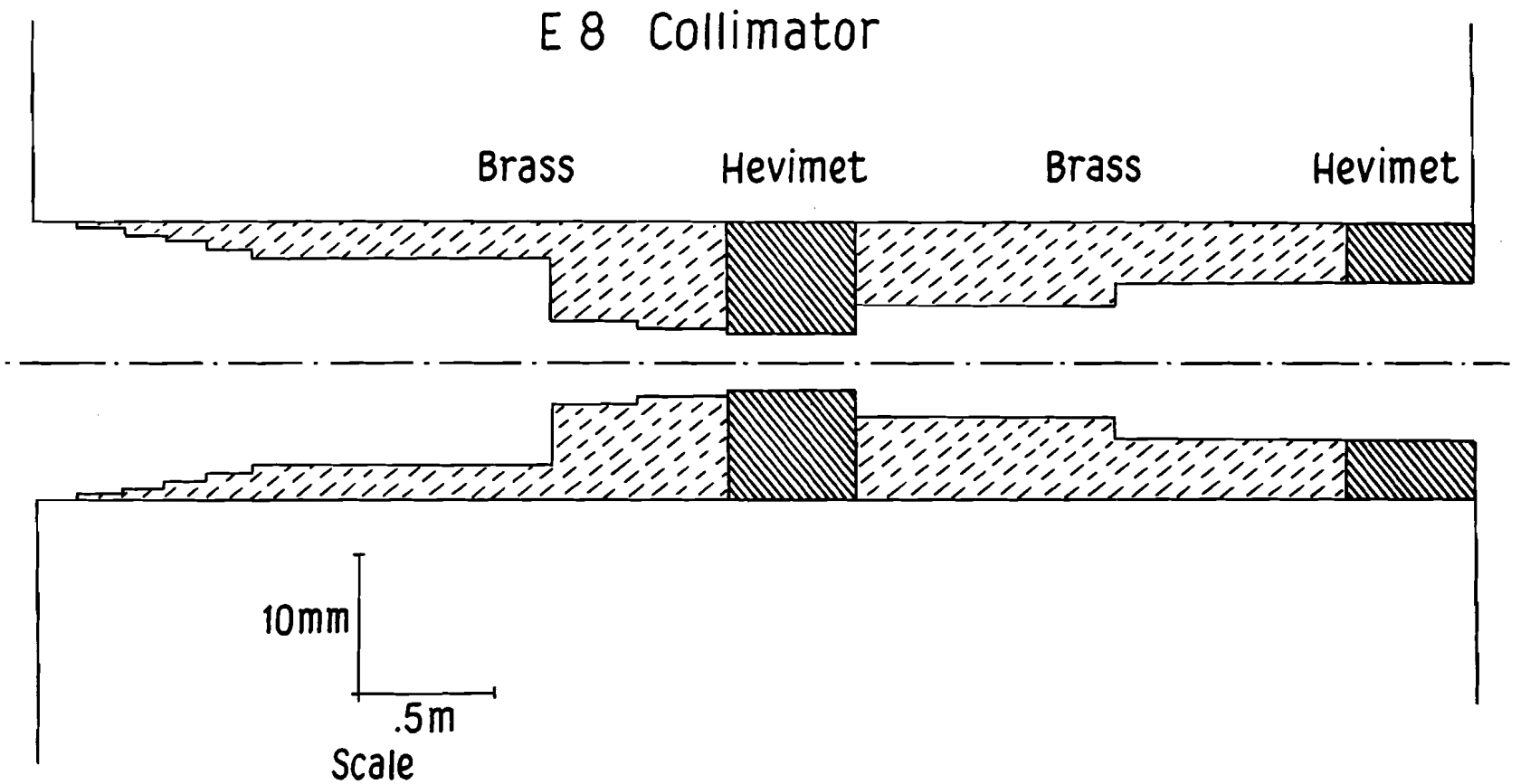

Fig. 1. The neutral beam collimator.

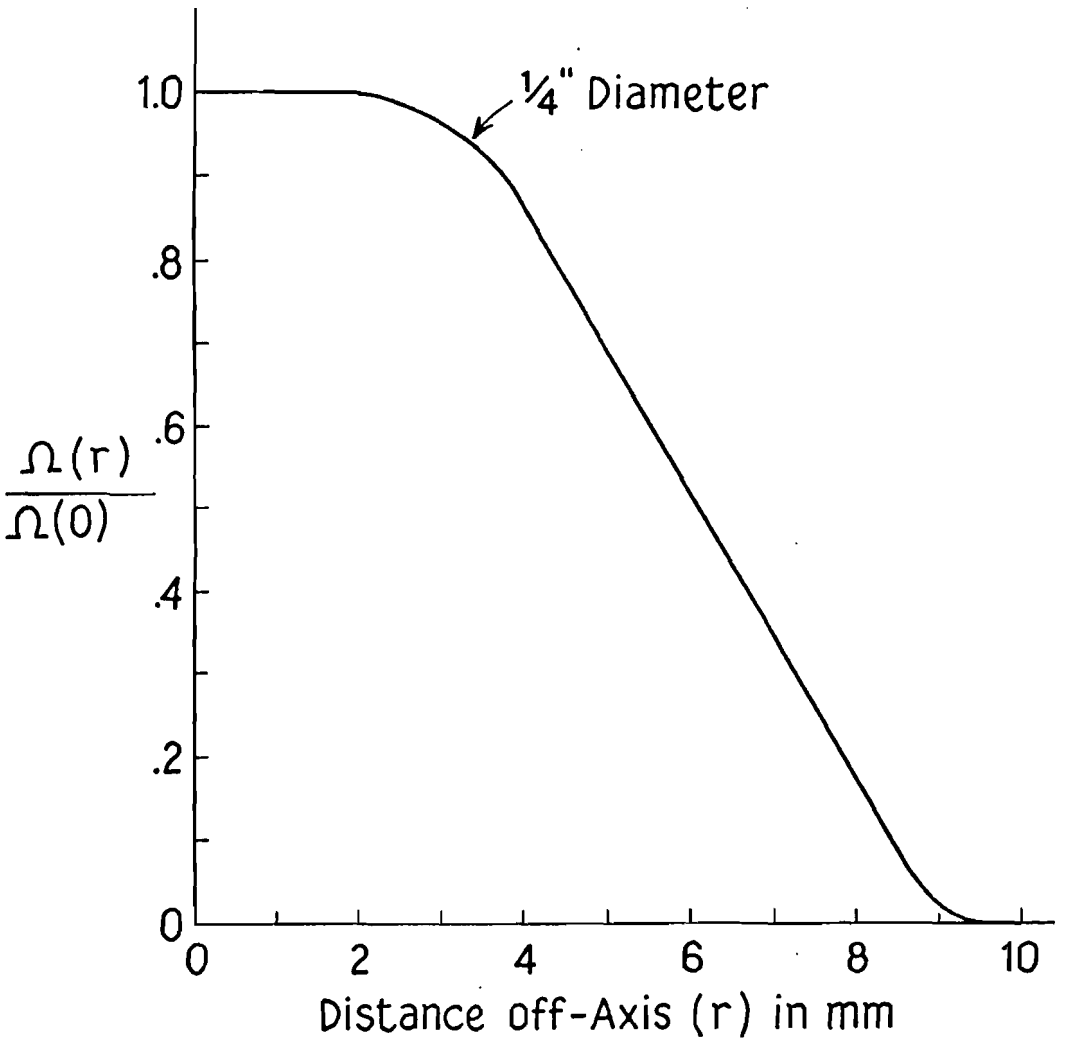

Fig. 2. Results of a Monte carlo calculation showing the change in solid angle acceptance versus off-axis distance at target position.

detected by the spectrometer at a production angle of 0.6 mr were 400 lambdas/pulse, 45 K_S^0's/pulse, 5 $\bar{\Lambda}^0$'s/pulse and 0.2 Ξ^0's/pulse.

The flux in the neutral beam was monitored by a scintillator, steel, lead glass array which was located at the far downstream end of the experimental area. Figure 3 shows the configuration of this neutral monitor. The following signals from the neutral monitor were scaled and were read out between pulses:

$$n=\bar{P}\bar{b}\bar{G}\bar{2}\cdot PbG3,$$

$$\gamma=\bar{V}\cdot c_1\cdot c_2,$$

$$n\gamma=PbG1.$$

Assuming the n monitor counts only neutron interactions with an efficiency which can be calculated from the lengths of the detectors and absorbers, and the $n\gamma$ monitor counts both neutrons and γ's, it is possible to determine the number of neutrons and γ's in the neutral beam. The yield was estimated to be on the order of 20,000 n's/pulse and 30,000 γ's/pulse at 0.6 mr.

C. The Spectrometer

Figure 4 shows the layout of the hyperon spectrometer. The spectrometer consisted of three multiwire proportional chambers (MWPC's) upstream of the superconducting analyzing magnet and three MWPC's downstream of the analyzing magnet. Chamber 6 which was smaller than chamber 5 was used to

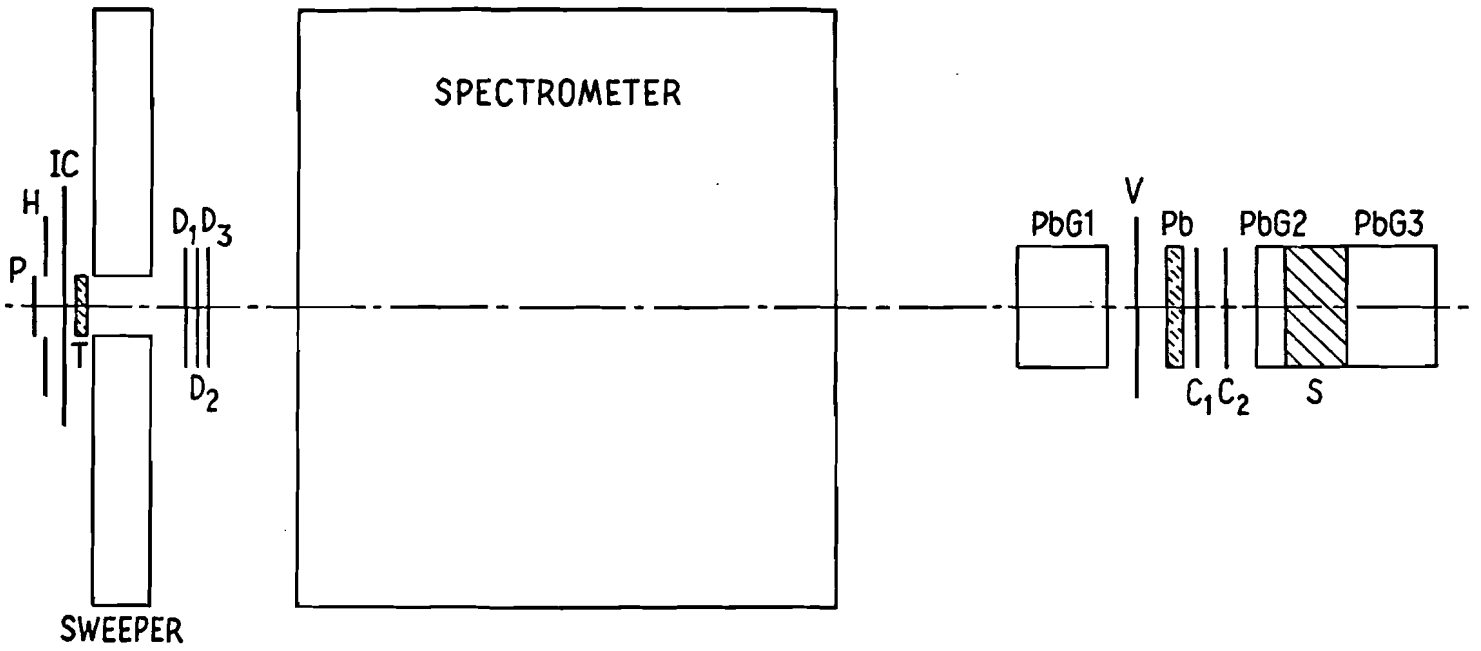

P: ¼" Diameter Counter
H: Counter with ¼" Hole
IC: Ion Chamber
T: Target
D: Counters

PbG: Lead Glass Block
V, C_1, C_2: Counters
Pb: ½" Lead
S: 12" Steel

Fig. 3. The beam monitoring system. (Not to scale.)

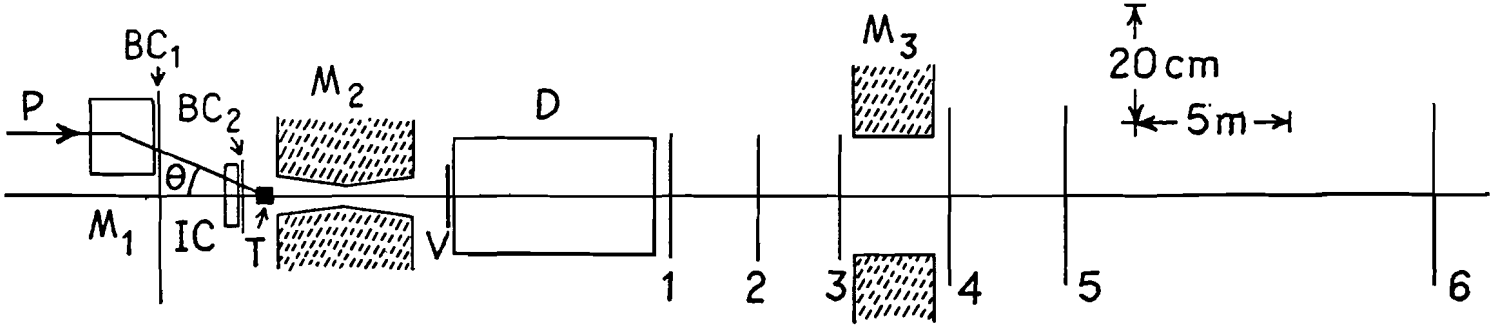

Fig. 4. The layout of the spectrometer.

improve the momentum resolution in the tracks of high momentum protons from Λ^0 decay. Each chamber had horizontal and vertical signal planes and chamber 2 was rotated 45° counter clockwise to give u-v planes to resolve spatial ambiguity. The superconducting analyzing magnet had an aperture of 20.3 cm by 61 cm and was 2.5 meters long including the cryogenics and magnetic shield. It had a maximum field of about 17 kilogauss which corresponds to a transverse momentum transfer of 1 GeV/c. For the production data the magnet was operated at a field of about 12 kilogauss or a transverse momentum transfer of 0.73 GeV/c to increase the spectrometer acceptance for K_S^0's. The $\int Bdl$ was measured using a rotatable current loop which extended through the magnet and the field intergral was found to be uniform over the region populated by detected particles to ±0.5%. The final value of the field integral was determined by making the reconstructed K_S^0 mass agree with its known value.[40]

A beam veto scintillation counter 10 cm in diameter was located 1.75 meters downstream from the exit of the sweeping magnet and was used in the trigger logic to veto charged particles from sources such as neutron interactions and decays in the collimator. The decay volume between the beam veto counter and chamber 1 was enclosed by a 36 cm diameter vacuum pipe and the vacant spaces between the chambers were filled with helium bags. A 11 m long, 1.5 m in diameter helium filled gas threshold cherenkov counter was located

between chambers 5 and 6 and could be used to distinguish between $p(\bar{p})$ from $\Lambda^0(\bar{\Lambda}^0)$ decay and $\pi^\pm$ from K^0_S decays in the kinematic region where the reconstructed invariant masses are ambiguous. Since the number of ambiguous events was small, the cherenkov counter was not used in the final particle identification for the yield measurements.

An array of 72 Pb-glass blocks was placed downstream of chamber 6 and was stacked in 5 staggered rows of 14 or 15 blocks each with the first block right of center in the middle row removed to prevent most protons from Λ^0 decay from creating hadron showers in the array. This array of Pb glass blocks shadowed the magnet aperture and was used to detect γ rays from Ξ^0 decays. Each block was 10 cm x 10 cm x 38 cm and had a RCA 6655A photomultiplier tube epoxied to its back. The signal from each photomultiplier was integrated by an 8 bit analogue to digital converter (ADC) which was read for each event. The information from this array however was not used in the analysis presented here.

D. The Chambers and Readout Electronics

Each MWPC chamber had two signal planes, with 2.5 micron gold plated tungsten wires, sandwiched between three high voltage(HV) planes, which were made with 6.4 micron beryllium-copper (25 alloy) wires. (See Figure 5.) The wire separation was 2 mm for the signal planes and 1 mm for the HV planes and the distance between the planes was 0.48 cm.

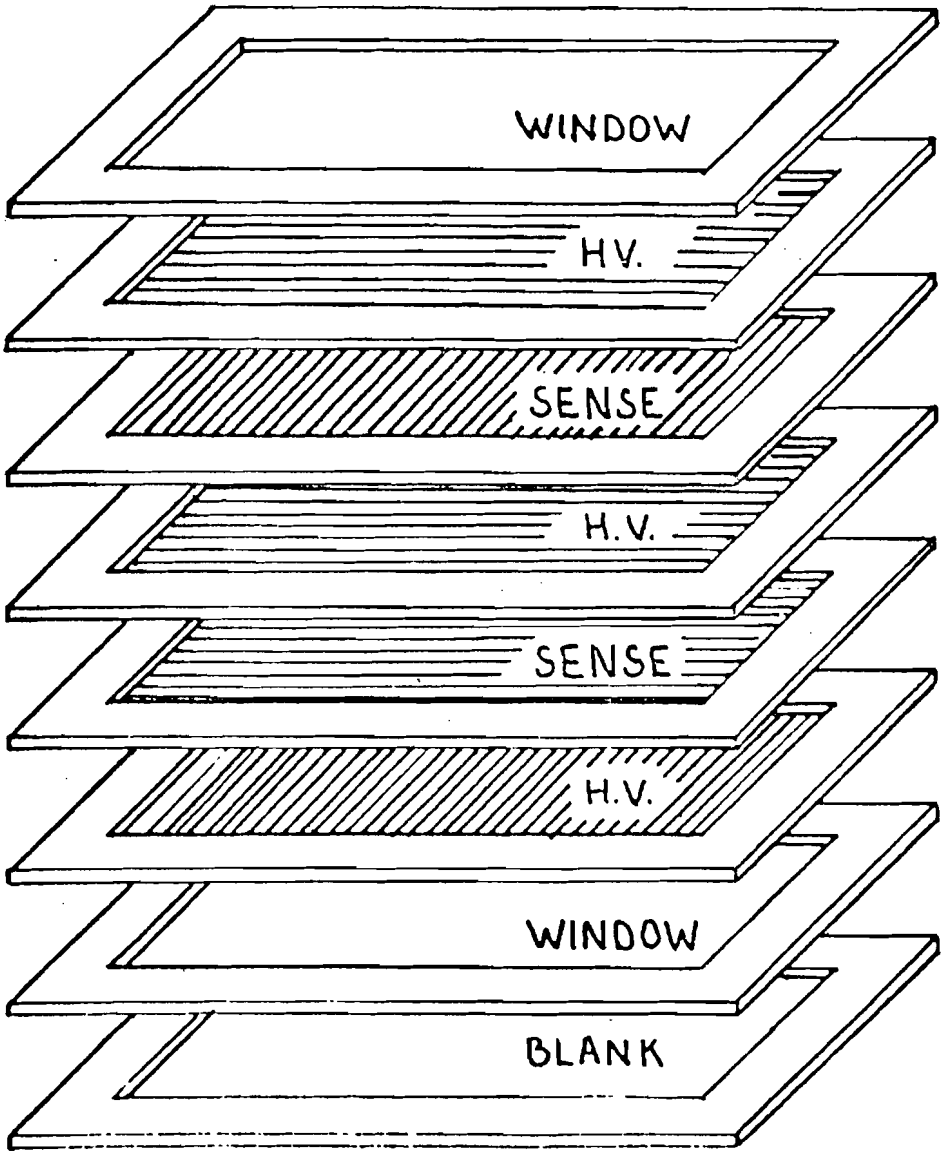

Fig. 5. Chamber assembly.

The wires were wound at constant tension around a rotating aluminum paddle with the wire separation controlled by a high precision screw. Then the wires were soldered to printed circuit boards which had been epoxied to a 0.48 cm thick fiberglass epoxy-board frame. The chambers were filled with a standard gas mixture of about 70% argon, 30% isobutane, and 0.3% freon which was bubbled through liquid methylal at 40° F. The chambers were mounted in enclosed aluminum boxes with aluminum foil windows. Also mounted in the chamber box were signal amplifier printed circuit boards, each of which serviced four wires. The chamber boxes were air conditioned to remove heat created by the amplifier electronics and to reduce external corona by lowering the humidity. The chamber operating voltage was typically 4200 volts.

On the passage of a charged particle through a chamber, the signal generated on the nearest wire was amplified, triggered an electronic delay circuit, and generated a fast trigger pulse which was OR'ed with other wires in the same plane. The OR signals from the chambers were used to form a master trigger coincidence which in turn generated an enable pulse which was sent in parallel back to the chambers. Upon coincidence between the output pulse from the delay circuit and the enable pulse, a latch on the amplifier board corresponding to the hit wire was set. Each wire in the spectrometer had a unique 16-bit address. The addresses of hit wires were read sequentially into memory by the on-line

PDP 11-45 computer through a CAMAC interface system. Altogether, thirty six 16-bit words of ADC information, one 16-bit latch word, and up to 63 MWPC wire addresses were read for each event. The data taking rate was limited by the amount of computer memory and the maximum event rate was 220 events/pulse.

E. The Trigger Logic

Figure 6 is a schematic of the trigger logic. The fast OR signals from the amplifier boards of each plane of wires were OR'ed at the chamber box. The left and right halves of the planes of vertical wires were OR'ed separately for chambers 3,4,5, and 6. An AND was then formed at the chamber box between the OR's from the horizontal and vertical planes for all chambers except chamber 1. Therefore the following signals were available for pattern recognition:

1x,

2x•2y,

3Lx•3y, or 3Rx•3y,

4Lx•4y, or 4Rx•4y,

5Lx•5y, or 5Rx•5y,

6Lx•6y, or 6Rx•6y.

For the production data the trigger was made as loose as possible to avoid biasing the trigger against any detectable decay. The trigger used consisted of a

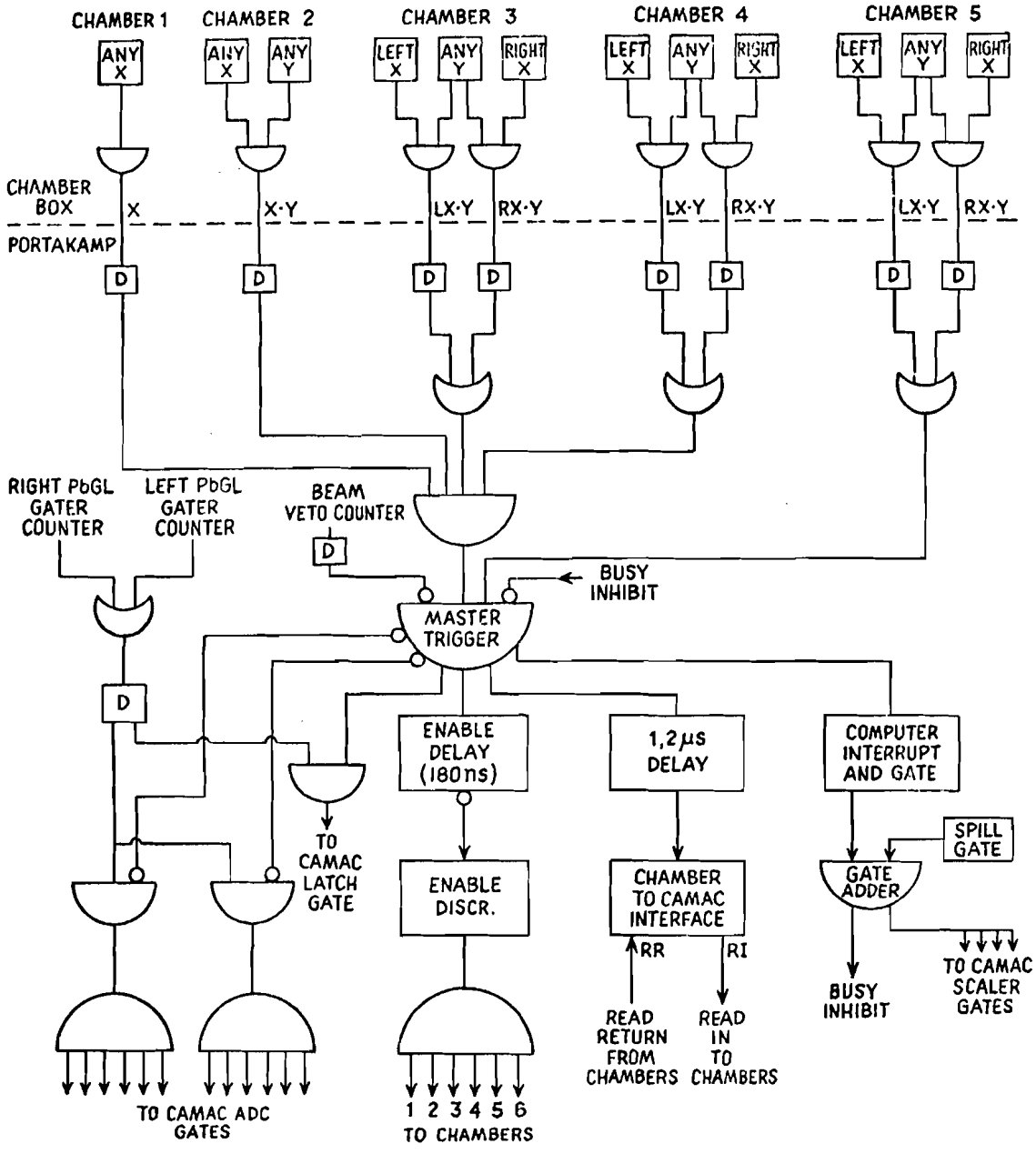

THE TRIGGER LOGIC

Fig. 6. The trigger logic.

coincidence between chambers 1, 2, 3, 4, and 5 requiring one track. Chamber 6 was not required since events could be reconstructed without any hits in chamber 6. The trigger was

$\bar{V} \cdot 1x \cdot (2x \cdot 2y) \cdot (3Lx \cdot 3y + 3Rx \cdot 3y) \cdot (4Lx \cdot 4y + 4Rx \cdot 4y) \cdot (5Lx \cdot 5y + 5Rx \cdot 5y)$

where V is the 10 cm beam veto scintillation counter.

F. Data Taking

It took approximately 45 minutes to fill one tape which contained 80,000 triggers. At 0.6 mr 50% of the triggers were later reconstructed as neutral vee's with 44% Λ^0, 0.5% $\bar{\Lambda}^0$, and 5.5% K^0_S. The remaining triggers were ~~mostly~~ Largely single tracks, neutron interactions and gamma conversions. The incident proton beam intensity was varied to saturate the readout electronics at the maximum event rate of 220 triggers/pulse and ranged from about 2×10^6 protons/pulse at 0.6 mr to about 10^7 protons/pulse at 9 mr. Typically four tapes were taken at each production angle for the 1/2 interaction length Be target while only one tape was taken at each angle for the 1/2 interaction length Cu and Pb targets. Table 1 summarizes the total yield of neutral strange particles for each production angle and each target. The neutral monitors were scaled and were read once between each spill. The scalers were summed for 8 spills by the computer and then the sums were written on tape. Since the ion chamber could not be gated during the spill, the neutral monitors were scaled both gated and ungated. The ratio of a

Production Angle (mrad)	Number of Events								
	Λ°			$\bar{\Lambda}^\circ$			K_s°		
	Be	Cu	Pb	Be	Cu	Pb	Be	Cu	Pb
.6	122000	25500	28300	882	216	273	7230	1620	1890
.7	27000	50700	25900	190	438	288	1620	3290	1730
1.3	87700	31400	30500	651	289	312	5550	2140	2140
1.5	114000	53700	28900	900	555	319	7480	3790	2050
1.9	84200	30900	30000	748	354	371	5770	2260	2340
3.3	78600	—	26100	1100	—	447	6940	—	2690
3.8	16800	—	—	310	—	—	1620	—	—
5.3	86300	—	19300	2230	—	577	10700	—	2440
7.2	46000	—	15700	1920	—	698	7010	—	2360
8.9	35500	8620	12400	1980	508	736	5750	1360	2050
Total	698100	200820	217100	10911	2360	4021	59670	14460	19690

Table 1. Yield of produced particles.

gated monitor to the same monitor ungated was used to correct the total ion chamber reading for experiment deadtime.

A beam focus and ion chamber calibration check was made before each run at an intensity of from 10^6 to $3x10^6$ protons/pulse. The ratio P/(P+H) where P is the 0.635 cm proton counter and H is the halo counter, was calculated as a monitor of the beam focus and typically varied between 0.85 and 0.90. This ratio remained stable during each 3 or 4 day running period after the beam was tuned. The rate dependence of the proton counters was studied during the course of the experiment and a rate correction was made for rates above 10^6 counts/pulse. The ratio (P+H)/IC where IC is the ion chamber reading in volts, was also calculated before each run and was used to calibrate the ion chamber. There was no evidence of a systematic variation in this ratio during the running period however changes in beam tuning in conjunction with a slight misalignment between the proton and halo counters caused a scatter in the value of the ratio at each reading. The average of 48 readings resulted in a value of (P+H)/IC = 14.3±0.7.

For non-zero production angles, the required current in the upstream bending magnets was calculated from the desired nominal production angle with the use of a field map of the external beam line bending magnets.[41] The actual angle which resulted was checked against the calculated one with the two

proportional chambers which were located upstream of the sweeping magnet. These angles agreed within the resolution of the chambers.

During the course of the running period several runs were taken with a low intensity proton beam and with the upstream bending magnets and the sweeper and analyzing magnets off. These runs were used to define a coordinate system in which the relative chamber alignment was defined and which was used by the reconstruction program to calculate particle positions. The coordinate system was thus defined by the direction of the proton beam. One run was taken at +1 mr with the sweeper and analyzing magnets off to check the calculated production angle and was found to agree with it to ±0.1 mr.

Data were taken in five runs, each consisting of four to six weeks, during the period from September 1974 to March 1976. The data to be presented here were obtained during a six week run which occurred in June and July of 1975.

CHAPTER III

DATA ANALYSIS

A. The Reconstruction Program

The raw data tapes were processed by a reconstruction program which searched for neutral vee's from the decay modes $\Lambda^0 \to p\pi^-$, $\bar{\Lambda}^0 \to \bar{p}\pi^+$, and $K_S^0 \to \pi^+\pi^-$. The momentum components of each track, the vertex position of the reconstructed vee, and the error matrix obtained in the track fitting were written to a compacted tape for those events with the neutral vee topology. In this way most single tracks, neutron interactions, and gamma conversions were eliminated from the data sample.

The compacted tape was processed by a particle identification program which performed a fit to the invariant mass assuming that the vee was due to the decay of a Λ^0, $\bar{\Lambda}^0$, or K_S^0. Since the momentum resolution was momentum dependent, the mass window for accepted events also depended on momentum. Events which were ambiguous between Λ^0 and K_S^0 were assumed to be Λ^0 while events ambiguous between $\bar{\Lambda}^0$ and K_S^0 were rejected. From unambiguous Λ^0 and K_S^0 yields and from a Monte Carlo calculation of the ratio of ambiguous to unambiguous K_S^0's, it was estimated that the number of K_S^0's which were assumed to be Λ^0's resulted in less than 1/2% contamination of the Λ^0 sample for all

momenta. K^0_S's for which the higher momentum decay product was a positive track were rejected to avoid Λ^0 contamination of the K^0_S sample. This resulted in a cut of about 50% of the K^0_S's. The FWHM of the reconstructed mass was 6 MeV for the Λ^0 and $\bar{\Lambda}^0$ and 14 Mev for the K^0_S. Figure 7 shows the Λ^0 and K^0_S reconstructed mass distributions from a typical 0.6 mr run.

Geometric cuts were made along the edges of all chambers and in the z vertex position at both ends of the decay volume to eliminate regions of the acceptance where the detection efficiency or reconstruction efficiency were poor. From the decay vertex position and the momentum components of the reconstructed neutral vee, the radial position (R) of the neutral particle at the production target could be calculated. Events with $R^2>40$ $(mm)^2$ were rejected to reduce background from neutral strange particles not directly produced in the target. Altogether these geometric cuts eliminated about 25% of the data.

Accepted events were binned in 5 GeV/c momentum bins and the following quantities along with their measured errors were calculated for each event and accumulated for each bin:

1) N = number of particles,

2) p_{lab} = laboratory momentum,

3) p_T^2 and p_T = transverse momentum in the proton-nucleon center of mass frame,

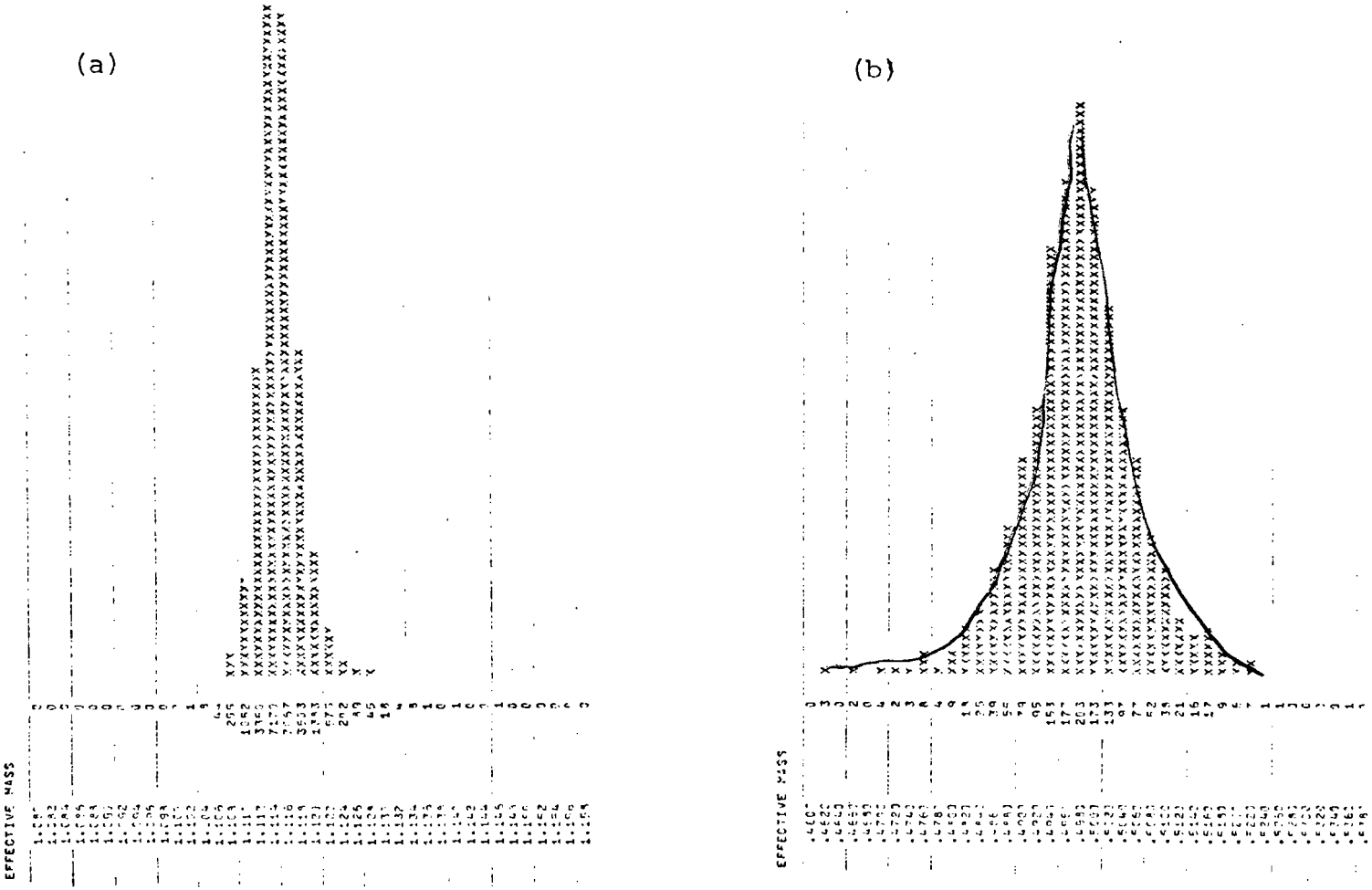

Fig. 7. Reconstructed mass distributions for (a) Λ^0 and (b) K^0_S.

4) x = the Feynman scaling variable = P_L^*/P_{max}^* where P_L^* is the center of mass (CM) longitudinal momentum of the produced particle and P_{Max}^* is the CM momentum of the incident particle,

5) θ = laboratory angle of the reconstructed particle relative to the incident proton beam direction.

An output file was created containing these binned quantities for every run so that their weighted averages could later be calculated. Runs at the same production angle were combined by summing the accumulated quantities for each bin. Appendix A gives the formula and geometry used to calculate the production angle θ.

B. The Invariant Cross Section

The Lorentz invariant differential inclusive cross section was calculated for the three nuclear targets for Λ^0, $\bar{\Lambda}^0$, and K_S^0 from the following formula:

$$Ed^3\sigma/d\vec{p}^3=(E_{lab}/p_{lab}^2)(d^3\sigma/dp_{lab}d\Omega)=$$
$$(E_{lab}/p_{lab}^2)[(N(p,\theta)AC(p,\theta))/(N_o\rho LIA(p)B\Delta p\Delta\Omega)]$$

where $N(p,\theta)$ is the number of events in a bin, E_{lab} and p_{lab} are the average laboratory energy and momentum of the reconstructed particle, A, ρ, L are the atomic weight, density, and length of the target respectively, B is the branching ratio for the observed decay mode, N_o is Avogadro's number, I is the number of protons incident on

the target, Δp is the momentum bin size (5 GeV/c), $\Delta\Omega$ is the solid angle acceptance (1.20×10^{-6} steradians), A(p) is the lifetime and geometric acceptance of the spectrometer, and $C(p,\theta)$ is a correction factor which depends on production angle and momentum. The spectrometer acceptance and reconstruction efficiency were determined from a Monte Carlo program and the correction factor $C(\theta,p)$ is the cumulative result of a number of effects which are described in detail in Section E. The values used for the $\Lambda^0 \rightarrow p\pi^-$ ($\bar{\Lambda}^0 \rightarrow \bar{p}\pi^+$) and $K_S^0 \rightarrow \pi^+\pi^-$ branching ratios were 0.642 and 0.6877 respectively.[40]

No attempt was made to distinguish directly produced particles from those resulting from electromagnetic or strange decays such as $\Sigma^0 \rightarrow \gamma\Lambda^0$ or $N^* \rightarrow \Lambda^0 K^0$.

C. Normalization

The number of protons incident on the production target was calculated from the following formula:

$$I = IC_{total}(n_g/n_{ug})[P/(P+H)][(P+H)/IC]$$

where IC_{total} is the ion chamber sum for the run, n_g is the gated neutron monitor sum, n_{ug} is the ungated neutron monitor sum, P is the 1/4" proton counter and H is the halo counter. (P+H)/IC is the previously mentioned ion chamber calibration factor and was equal to 14.3 ± 0.7 for all runs,

and P/(P+H) is the fraction of beam hitting the target and varied from 0.85 to 0.90 depending on the run. From the scatter in the Λ^0 yields the relative run to run normalization error was estimated to be 4% FWHM. The total error in the absolute normalization was estimated to be 20% FWHM.

D. The Monte Carlo Acceptance

The Monte Carlo program generated events at the target which passed through the defining collimator and decayed in the decay volume. For the incident beam a Gaussian distribution over the area of the target was assumed and gave a target pointing R^2 distribution which was the same as that of the data. The positions of the decay products at the chambers were calculated and wire hits were generated in the same manner as actual events. The output tape from the Monte Carlo program was then processed by the reconstruction program. The Monte Carlo simulated chamber inefficiencies and adjacent multiple hits where two wires are hit by one particle. Care was taken to make the output momentum spectrum from processed Monte Carlo events the same as the momentum spectrum of the data so that the Monte Carlo acceptance would correct for the smearing effect caused by the finite momentum resolution of the spectrometer. Altogether the Monte Carlo acceptance corrected for the geometric acceptance (including lifetime) of the spectrometer, the reconstruction program efficiency

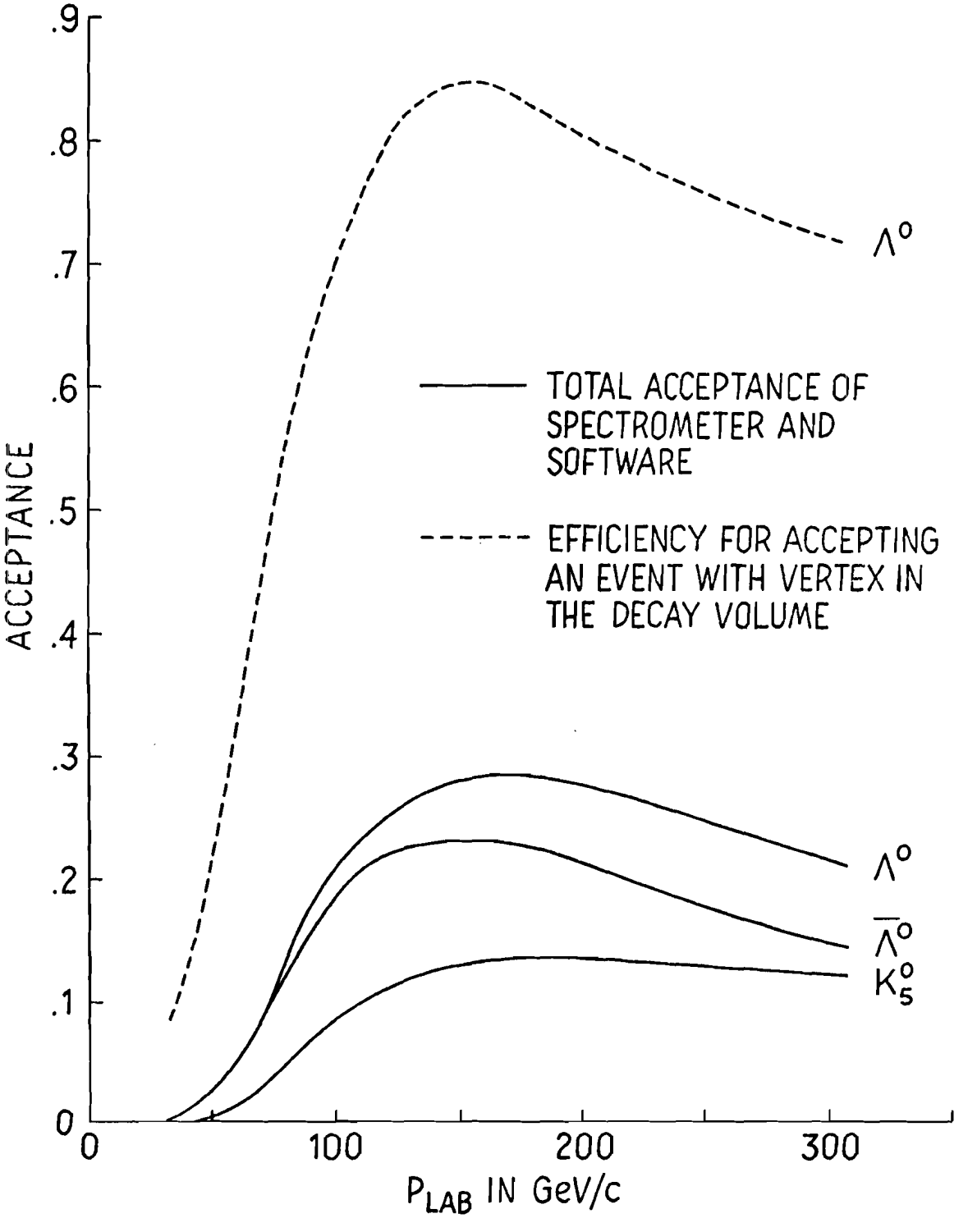

Fig. 8. Spectrometer acceptances for Λ^0, $\bar{\Lambda}^0$, and K_S^0 including lifetimes, spectrometer geometry, and reconstruction efficiency as a function of laboratory momentum.

including ambiguity cuts, and the resolution of the detector. The Monte Carlo acceptances for Λ^0, $\bar{\Lambda}^0$, and K_S^0 are shown in Figure 8 as a function of laboratory momentum. The value used for the Λ^0 and $\bar{\Lambda}^0$ lifetime was 2.61×10^{-10} seconds[42] and the value used for the K_S^0 lifetime was 0.886×10^{-10} seconds.[40]

E. Corrections

A target pointing cut was made at a radius squared, R^2, of 40 $(mm)^2$ to eliminate background which was due primarily to scattering of the neutral beam in the defining collimator. This background was most prevalent at low momentum for the low production angle data as would be expected for a scattering process whose source is between the target and the decay volume. Therefore a momentum dependent correction was made for background contained within the R^2 cut.

This correction was made by fitting the sum of two Gaussian functions of R, one representing events produced at the target and the other representing events produced by collimator scattering, to data with R^2 between 0 and 200 $(mm)^2$ in 20 GeV/c momentum bins. The function which described the background was then integrated inside the R^2 cut with the aid of a Monte Carlo simulation of collimator scattering. Figure 9 shows the R^2 distribution of data compared with the R^2 distribution of Monte Carlo events

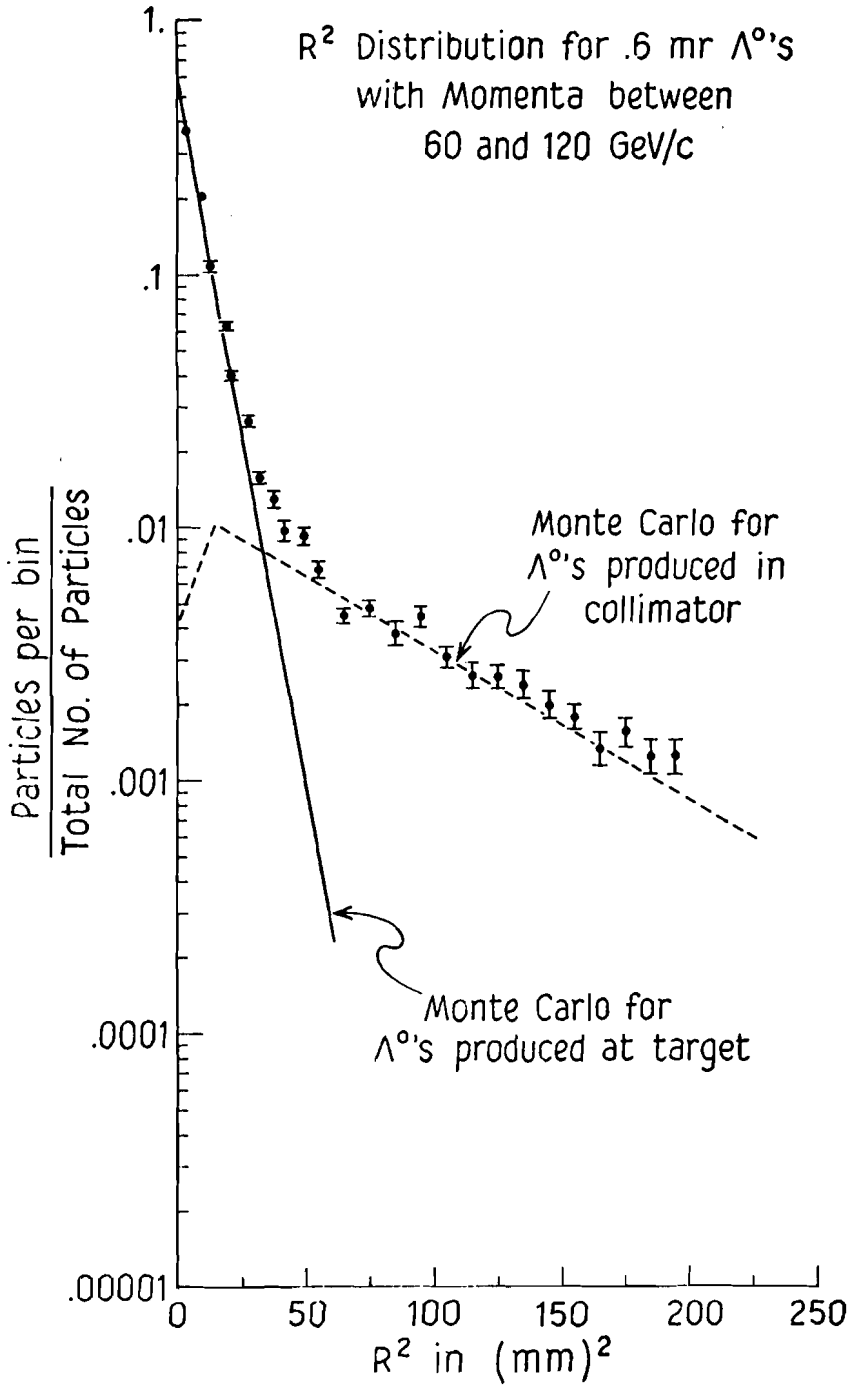

Fig. 9. R^2 distribution for .6 mr Λ^0's with momenta between 60 and 120 GeV/c compared with R^2 distributions of Monte Carlo Λ^0's produced at the target and in the collimator.

produced at the target and Monte Carlo events simulating collimator scattering. There is a geometric cutoff in the Monte Carlo collimator scattering distribution inside the aperture of the defining collimator. For Λ^0 this correction varied from -10% at 60 GeV/c and 0.6 mr to -5% for momenta greater than 150 GeV/c or angles greater than 2 mr.

A significant number of events which were reconstructed as vee's and had invariant masses on the tails of the Λ^0, $\bar{\Lambda}^0$, or K_S^0 mass distributions, did not have masses within the mass window defined by the particle identification subroutine. The number of such events was found to be greater in data tapes than in Monte Carlo tapes. A correction was made to account for the excess number of these events and was independent of production angle and particle indentity but depended only on momentum, and varied from +12% at 60 GeV/c to +2% at 200 GeV/c.

A sample of events which the reconstruction program determined were not vee's was scanned by hand and a +1% correction was applied to correct for good vee's lost by the program for reasons not accounted for by the Monte Carlo. This loss was caused mainly by accidental hits in the data.

During the experiment a number of target out runs was taken at selected production angles to measure the yield of neutral strange particles produced by interaction of the proton beam with material other than the target such as air and scintillation counters. The ratio, OUT/IN, of the total

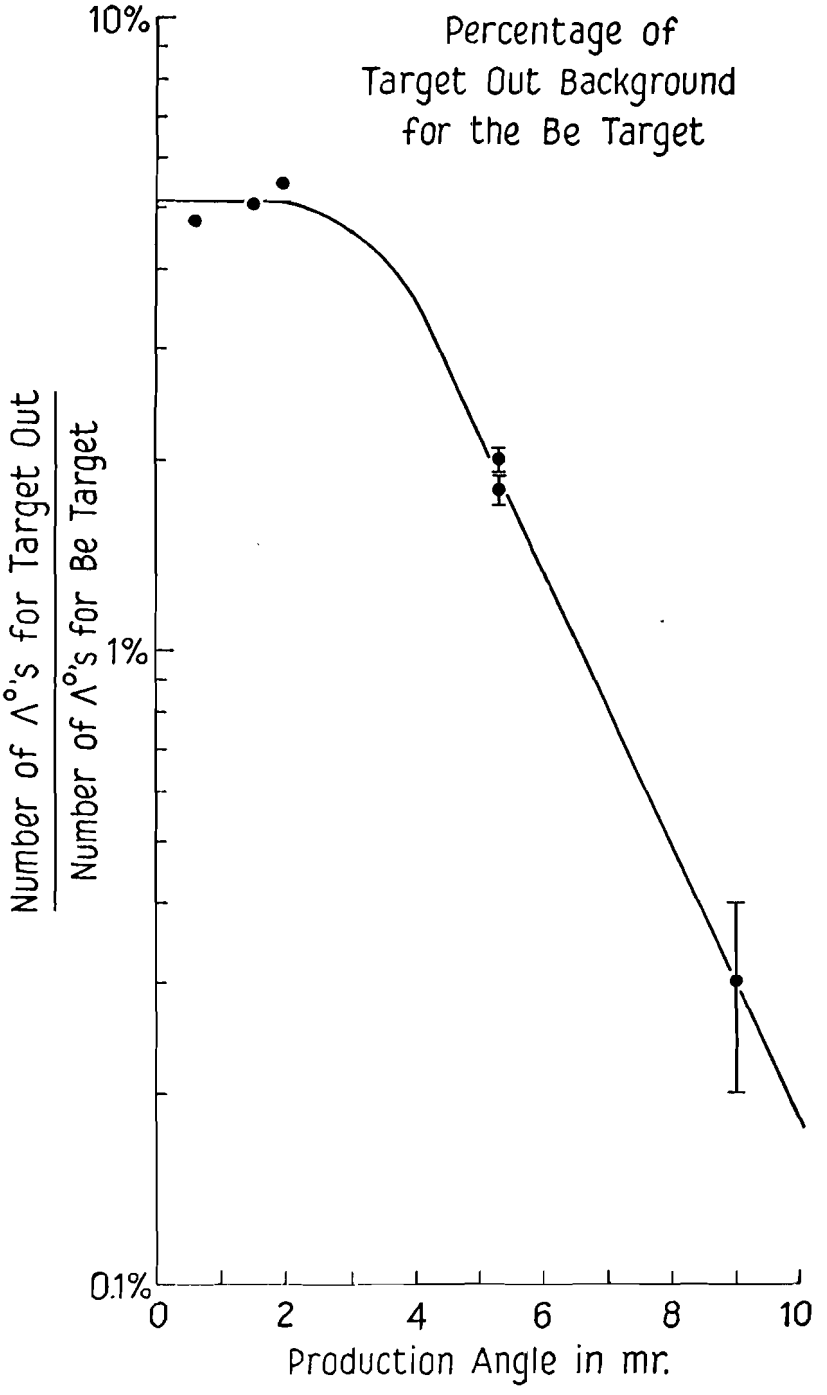

Fig. 10. Percentage of target out background summed over momentum for the 1/2 interaction length Be target as a function of production angle. The error bars indicate the statistical errors.

Λ^0 yield for target out to the total Λ^0 yield for target in is shown in Figure 10 as a function of production angle for the 1/2 interaction length Be target. Figure 11 shows the momentum spectra of the target out data scaled by the OUT/IN ratio together with the 1/2 interaction length Be target data for 0.6 and 5.3 mr.

A momentum independent target empty subtraction was made to correct for this background based on the OUT/IN ratios. For the 1/2 interaction length Be target this correction varied from -5% for production angles 2 mr or less to less than -1% at 9 mr. From Figure 11(b), the 5.3 mr momentum distribution, one sees that a large amount of background is present at high momentum. This high momentum background was isolated in the production angle distribution of the 5.3 mr target out data and was found to be consistent with production from a concentration of material which was located approximately 16.5 meters upstream of the target. This material consisted of a lucite test target in addition to two ion chambers, all of which were used by other experiments. Figure 12 shows the production angle distribution for one 5.3 mr target out run for all Λ^0's and for Λ^0's with momenta above 200 GeV/c. The 5.3 mr target out production angle distribution of Λ^0's with momenta above 200 GeV/c is localized about the average value of 4.7 mr indicating that the position of the source of high momentum Λ^0's is well localized along the proton beam direction. From the angle distribution of the high momentum background

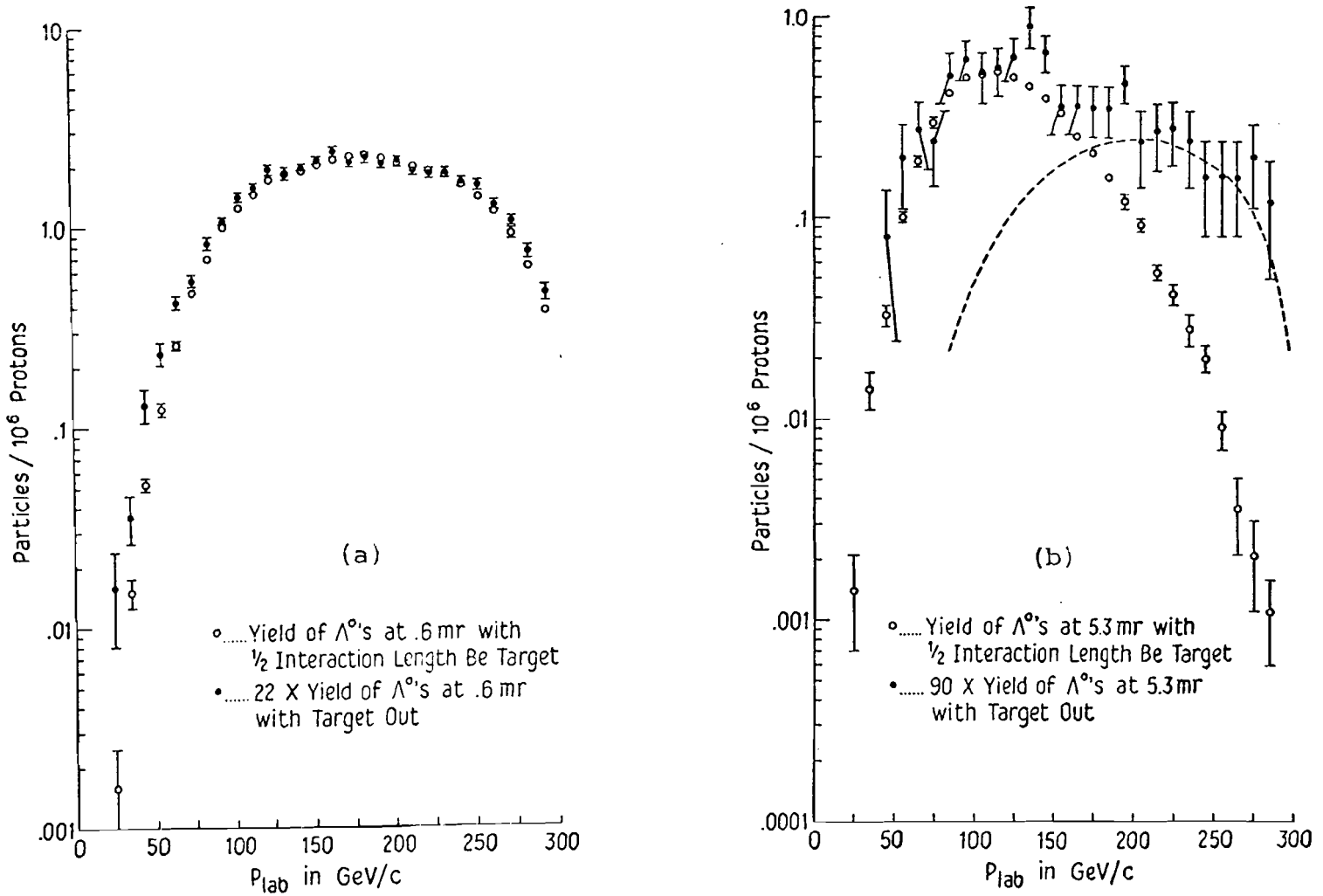

Fig. 11. Comparison of the shapes of the laboratory momentum distributions for Λ° production with the 1/2 interaction length Be target versus target out at (a) .6 mr and (b) 5.3 mr.

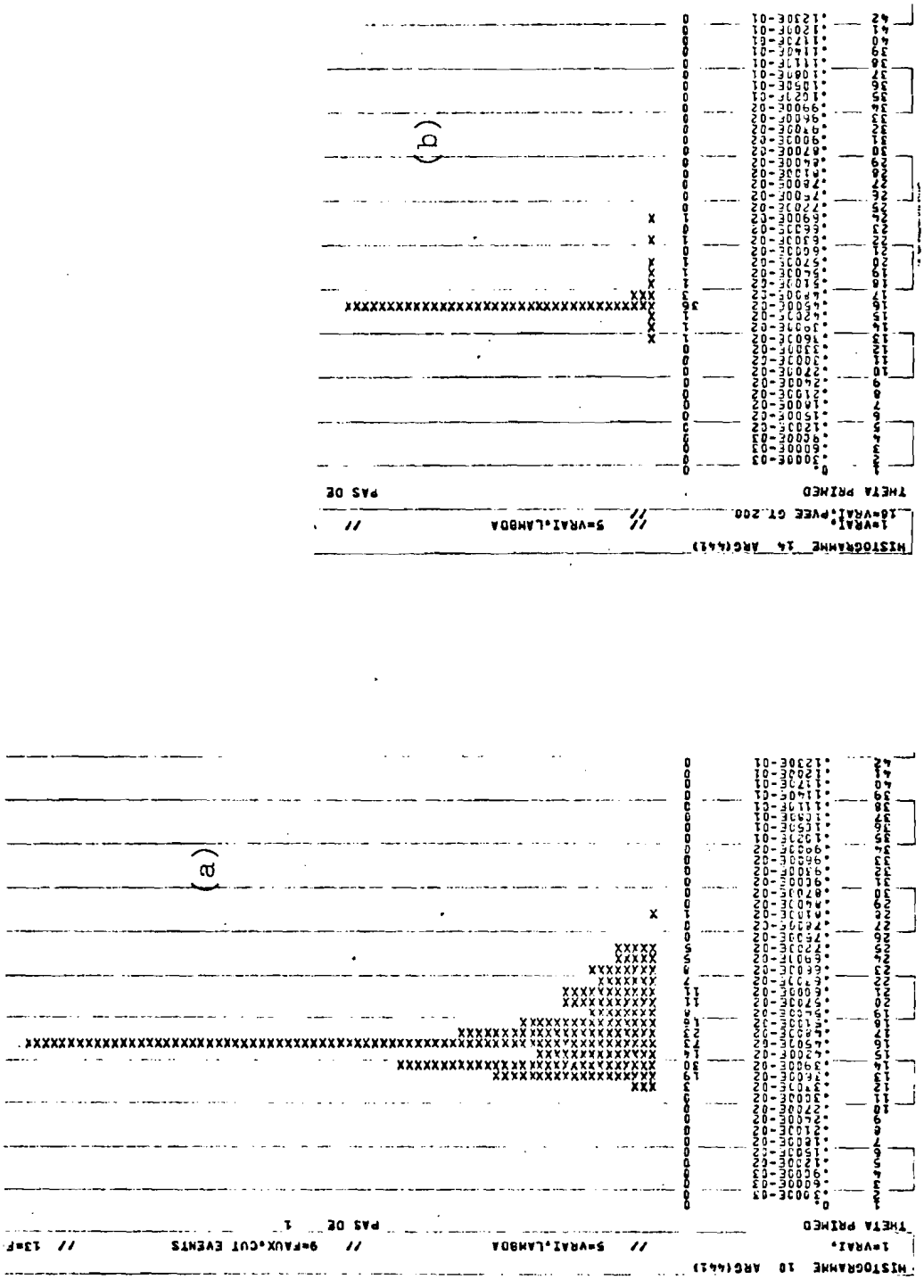

Fig. 12. Laboratory production angle distributions for (a) all Λ^0's and (b) Λ^0's with momenta above 200 GeV/c.

and the incident proton beam direction the position of the source could be determined from the data. The calculated invariant cross sections for Λ^0, K^0_S, and $\bar{\Lambda}^0$ (with all corrections except this one) were fit to the function described in the next section which was then used to calculate the production of neutral strange particles from the upstream source as a function of laboratory production angle and momentum. The normalization for Λ^0 production from the upstream source was obtained from the isolated target out Λ^0 yield at 5.3 mr and the normalization for K^0_S and $\bar{\Lambda}^0$ production from the upstream source was obtained from the K^0_S/Λ^0 and $\bar{\Lambda}^0/\Lambda^0$ ratios (corrected for lifetime and geometric acceptance) which were measured in production from the Be target. This calculated yield was used to make an angle and momentum dependent subtraction to correct for background due to the upstream source. It was assumed that the error in the correction was due to the statistical error in the 5.3 mr target out yield of high momentum Λ^0s. The dashed line in Figure 11(b) indicates the calculated yield of lambdas from the upstream source at 5.3 mr.

The largest momentum independent correction was due to absorption of protons and produced particles by the production target. Several runs were taken with a 1/4 interaction length Be target and the momentum spectrum is compared with that of the 1/2 interaction length Be target in Figure 13. The shape of the spectrum does not depend on the length of the target, and thus the correction due to the

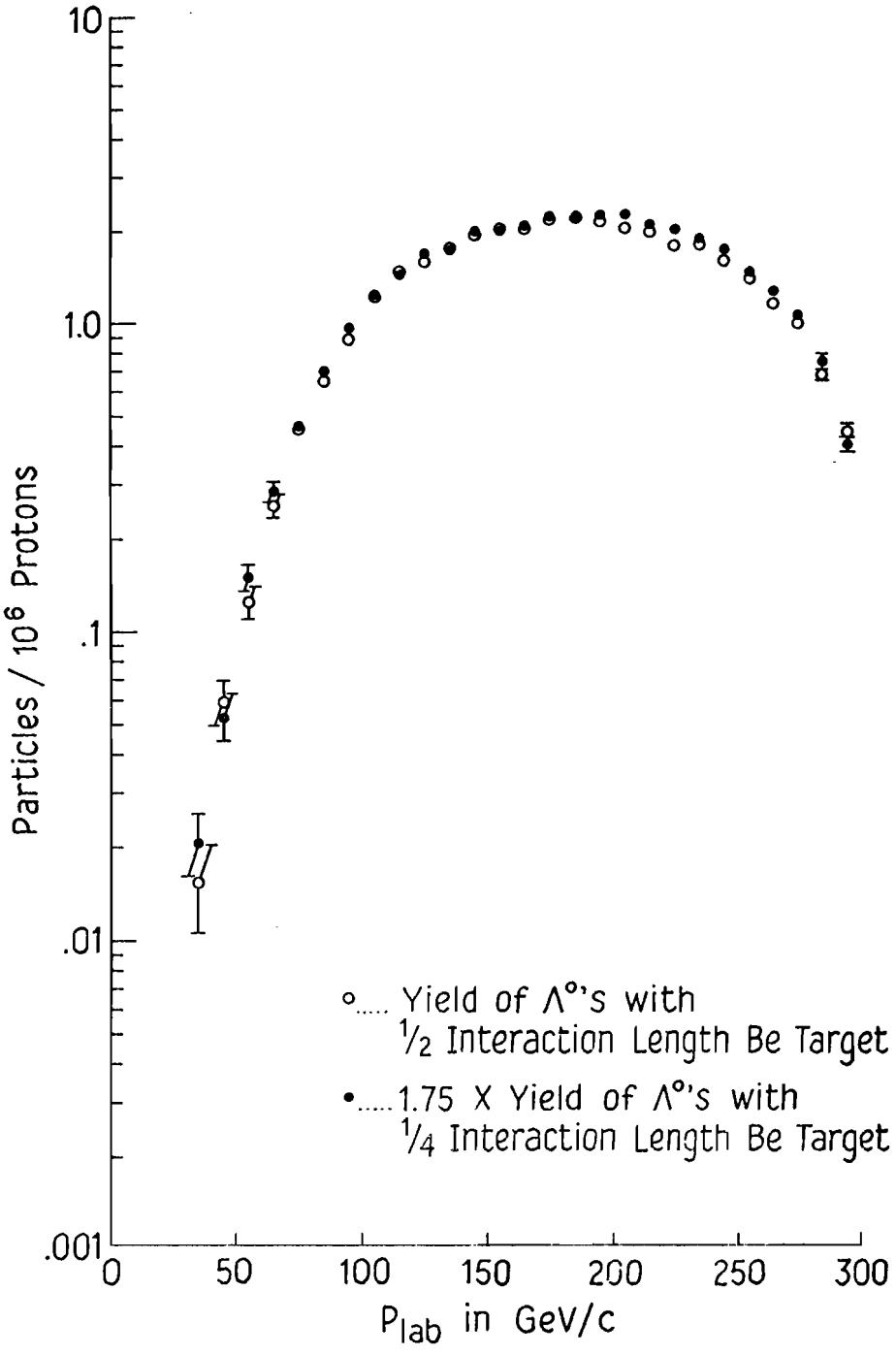

Fig. 13. Comparison of the shapes of the laboratory momentum distributions for Λ^0 production with 1/2 versus 1/4 interaction length Be targets.

finite length target is just one of normalization.

This normalization correction can be parameterized in terms of the absorption length for protons l_o, the target length L, and the measured ratio (R) of the yield of produced particles for the 1/2 interaction length Be target to that for the 1/4 interaction length Be target. As shown in Appendix B the correction factor, c, is given by the following formula for the 1/2 interaction length Be target:

$$c=2\ln(R-1)/[R(R-2)].$$

It is also shown in Appendix B that the correction for the 1/2 interaction length Cu and Pb targets can be calculated from the ratio R for Be as follows:

$$c_i=(2\beta/\alpha)\ln(R-1)[(R-1)^{2\beta/\alpha}-1]^{-1}$$

where β is the ratio of the length of the Cu or Pb target to the length of the Be target and α is the ratio of the proton absorption length of Cu or Pb to that of Be. The values of α were calculated from the absorption lengths tabulated in Reference 43.

The measured values of R were 1.78±0.05 for Λ^0 and 1.77±0.07 for K_S^0. From these values the corrections obtained for both Λ^0 and K_S^0 were 1.26±0.07 for Be, 1.20±0.05 for Cu, and 1.17±0.04 for Pb. The ratio for $\bar{\Lambda}^0$

was consistent with that for Λ^0 so the same correction factors were used.

The fraction of events which were lost due to interactions in material such as scintillator, air, and vacuum windows before reaching the spectrometer was calculated to be 6.5% for Λ^0 and $\bar{\Lambda}^0$ and 4.5% for K_S^0. The fraction of events lost due to absorption of their decay products in the chambers and He in the spectrometer was estimated to be 1.5% for Λ^0 and $\bar{\Lambda}^0$ and 1.2% for K_S^0. This gives a total correction of +8.0% for Λ^0 and $\bar{\Lambda}^0$ and +5.7% for K_S^0.

The chamber inefficiencies were monitored off line by counting the missing hits on each reconstructed track with the Monte Carlo (with zero chamber inefficiency) indicating what fraction of this inefficiency was due to mistakes made by the reconstruction program. From this information it was found that all the chambers in the trigger had stable efficiencies between 97.5% and 99.5%. Since two charged particles could trigger the chambers for each neutral vee, the overall trigger efficiency was estimated to be better than 99%.

F. The Fit

The invariant cross section can be expressed in the proton-nucleon center of mass frame in terms of the Feynman scaling variable x and the transverse momentum squared, p_T^2

as follows:

$$Ed^3\sigma/d\vec{p}^3=(2E^*/\pi\sqrt{s})d^2\sigma/dxdp_T^2$$

where E^* is the center of mass energy of the produced particle and $s=(p_1+p_2)^2$ where p_1 and p_2 are the 4-momenta of the incident and target particles respectively. In order to express the data in terms of useful kinematic variables it was convenient to fit a function of x and p_T^2 to the data. The region of phase space populated by the data is shown in Figure 14 where the broken lines indicate the limits due to statistics. Separate fits were performed for each particle for the Be and Pb targets using the following function:

$$Ed^3\sigma/d\vec{p}^3\equiv f(x,p_T)$$
$$=\exp(c_1+c_2x^2+c_3x+c_4xp_T+c_5p_T^2+c_6p_T^4+c_7p_T^6)\cdot(1-x)^{c_8+c_9p_T^2}.$$

The values of the parameters and the χ^2 per degree of freedom for the final fits are given in Table 2. A representative sample of the data is plotted in Figures 15-17 as a function of laboratory momentum for fixed laboratory production angle where the solid lines show the results of the fits. The fits are intended for use as interpolation aids and any extrapolation should be performed with the understanding that the fits are constrained only in the kinematic region were data exist. The data are tabulated in Appendix C.

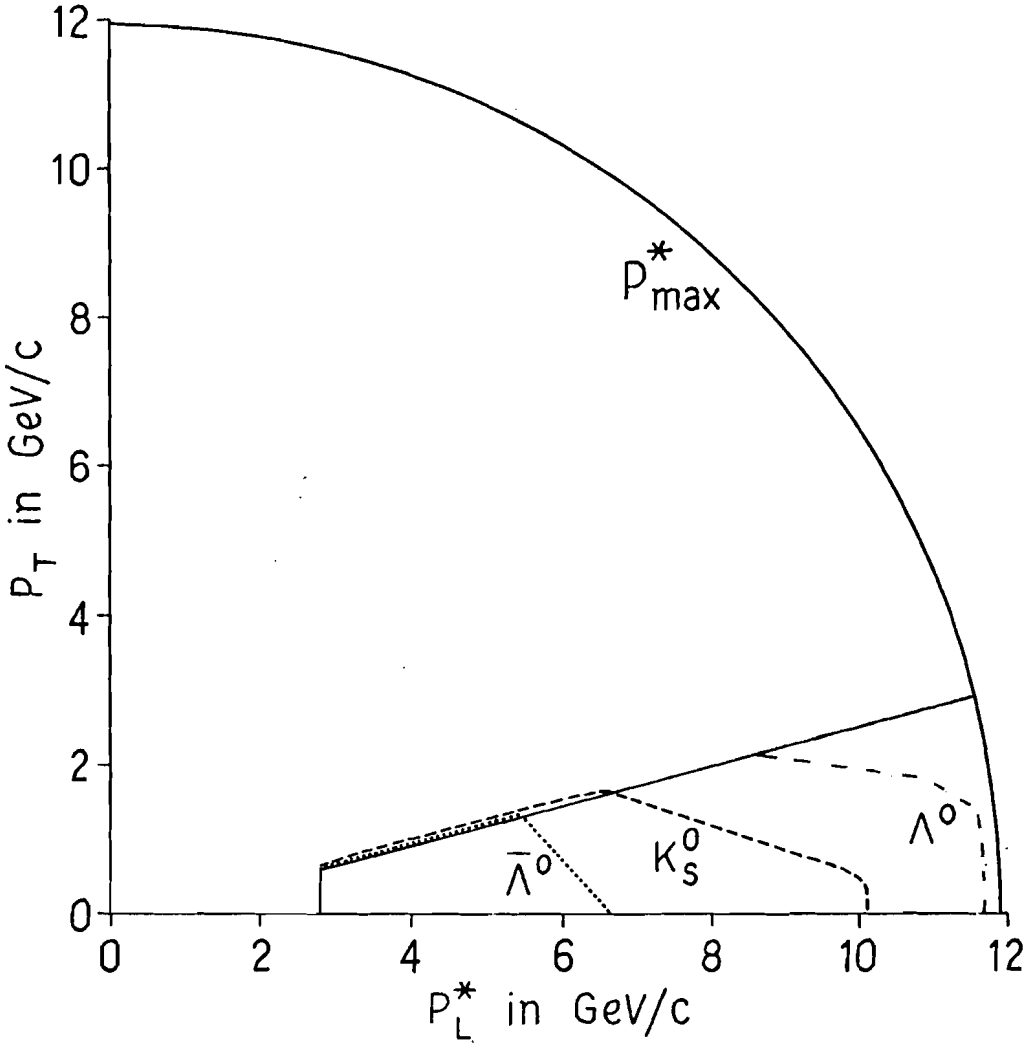

Fig. 14. Kinematic region populated by data.

$$f(x,p_T) = e^{c_1+c_2x^2+c_3x+c_4xp_T+c_5p_T^2+c_6p_T^4+c_7p_T^6}(1-x)^{c_8+c_9p_T^2}$$

	Λ°			$\overline{\Lambda^\circ}$			K_s°		
Parameter	Be	Pb	Nucleon	Be	Pb	Nucleon	Be	Pb	Nucleon
c_1	1.45±.02	4.11±.03	-.38±.04	1.89±.06	4.3±.1	.3 ±.1	2.52±.03	4.74±.08	.6 ±.1
c_2	-.79±.09	1.1±.1	-1.9±.2	———	———	———	———	-2.0±.5	-5.0±.6
c_3	1.28±.07	-1.8±.1	3.3±.1	-12.5±.2	-14.1±.4	-12.2±.5	-3.3±.2	-6.5±.4	-2.3±.5
c_4	-1.09±.05	-.92±.08	-1.2±.1	———	———	———	-2.2±.1	-2.3±.2	-2.3±.3
c_5	-2.21±.04	-1.84±.06	-2.39±.08	-2.31±.05	-1.91±.09	-2.4±.1	-1.89±.05	-1.34±.08	-2.2±.1
c_6	.45±.04	.56±.06	.39±.09	———	———	———	———	———	———
c_7	-.07±.01	-.09±.02	-.05±.03	———	———	———	———	———	———
c_8	.74±.02	.73±.03	.82±.03	———	———	———	2.2±.1	———	———
c_9	.61±.02	.91±.04	.51±.05	———	———	———	———	———	———
Chi-squared / Degree of Freedom	1.63	1.62	1.01	1.07	.95	.92	1.16	1.03	.99

Table 2. Parameters obtained in fits of the data to a function of x and p_T^2.

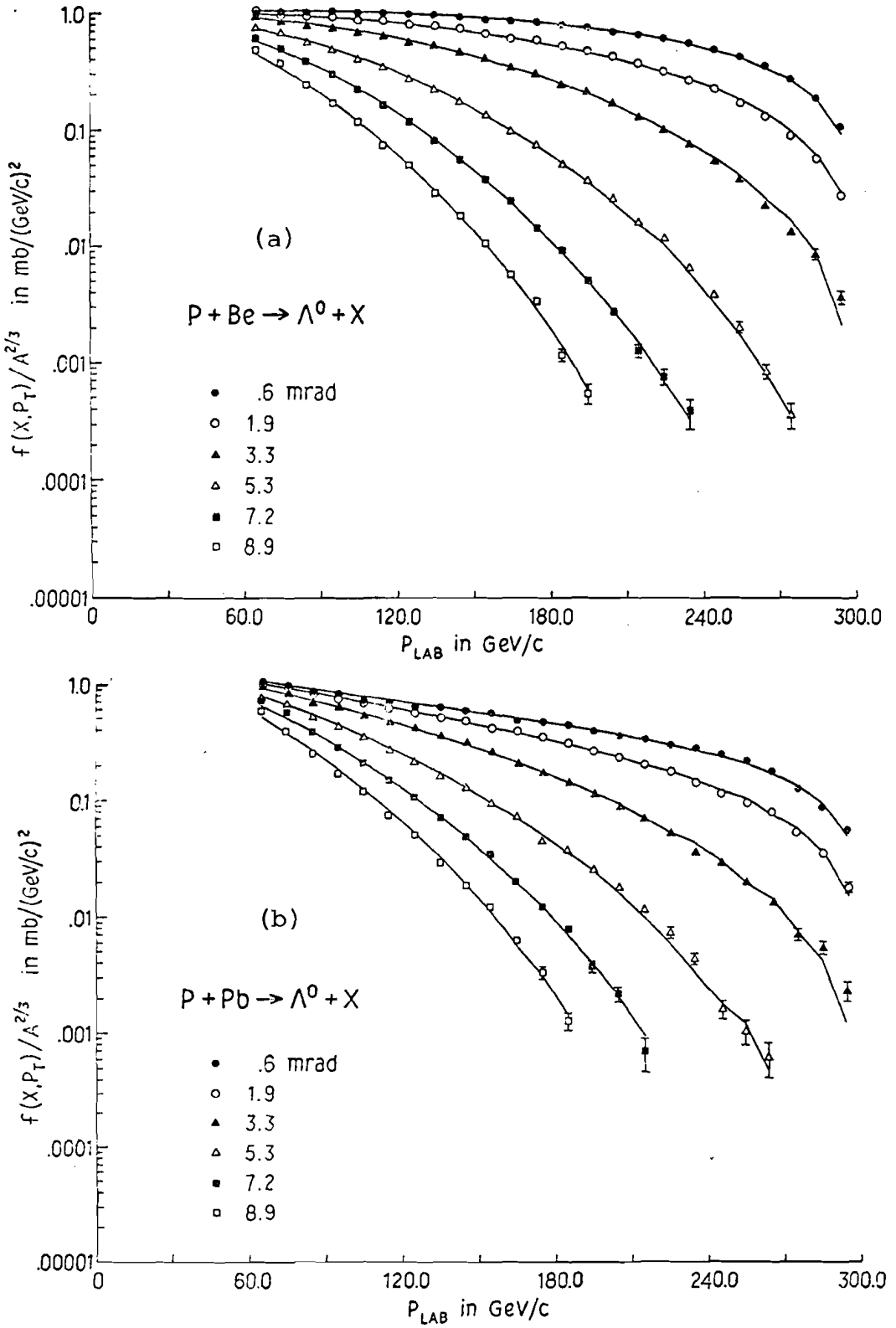

Fig. 15. Invariant cross section versus laboratory momentum for Λ^0 production from (a) Be and (b) Pb. The solid lines are the results of the fit described in the text.

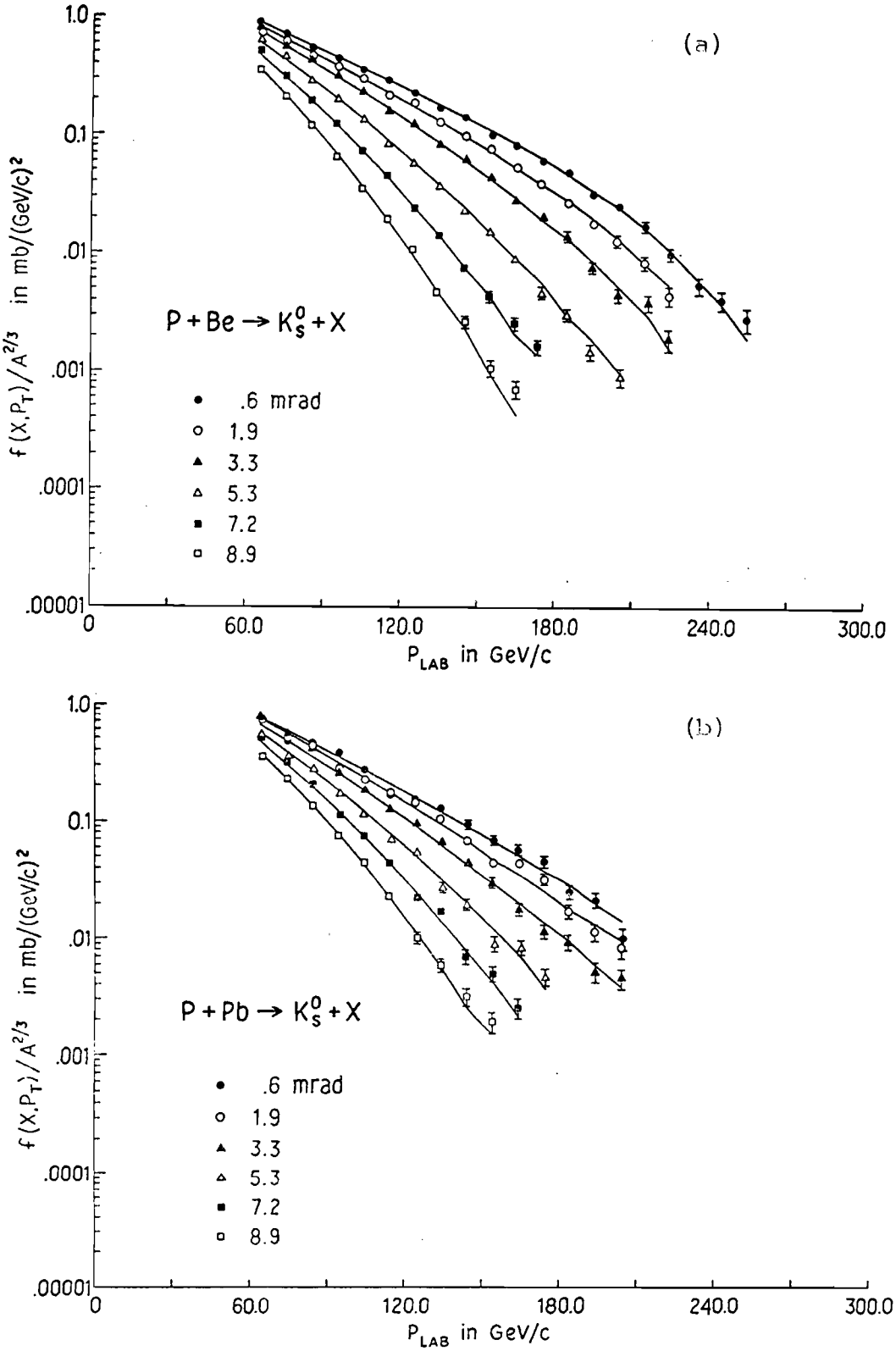

Fig. 16. Invariant cross section versus laboratory momentum for K_S^0 production from (a) Be and (b) Pb. The solid lines are the results of the fit described in the text.

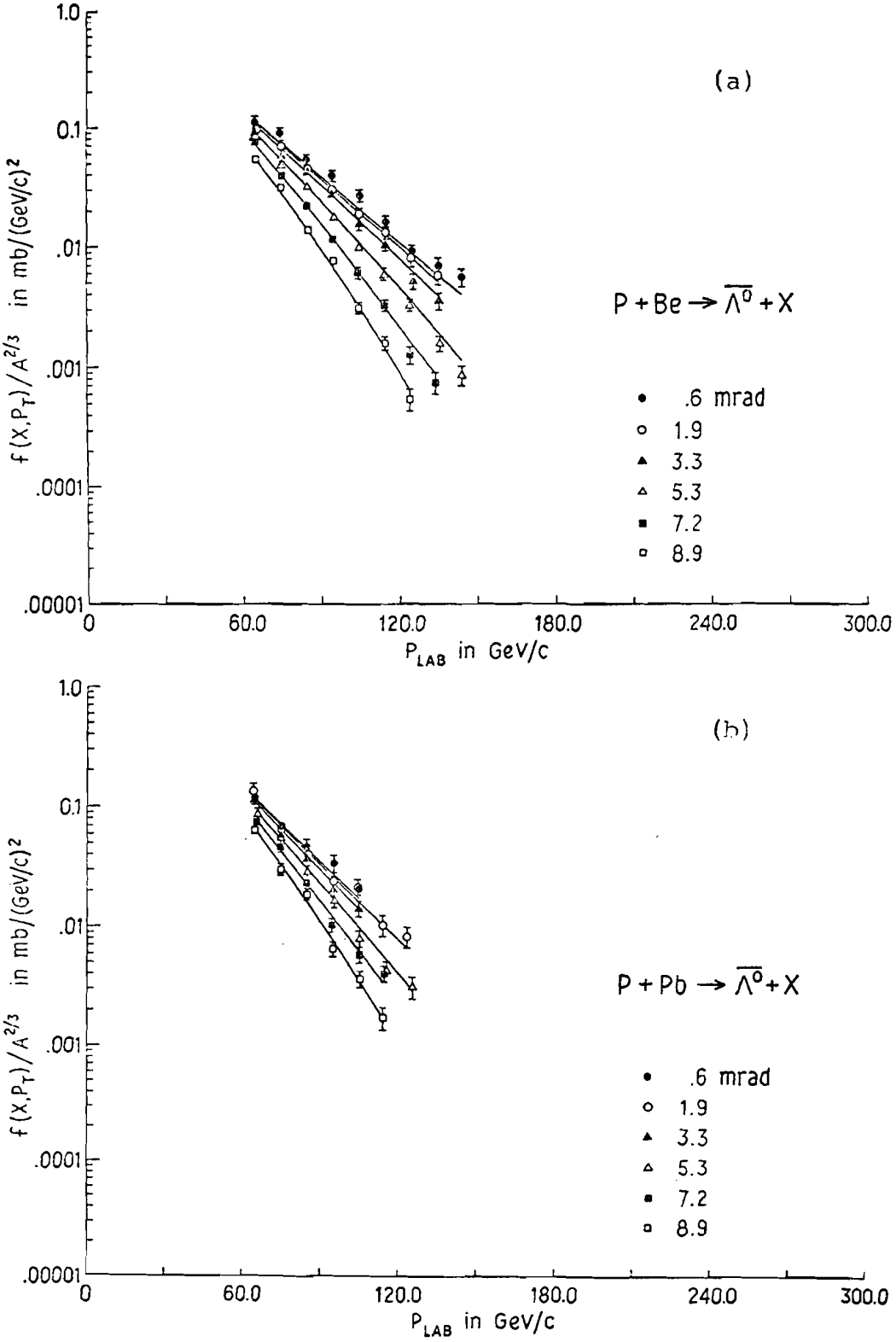

Fig. 17. Invariant cross section versus laboratory momentum for $\bar{\Lambda}^0$ production from (a) Be and (b) Pb. The solid lines are the results of the fit described in the text.

CHAPTER IV

RESULTS

A. Target Dependence Of The Invariant Cross Section

The behavior of the invariant cross section with the target nucleus is consistent with a power law of the form:

$$Ed^3\sigma/d\vec{p}^3=f(x,p_T,A)=f(x,p_T,1)A^{\alpha(x,p_T)} \quad \text{(IV.1)}$$

where A is the atomic mass number and the exponent α is a function of x and p_T. This behavior is illustrated in Figure 18 where the invariant cross section is shown versus A for several values of x and p_T. The error on each point is dominated by the ±2% relative run to run normalization error.

From the fits to the invariant cross section for Be and Pb the exponent α can be calculated as follows:

$$f_{Be}/f_{Pb}=A_{Be}^{\alpha}/A_{Pb}^{\alpha}$$
$$\alpha(x,p_T)=\log(f_{Be}/f_{Pb})/\log(A_{Be}/A_{Pb}).$$

Figure 19 shows α as a function of p_T for fixed x and as a function of x for fixed p_T for Λ^0 and K_S^0 production. α is a strong function of both x and p_T, and at $p_T=0$ for Λ^0 production it varies from 0.45 at $x>0.7$ to 0.7 at $x=0.2$.

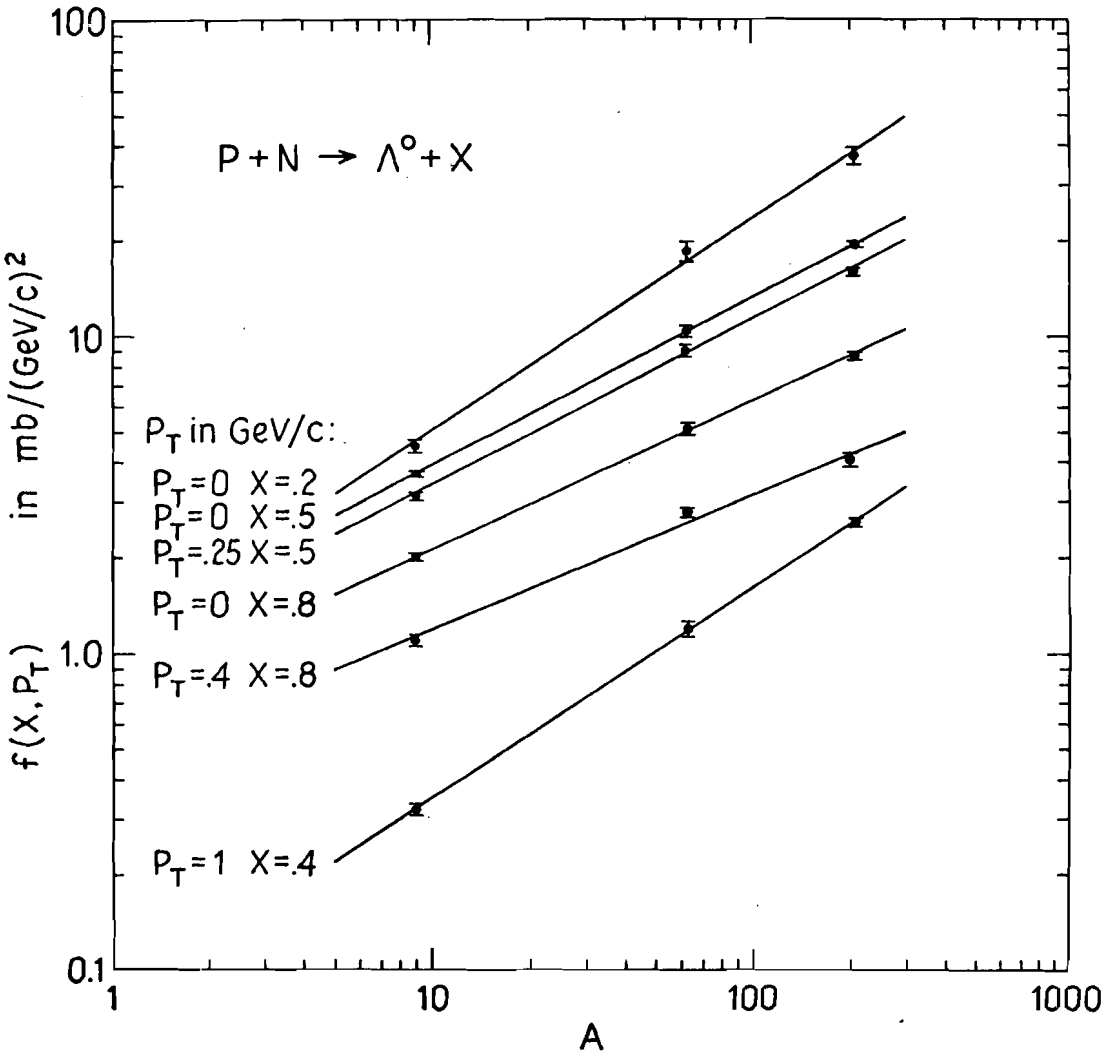

Fig. 18. The behavior of the invariant cross section with A for Λ^0 production. The lines were hand drawn to guide the eye.

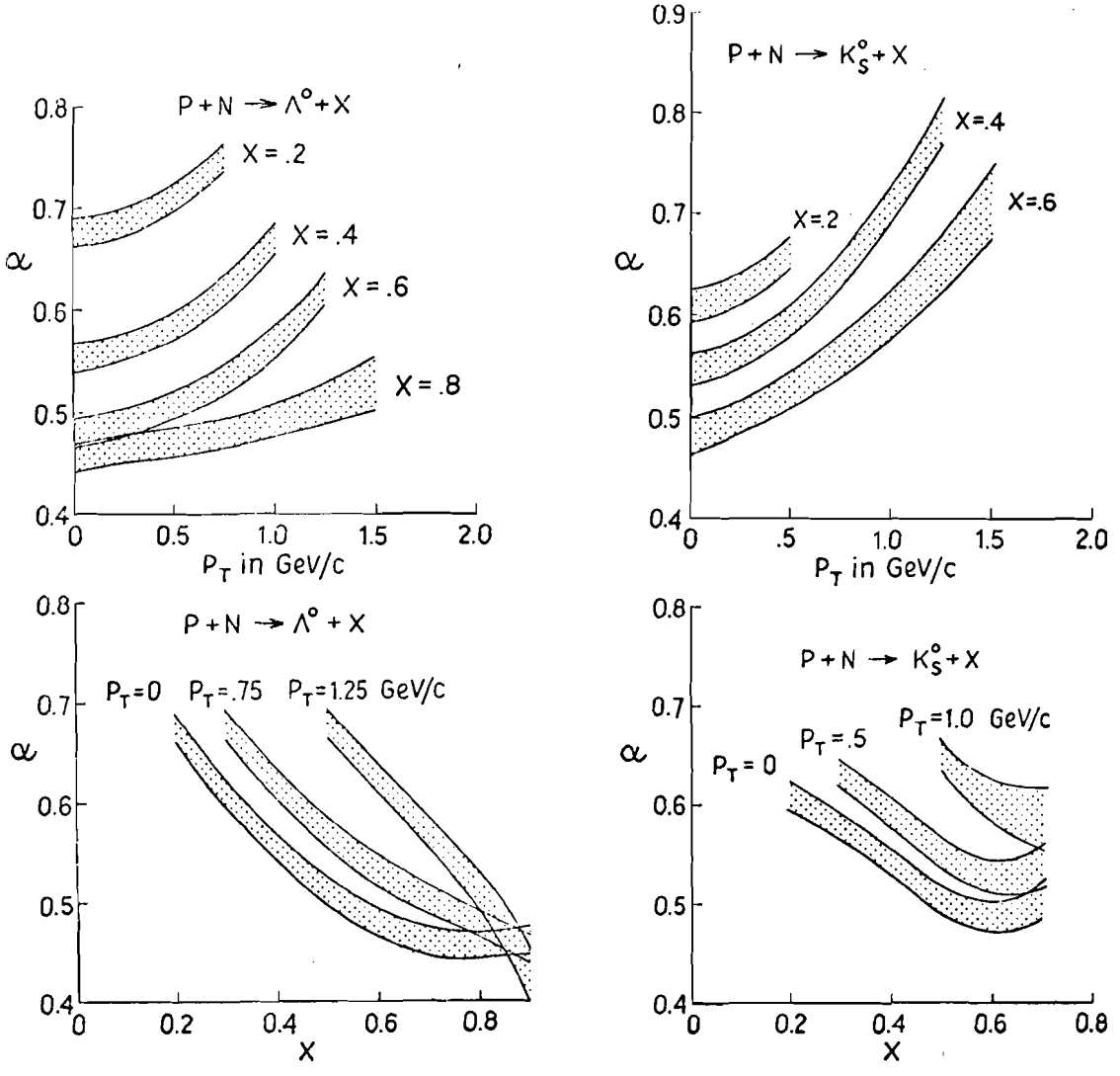

Fig. 19. $\alpha(x,p)$ versus x and p_T for Λ^0 and K^0_S.

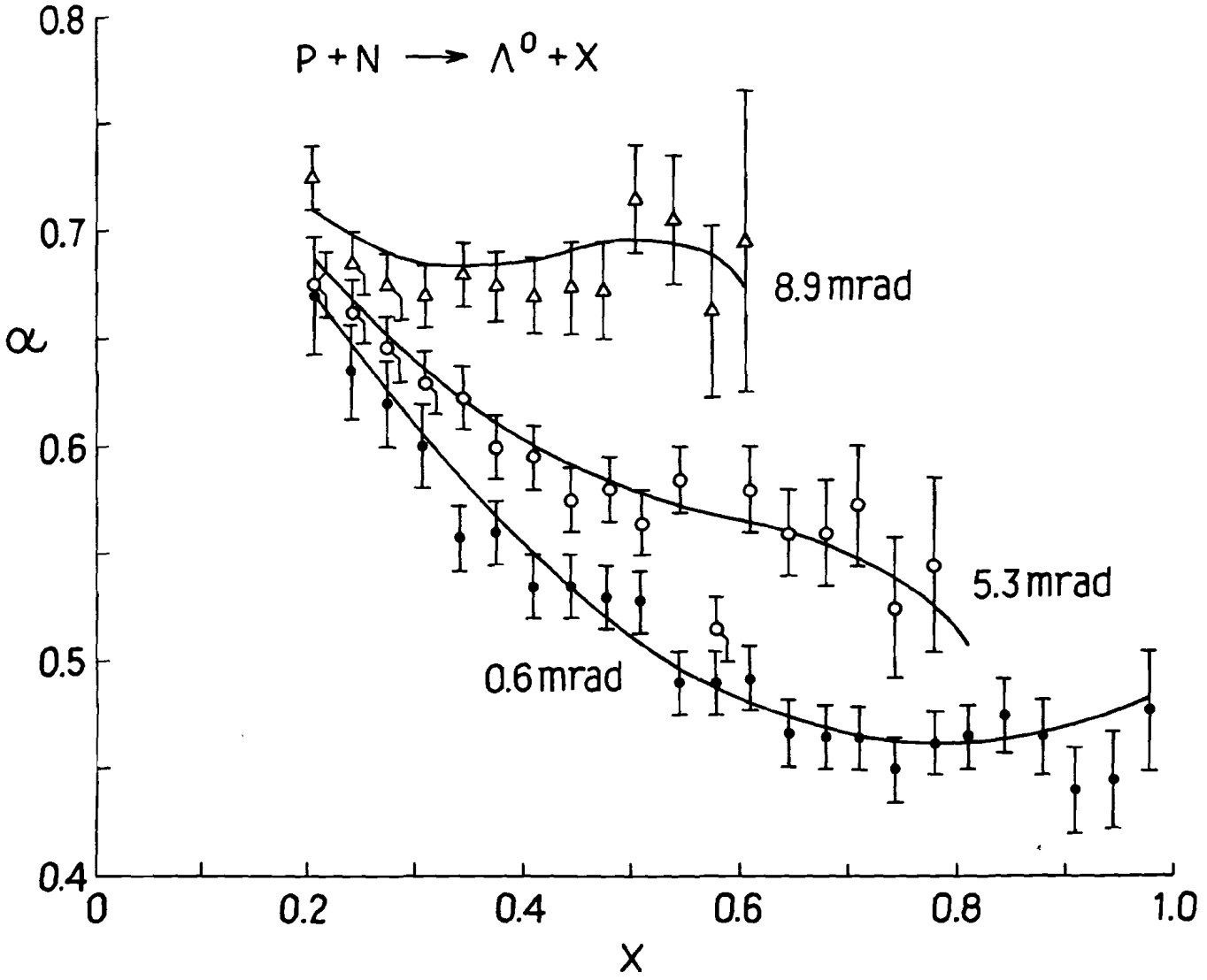

Fig. 19a. $\alpha(x,p_T)$ calculated from the Be and Pb data of Appendix C versus x for Λ°. The solid lines were calculated with the fit parameters in Table 2.

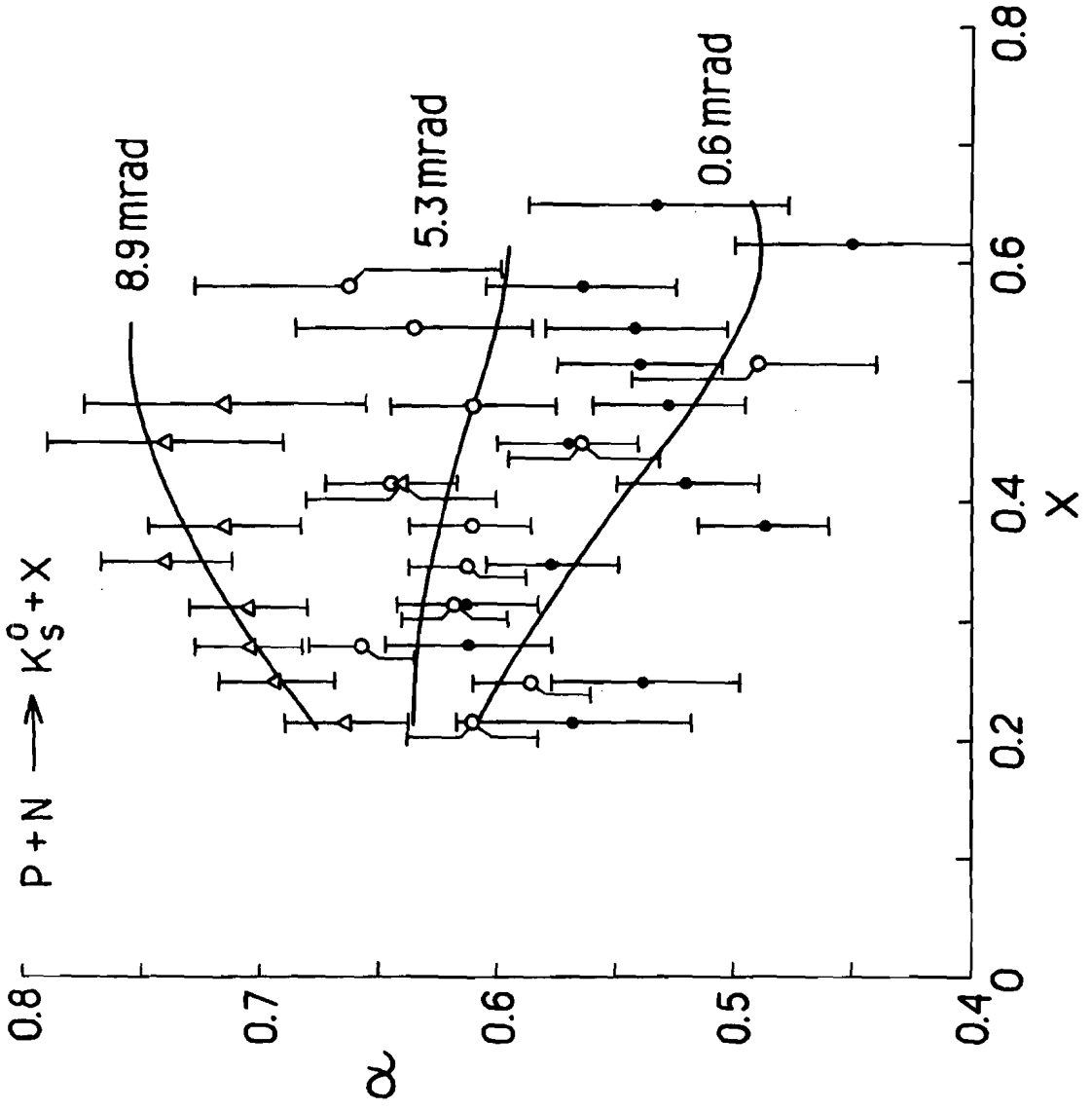

Fig. 19b. $\alpha(x,p_T)$ calculated from the Be and Pb data of Appendix C versus x for K_S^0. The solid lines were calculated with the fit parameters in Table 2.

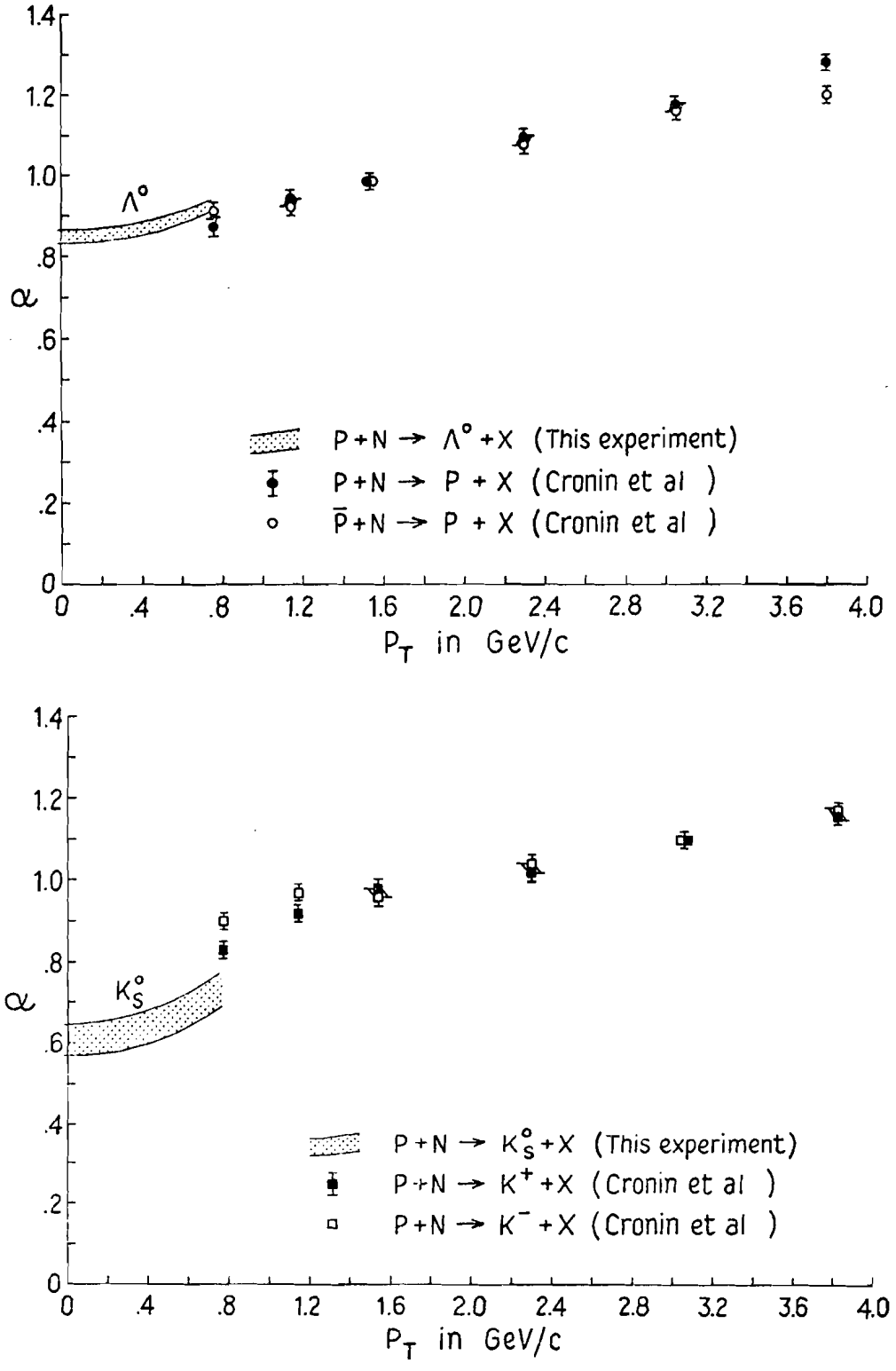

Fig. 20. α extrapolated to x=0 for Λ° and K°_S compared to the data of Reference 24.

The fits were extrapolated to x=0 and the values of α obtained are compared in Figure 20 to the values of α found at x=0 by Cronin et al.[24] in proton and charged kaon production by 200 to 400 GeV/c protons. α at x=0 for Λ^0 agrees well with the trend observed in proton production and α for K_S^0 is in reasonable agreement with α for K^+ and K^- production. The behavior of $\alpha(x,p_T)$ for K_S^0 is very similar to that for Λ^0 over the kinematic region where K_S^0 data exists. Little variation of α was seen for $\bar{\Lambda}^0$, however the x region sampled is limited for $\bar{\Lambda}^0$ and the statistical precision is poor so a variation of α similar to that for Λ^0 cannot be ruled out.

B. Extrapolation of The Invariant Cross Section To A=1

Based on the power law of Equation (IV.1), it is possible to perform an extrapolation to A=1 to extract the proton-nucleon invariant cross section. The extrapolation must be done with a different value of the exponent for each point because α is a strong function of x and p_T. Such an extrapolation does not account for systematic error due to the possible non-power law behavior of the invariant cross section for small A. The proton-nucleus absorption cross sections in the momentum range 20 to 60 GeV/c obey a power law similar to Equation (IV.1) with α=0.70.[44] However, the absorption cross section obtained by extrapolating the power law to A=1 is 35% larger than the measured proton-proton absorption cross section. Therefore it is possible that a

similar normalization error of 35% results from such an extrapolation in the case of inclusive cross sections.

The extrapolated cross section can be directly calculated from the Be and Pb cross sections for each momentum and angle bin as follows:

$$f_N = f_{Be}^b / f_{Pb}^a$$
$$a = \log(A_{Be})/\log(A_{Pb}/A_{Be}) = 0.70$$
$$b = \log(A_{Pb})/\log(A_{Pb}/A_{Be}) = 1.70.$$

The copper data do not enter in the calculation but serve as a consistency check indicating that the power law is obeyed. The extrapolated cross sections for Λ^0, $\bar{\Lambda}^0$, and K_S^0 were fit to empirical functions of x and p_T in the same manner as the directly measured data and the parameter values are given in Table 2.

C. Comparison Of The Λ^0 Extrapolated Cross Section With The Thermodynamic Model

The extrapolated cross section can be compared with the predictions of the thermodynamic model of Hagedorn and Ranft[45] for Λ^0 production from hydrogen at 300 GeV/c. This comparison is shown in Figure 21 where $(1/\sigma_{abs})d^2\sigma/dpd\Omega$ in particles/(GeV/c)(sr)(interacting proton) calculated from the fit to the extrapolated cross section is plotted versus laboratory momentum for various production angles. The

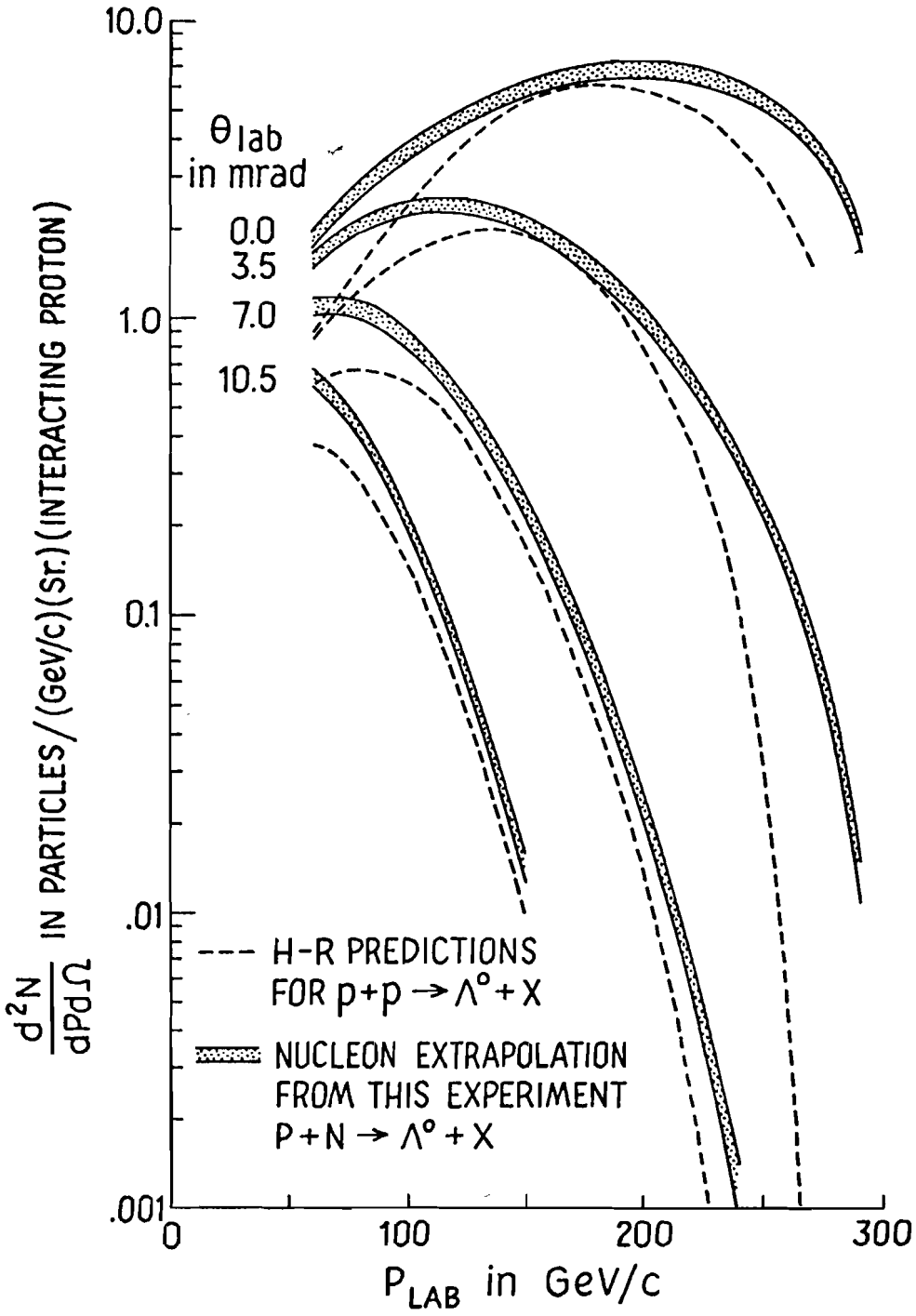

Fig. 21. Fit to Λ° cross section extrapolated to A=1 compared to the Thermodynamic Model of Reference 45.

proton absorption cross section, σ_{abs}, was taken to be 33 mb.[43] The absolute normalization of the 0 mr peak and the shape above 100 GeV/c for 7 and 10 mr agree well with the prediction while the 0 and 3.5 mr contours are somewhat flatter than those predicted. Overall the model is consistent with the gross features of the data.

D. The Λ^0 Spectra

Figure 22(a) shows the differential invariant cross section versus x for nuclear targets Be and Pb divided by $A^{2/3}$ for contours in p_T^2 of 0, 0.5, 1.0, and 1.5 $(GeV/c)^2$. The dashed and dotted lines are the fits to the Be and Pb data respectively and the solid line is the fit to the differential cross section extrapolated to A=1. It should be emphasized that the lines represent fits to all the data at once and are not fits only to the data points displayed in the figure.

In the reaction $p+p \rightarrow p+X$[26,46-48] peaks have been observed in the forward and backward directions near $x=\pm 1$ which have been interpreted as arising from the fragmentation of the projectile and target protons respectively. For $p+p \rightarrow \pi^+ + X$[26,46,48,49], however, the cross section is greatest at x=0 and decreases as |x| increases showing that most π's are produced in the central region near x=0 . Recent bubble chamber experiments[48-53] indicate that similar behavior occurs in the case of neutral strange

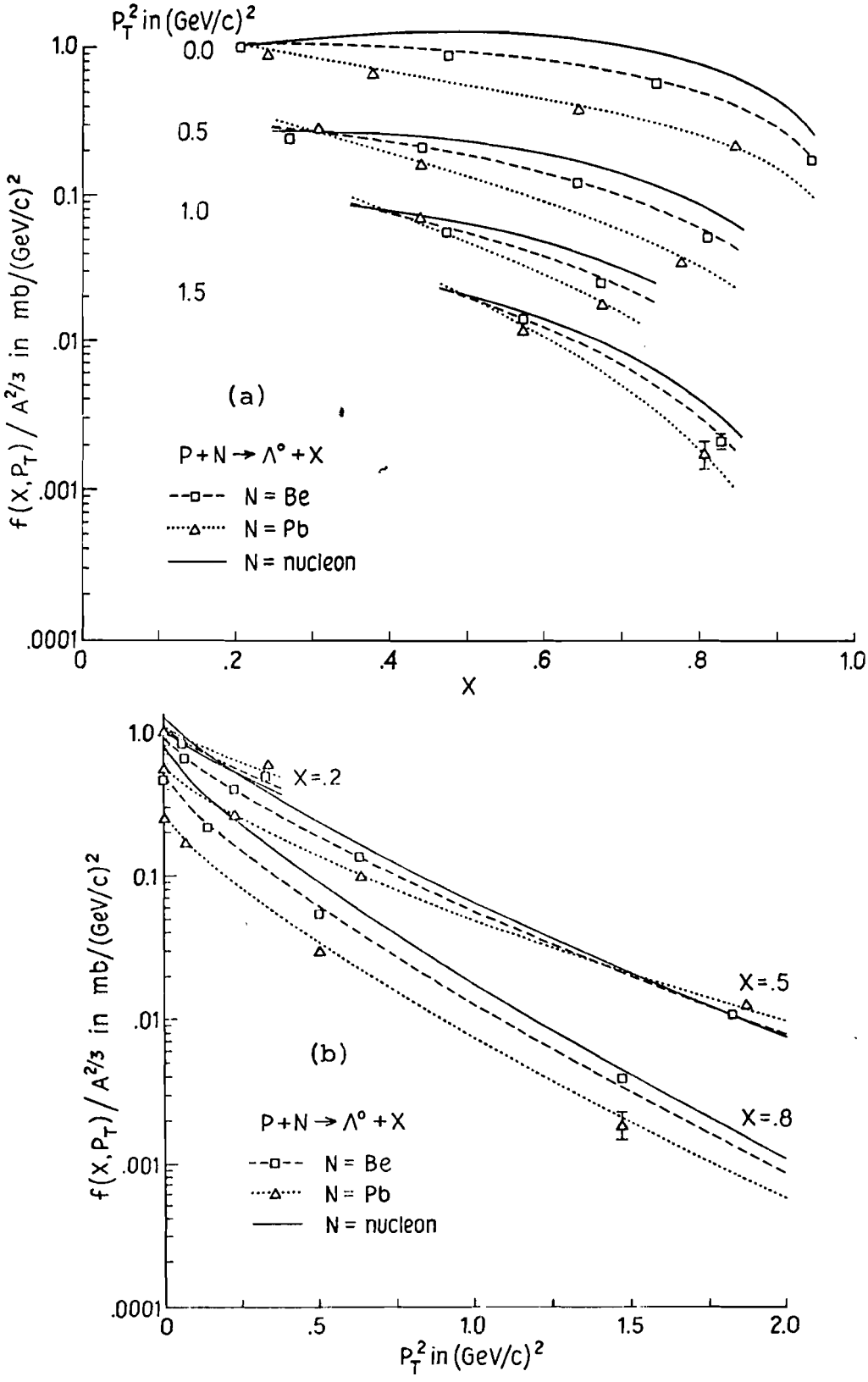

Fig. 22. Invariant cross section divided by $A^{2/3}$ for Λ° production versus (a) x and (b) p_T^2. The lines are the results of fits to all the data for each target.

particles.

The extrapolated distribution at $p_T^2=0$ has a broad plateau extending from x=0.3 to x=0.7 indicating that significant Λ^0 production occurs in the projectile fragmentation region. A dip in the distribution is evident at low x hinting that production is depleted in the central region. The distributions fall more steeply with x as p_T^2 increases which shows that the x behavior is not completely independent of the p_T behavior.

The x distributions for the nuclear targets are distorted in a p_T^2 dependent manner. The Pb distribution at $p_T^2=0$ increases as x becomes small and there is no sign of a dip at x=0. This enhancement at low x is greater as p_T^2 increases and is more pronounced for Pb than for Be. The general A behavior is indicative of a mechanism inside the nucleus which degrades the longitudinal momentum of produced particles and results in excess particles in the low x region while depleting the x distribution at high x. Therefore, the total number of produced particles per interaction integrated over all x is roughly independent of A.

Figure 22(b) shows the Λ^0 invariant cross section for constant x contours of 0.2, 0.5, and 0.8 as a function of p_T^2. The shape is not consistent with a simple exponential in p_T^2 and the slope becomes more shallow as p_T^2 increases. The slope of the p_T^2 contour also becomes more shallow as x

decreases. The p_T^2 distributions depend less on the atomic mass number of the target as x increases and for x=0.8 there is almost no difference in shape between Be, Pb and the extrapolated contours.

Figure 23(a) shows the Λ^0 differential multiplicity,

$$d^2n/dydp_T^2=(1/\sigma_{abs})(d^2\sigma/dydp_T^2)=(\pi/\sigma_{abs})(Ed^3\sigma/d\vec{p}^3)$$

at $p_T^2=0$ for Be, Cu, and Pb as a function of laboratory rapidity,

$$y=(1/2)\ln[(E+p_L)/(E-p_L)],$$

where E is the Λ^0 laboratory energy, p_L is the component of the Λ^0 momentum parallel to the incident proton direction in the laboratory reference frame and σ_{abs} is the proton absorption length for the target. The values of σ_{abs} were taken from the measurements of Denisov et al.[44] in the momentum range 20-60 GeV/c and were 210±2 mb, 796±8 mb, and 1812±35 mb for Be, Cu, and Pb respectively. The differential multiplicity is depleted for y>5 for the Pb and Cu targets relative to the Be target. The distributions are approximately equal at the lowest accessible value of y(=4.75) suggesting that an enhancement occurs at lower y values for the high A targets.

The Energy Flux Cascade Model of Gottfried,[20] predicts a discontinuity in the y distribution of the multiplicity integrated over p_T^2 at $y=(1/2)y_{projectile}$ or

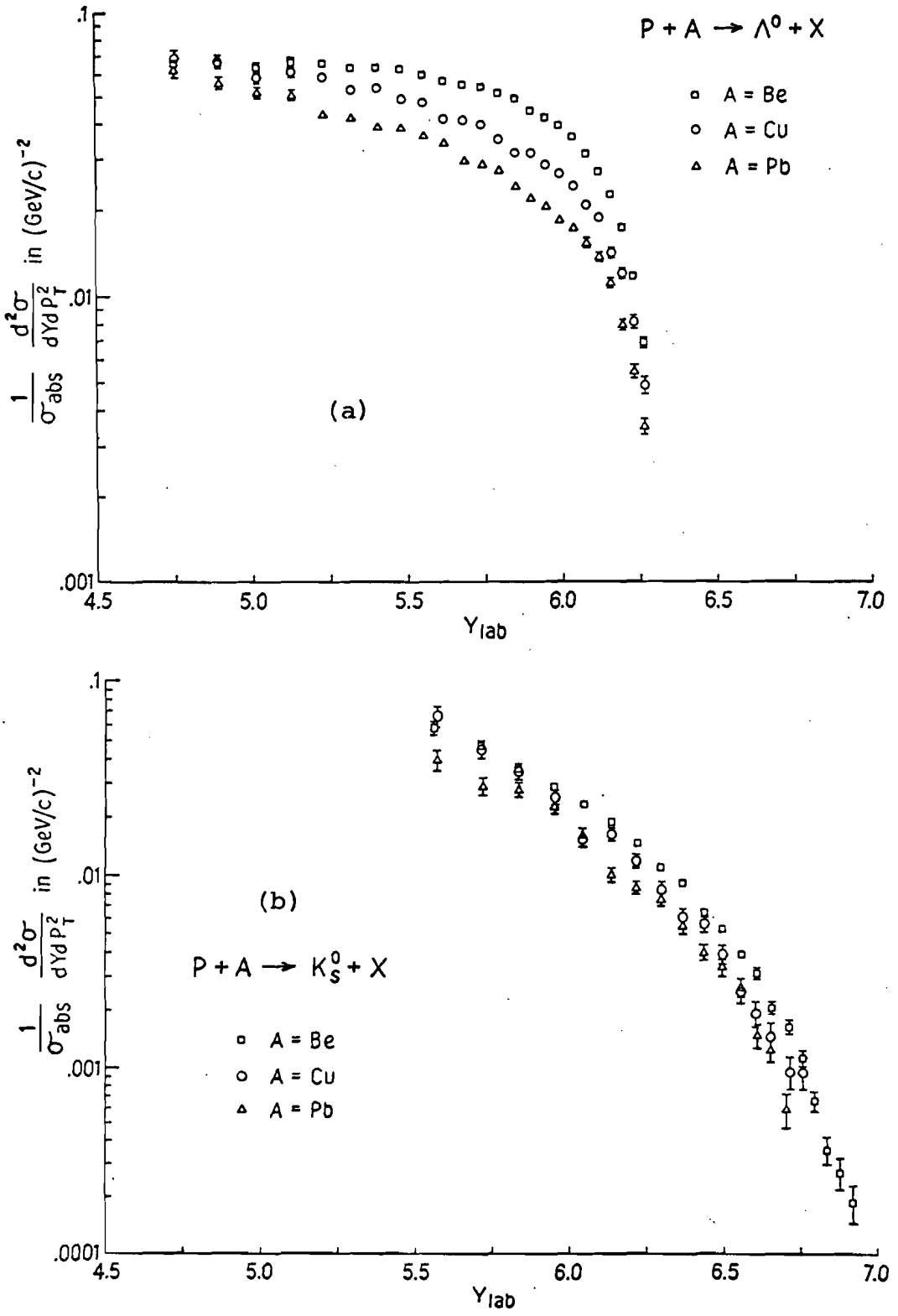

Fig. 23. Double differential multiplicity versus laboratory rapidity for (a) Λ^0 and (b) K_S^0 production.

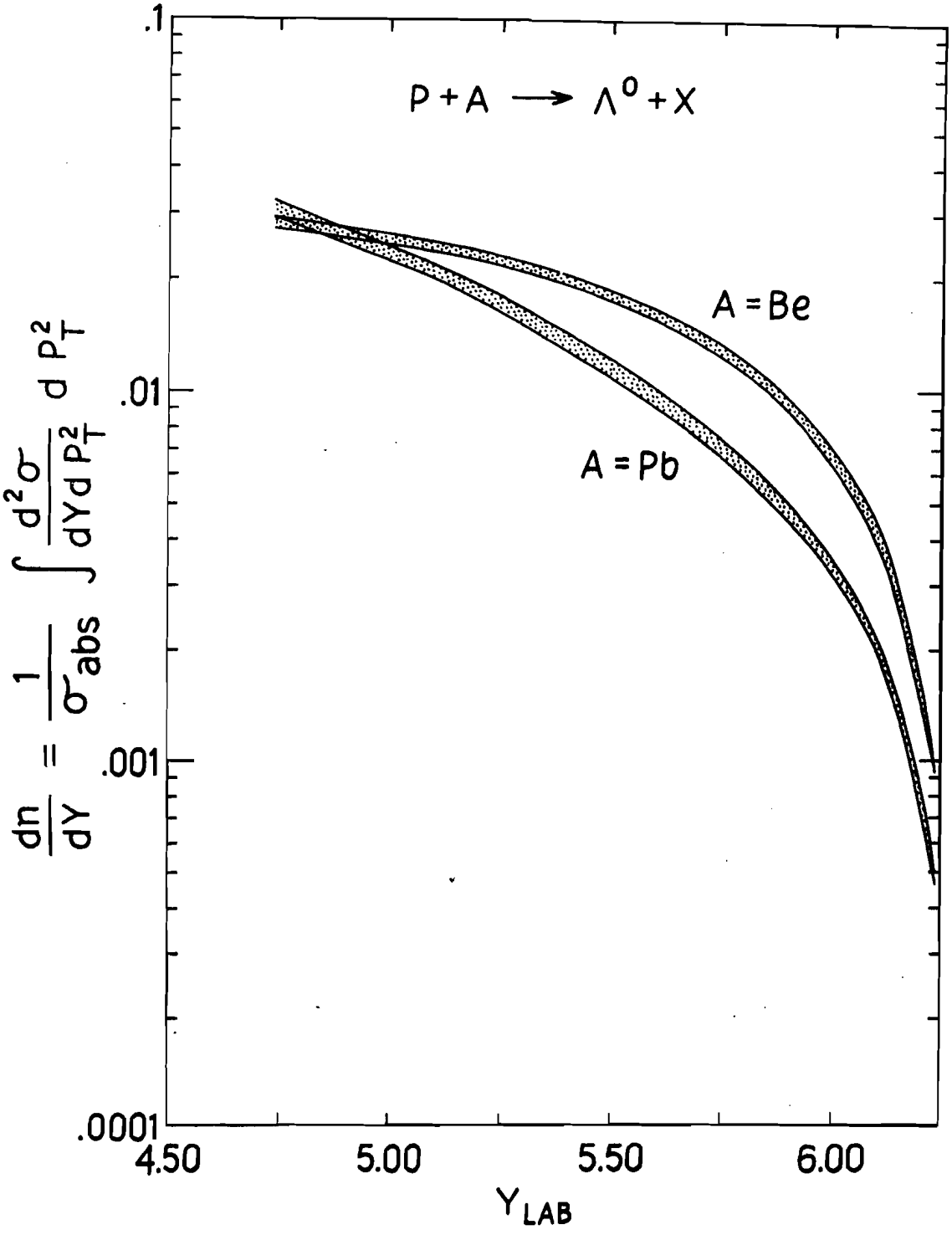

Fig. 23c. Single differential multiplicity calculated with the fit parameters in Table 2 versus laboratory rapidity for Λ°.

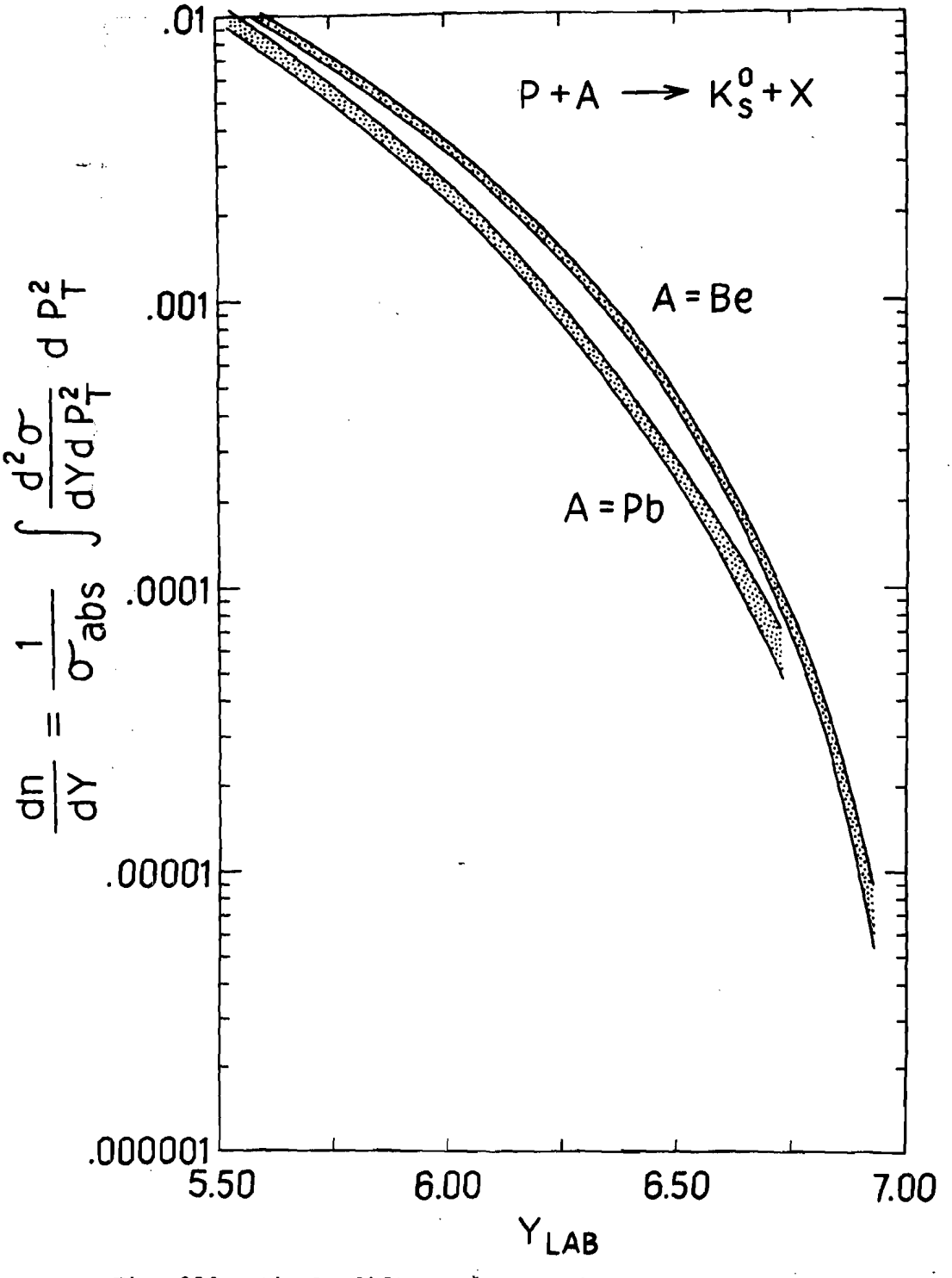

Fig. 23d. Single differential multiplicity calculated with the fit parameters in Table 2 versus laboratory rapidity for K^{o}_{S}.

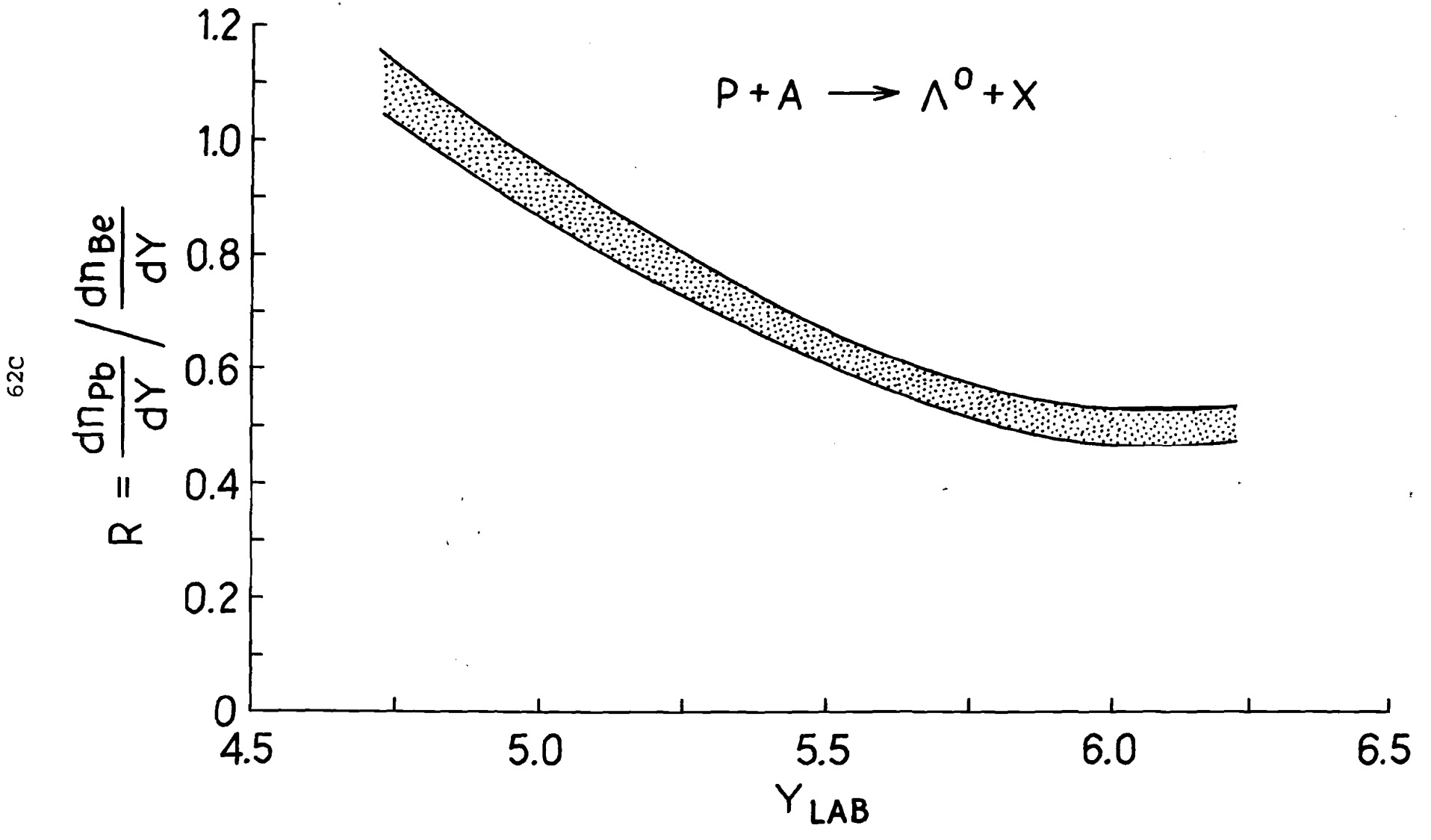

62C

Fig. 23e. The ratio of the single differential multiplicity for the Pb target to that for the Be target versus laboratory rapidity for Λ^0.

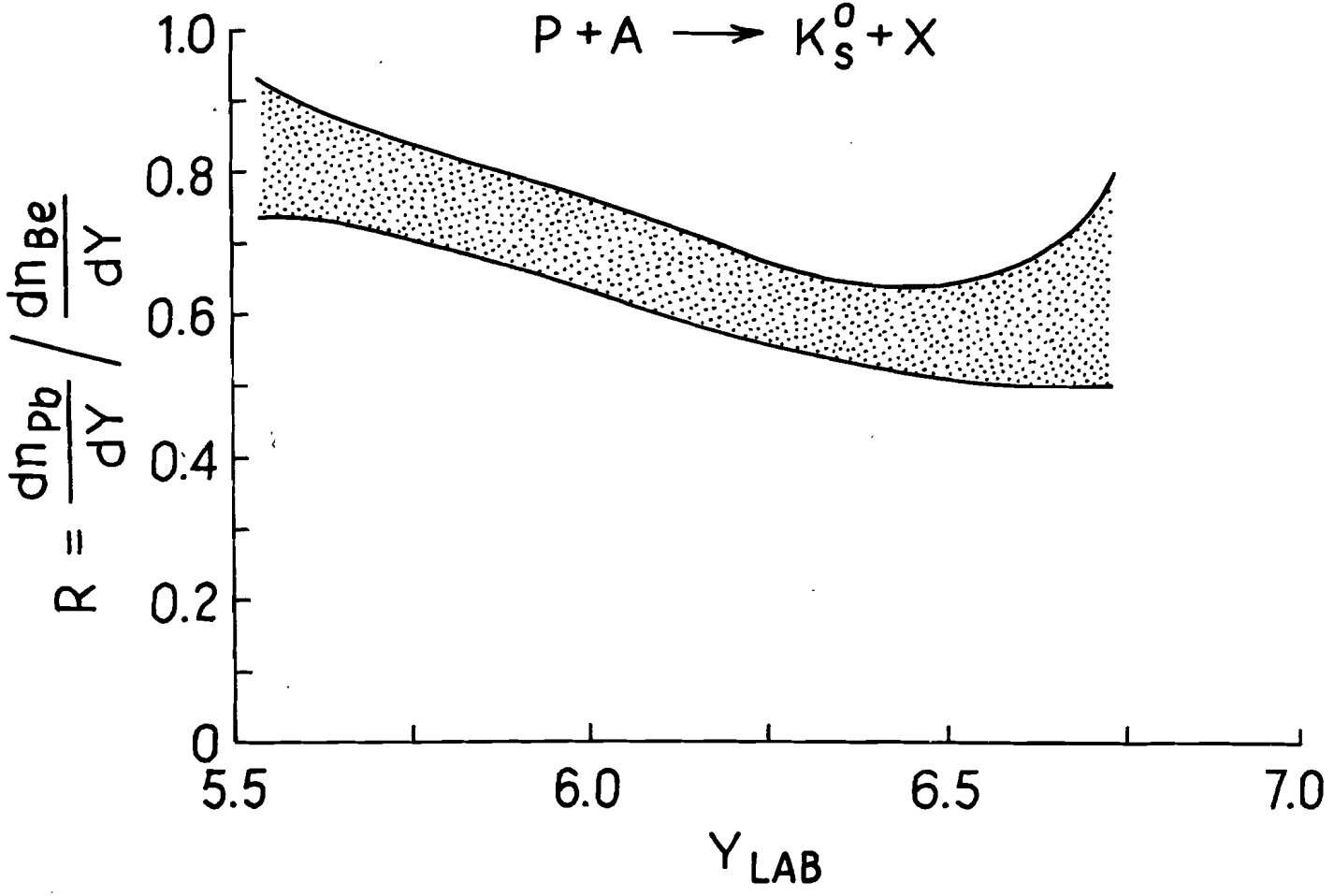

Fig. 23f. The ratio of the single differential multiplicity for the Pb target to that for the Be target versus laboratory rapidity for K^o_S.

$y=(1/3)y_{projectile}$ while predicting no A dependence for larger y.[21] On the other hand, the Two Phase Model of Reference 22 and the Independent Reaction Model of Reference 23, both predict a continuous A dependence in the y distribution. The data shown in Figure 23 seem to be in disagreement with the Energy Flux Cascade Model.

The fit to the extrapolated differential cross section was numerically integrated over p_T^2 to obtain the structure function:

$$F_1(x) \equiv (2/\pi/s)\int (Ed^2\sigma/dxdp_T^2)dp_T^2$$

which has been directly measured by several bubble chamber experiments.[48-53] The extrapolated fit was used as the best approximation to the proton-proton interaction studied in these experiments. The bubble chamber experiments observed neutral strange particle production in the backward hemisphere in the laboratory whereas in this experiment the observed particles were in the forward hemisphere. The integration was performed from $p_T^2=0$ to $p_T^2=10$ after which the contribution to the integral was negligible. Figure 24(a) shows $F_1(x)$ for the extrapolated Λ^0 fit compared to hydrogen bubble chamber experiments with incident proton energies of 12,[48] 24,[48] 102,[53] 205,[50] and 300[52] GeV. The shaded area of Figure 24 indicates the error in the calculation of $F_1(x)$ due to the uncertainty in absolute normalization not including possible systematic error

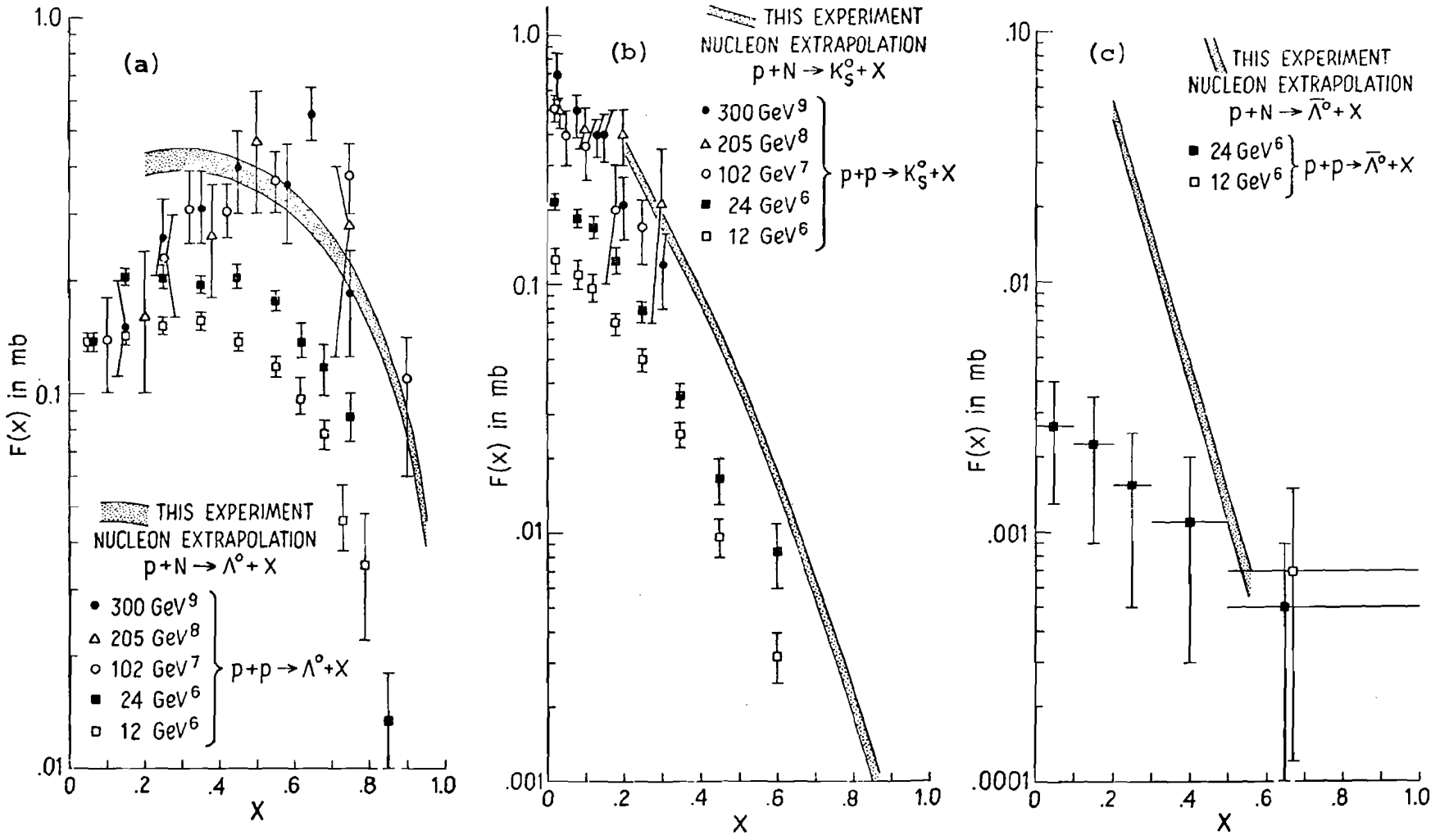

Fig. 24. $F_1(x)$ for (a) Λ^0, (b) K^0_S, and (c) $\bar{\Lambda}^0$ production.

arising from the nucleon extrapolation.

F_1 as calculated from the extrapolated fit is in good agreement with the 102-300 GeV bubble chamber data for x>0.3. Below x=0.3 there may be disgreement however we have no data below an x of 0.2 and the range in p_T^2 is limited at low x. The shape agrees well with the 12 and 24 GeV data but the absolute normalization is about a factor of two larger. The bubble chamber data indicate that the invariant cross section is independent of incident proton energy above 100 GeV.

E. The K_S^0 Spectra

Figure 25(a) shows the invariant cross section divided by $A^{2/3}$ for K_S^0 as a function of x for p_T^2=0, 0.5, and 1.0 $(GeV/c)^2$. The shape of the K_S^0 x distributions can be roughly approximated by an exponential in x for x<0.5. The extrapolated x distributions monotonically rise as x decreases indicating that K_S^0 production is dominated by the production mechanism in the central region. The shapes of the x distributions are weakly dependent on p_T^2 and the slope of the x contours is steeper for larger p_T^2. A non-exponential behavior is evident for x>0.5, particularly for Be at p_T^2=0 for which the greatest amount of high-x K_S^0 data exists. The x distributions are similar to those of the $\pi^\pm$ mesons from p-p interactions[26,46-49] which are also produced mainly in the central region. The A dependence for

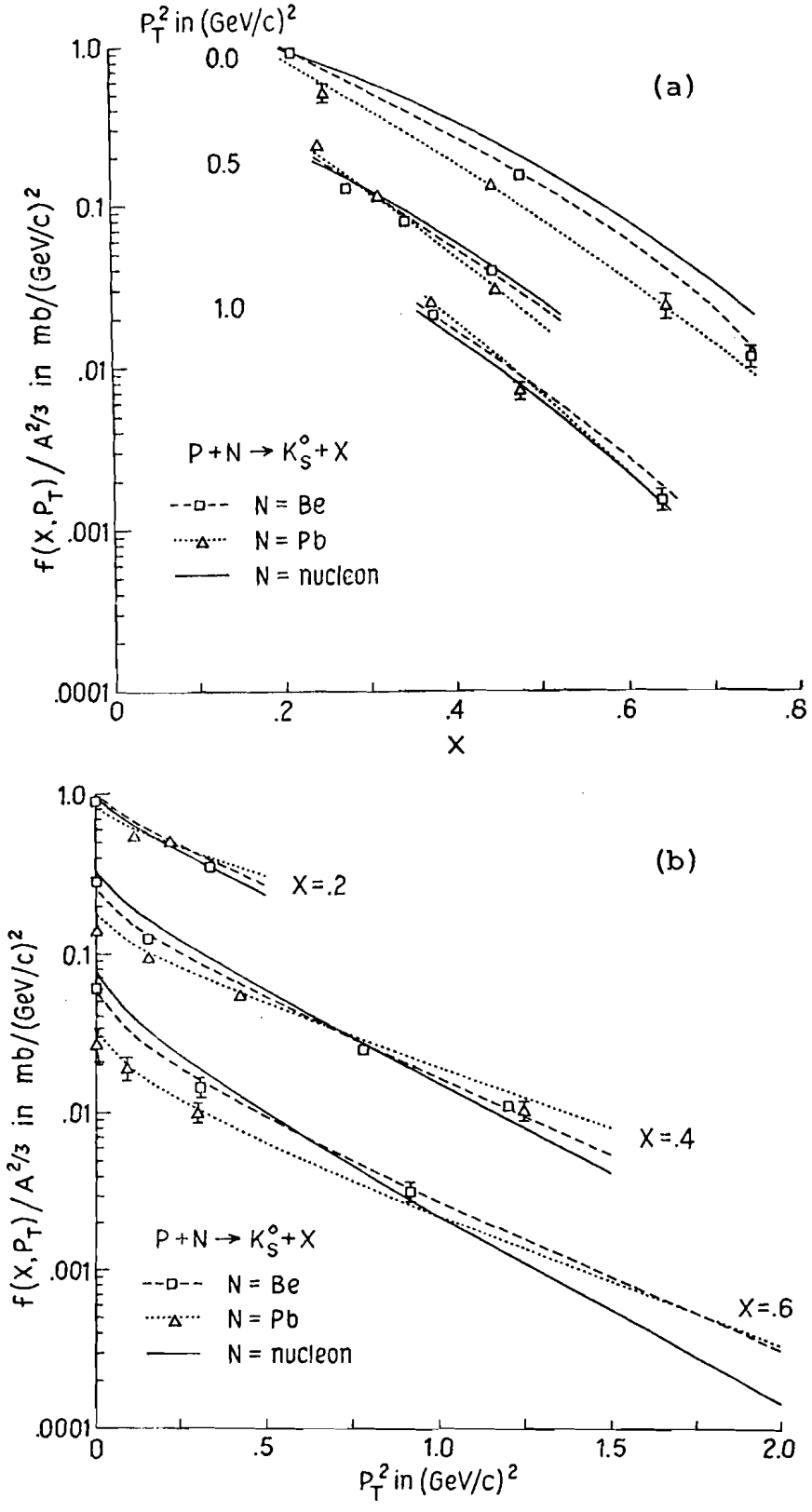

Fig. 25. Invariant cross section divided by $A^{2/3}$ for K_S^o production versus (a) x and (b) p_T^2. The lines are the results of fits to all the data for each target.

the K_S^0 is very similar to that for the Λ^0 with a high A enhancement at low x and high p_T^2.

Figure 25(b) shows the K_S^0 invariant cross section versus p_T^2 for x contours of 0.2, 0.4, and 0.6. The general behavior of the invariant cross section with p_T^2 is remarkably similar to that for the Λ^0 and a simple exponential in p_T^2 does not adequately represent the data.

Figure 23(b) shows the K_S^0 differential multiplicity versus laboratory rapidity for $p_T^2=0$ and for Be, Cu, and Pb. The behavior with y, although considerably less pronounced, is similar to that of the Λ^0. The distribution is increasingly depleted for y>5.5 as A increases.

$F_1(x)$ was calculated for the K_S^0 in the same way as for the Λ^0 and is compared with the hydrogen bubble chamber data of References 48-53 in Figure 24(b). The normalization is in good agreement with the bubble chamber data of 102-300 GeV and the shape agrees well with the low energy data of 12 and 24 GeV. There is a factor of 3 difference in normalization between the data of 24 and 300 GeV.

F. The $\bar{\Lambda}^0$ Spectra

Figure 26(a) shows the invariant cross section for $\bar{\Lambda}^0$ versus x for $p_T^2=0$ and 0.5 GeV/c^2. The data are consistent with a simple exponential dependence on x. There is no evidence of a target dependence although the region of x

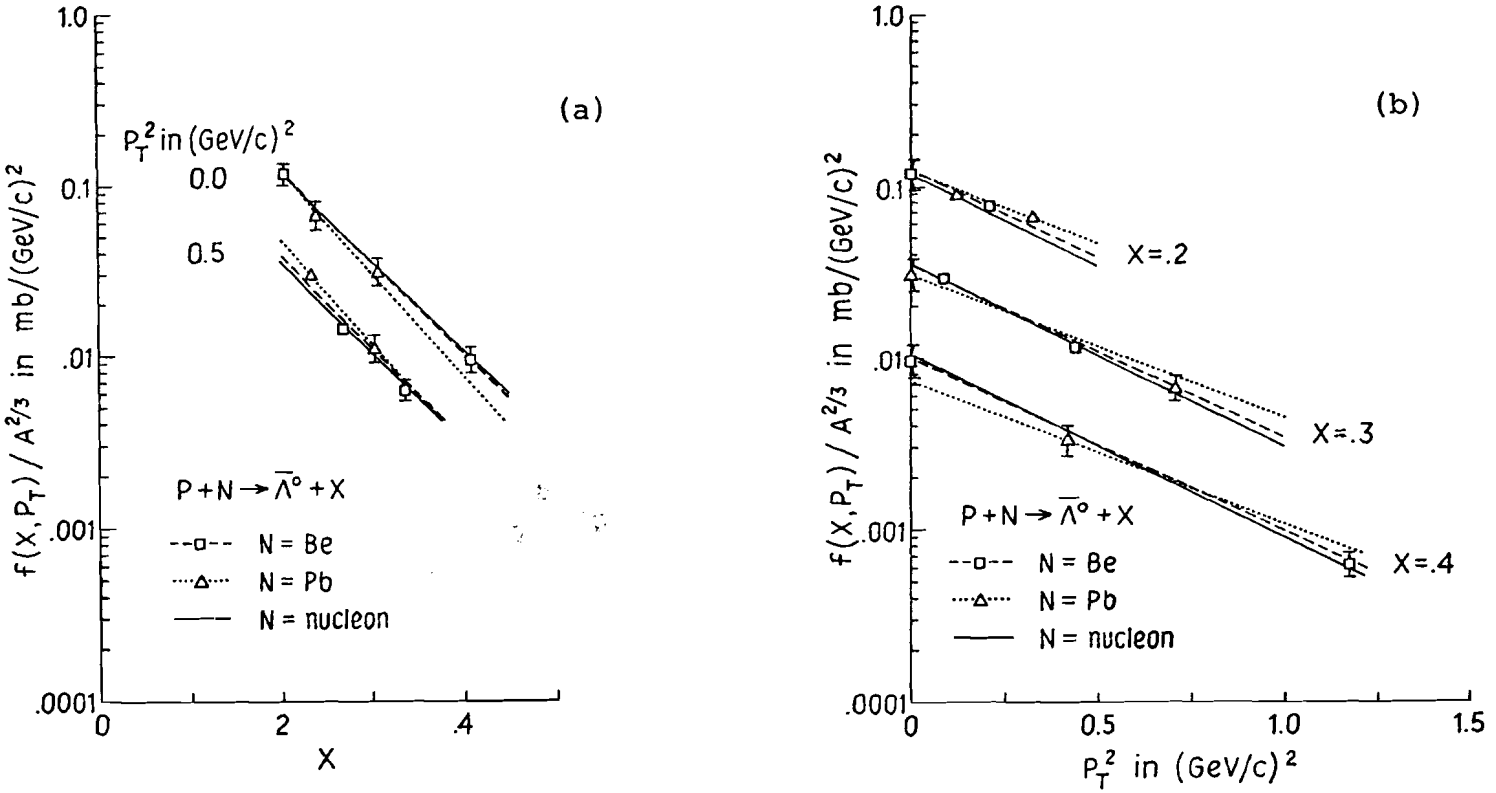

Fig. 26. Invariant cross section divided by $A^{2/3}$ for $\bar{\Lambda}^\circ$ production versus (a) x and (b) p_T^2. The lines are the results of fits to all the data for each target.

sampled by the data is small and the statistical errors are large so a target dependence similar to that of the Λ^0 and K_s^0 cannot be ruled out. Clearly $\bar{\Lambda}^0$ production mainly occurs in the central region and the x distributions for Λ^0 and $\bar{\Lambda}^0$ are consistent with nearly equal production of both particles in the region near x=0.

Figure 26(b) shows the invariant cross section for $\bar{\Lambda}^0$ versus p_T^2 for x=0.2, 0.4, and 0.6. The p_T^2 dependence is consistent with a exponential in p_T^2 and the p_T^2 dependence is similar to that of the Λ^0 and K_s^0. It would seem that the production mechanism for Λ^0, $\bar{\Lambda}^0$, and K_s^0 distinguishes between the three particles primarily as a function of x.

$F_1(x)$ for $\bar{\Lambda}^0$ is shown in Figure 24(c) along with the hydrogen bubble chamber data at 12 and 24 GeV.[48] The slope of $F_1(x)$ calculated from the extrapolated fit is much steeper than that of the low energy data so production of $\bar{\Lambda}^0$ is considerably greater near x=0 at 300 GeV than at 24 GeV.

G. Particle Ratios

Figure 27 shows the K_s^0/Λ^0 ratio versus x for Be and Pb targets and for production angles of 0.6, 3.3, and 8.9 mr. The line represents a fit of all the data to the function:

$$K_s^0/\Lambda^0 = A_1 \exp(A_2 x)$$

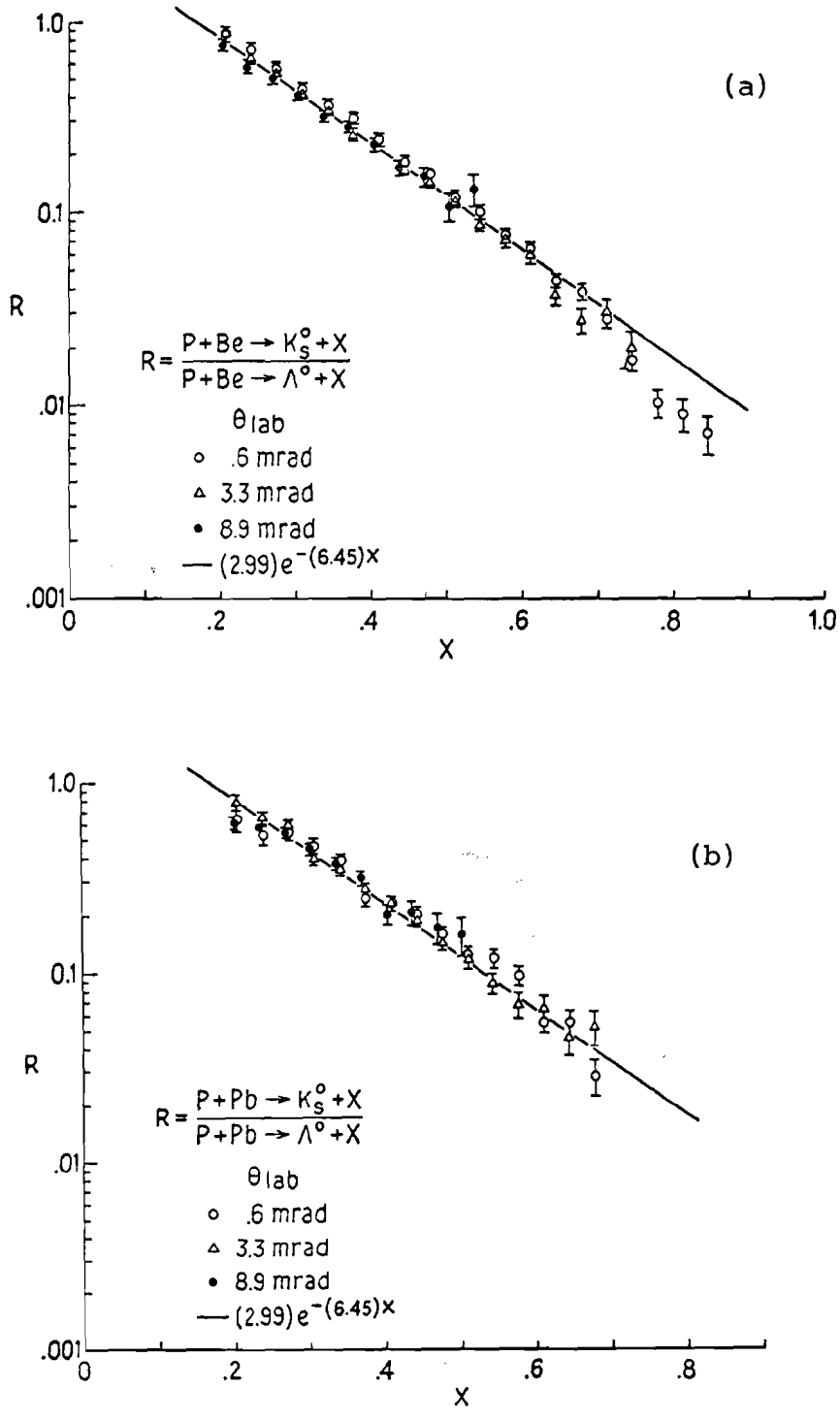

Fig. 27. K^0_S/Λ^0 ratio for (a) Be and (b) Pb. The line is the result of a fit to all the data.

where the fit gave $A_1=2.99\pm0.04$ and $A_2=-6.45\pm0.03$ with a $\chi^2=727$ for 375 data points. Within the statistical accuracy of this experiment, the K^0_S/Λ^0 ratio does not depend on p_T^2 or on the target. The K^0_S/Λ^0 ratio extrapolates to 3 at x=0 indicating the abundance of mesons produced in the central region.

Figure 28 shows the $\bar{\Lambda}^0/\Lambda^0$ ratio versus x for Be and Pb for production angles of 0.6, 3.3, and 8.9 mr. Again the line represents a fit of all the data to the function:

$$\bar{\Lambda}^0/\Lambda^0=A_1\exp(A_2x)$$

where the fit gave $A_1=1.16\pm0.05$, $A_2=-11.4\pm0.15$ with $\chi^2=158$ for 165 data points. No p_T^2 or target dependence is observed in the ratio. The $\bar{\Lambda}^0/\Lambda^0$ ratio extrapolated to x=0 is consistent with 1, hinting that perhaps production of baryon-antibaryon pairs dominates in the central region.

H. Inclusive Λ^0 Polarization

It has been reported by our group,[54] that a significant polarization was observed in the inclusive production of Λ^0's at non-zero production angles. The three components of the polarization vector were measured in the chamber reference system using the maximum-likelihood method and only the components consistent with parity conservation were

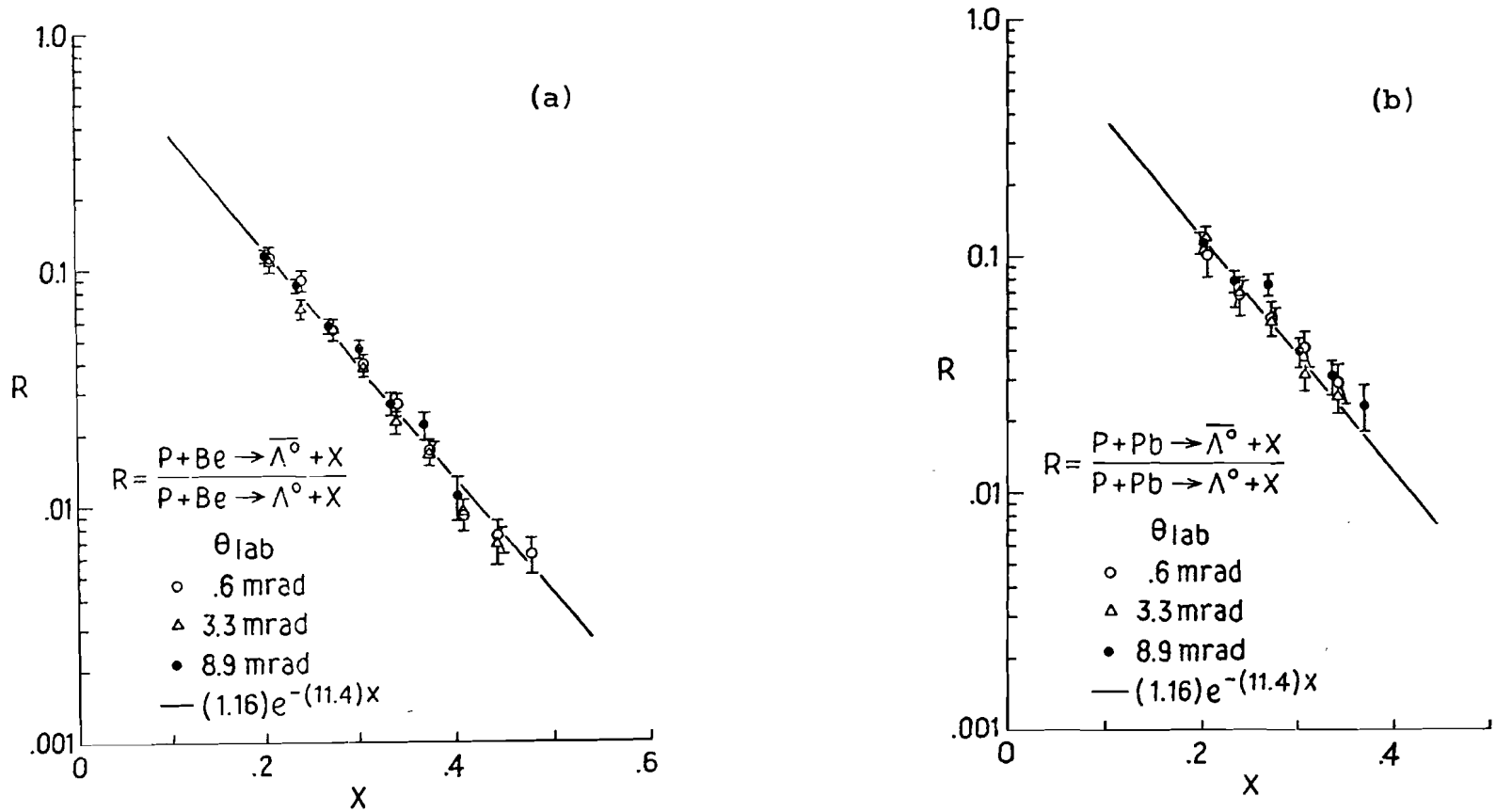

Fig. 28. $\bar{\Lambda}^0/\Lambda^0$ ratio for (a) Be and (b) Pb. The line is the result of a fit to all the data.

found to be non-zero. In the chamber reference system the z axis points in the proton beam direction for nominal zero production angle, the y axis points upwards, and the x axis points to the left. It is assumed here that the incident beam is deflected vertically for non-zero production angles. Parity conservation implies that the spin of produced particles must be normal to the scattering plane. In this experiment the initial spin direction must therefore be along the x axis, however as the produced particle traverses the magnetic field in the sweeper, the spin precesses and therefore the x and z components are allowed.

The three components of the polarization times the decay asymmetry parameter $\alpha(=0.647\pm0.013$[55]$)$ are shown in Figure 29 versus transverse momentum. Since no variation of $\alpha\vec{P}$ with x was observed, all x bins were combined. Figure 29(d) shows $|\alpha P|=[(\alpha\vec{P}\cdot\hat{x})^2+(\alpha\vec{P}\cdot\hat{z})^2]^{1/2}$ versus transverse momentum. $|\alpha P|$ increases monotonically with p_T from $p_T=0.2$ GeV/c to the maximum observable p_T of 1.5 GeV/c for which $P=0.28\pm0.08$.

A polarization consistent in magnitude and sign with that reported here has been measured in Λ^0 production from Be in the 24 GeV CERN neutral kaon beam.[56]

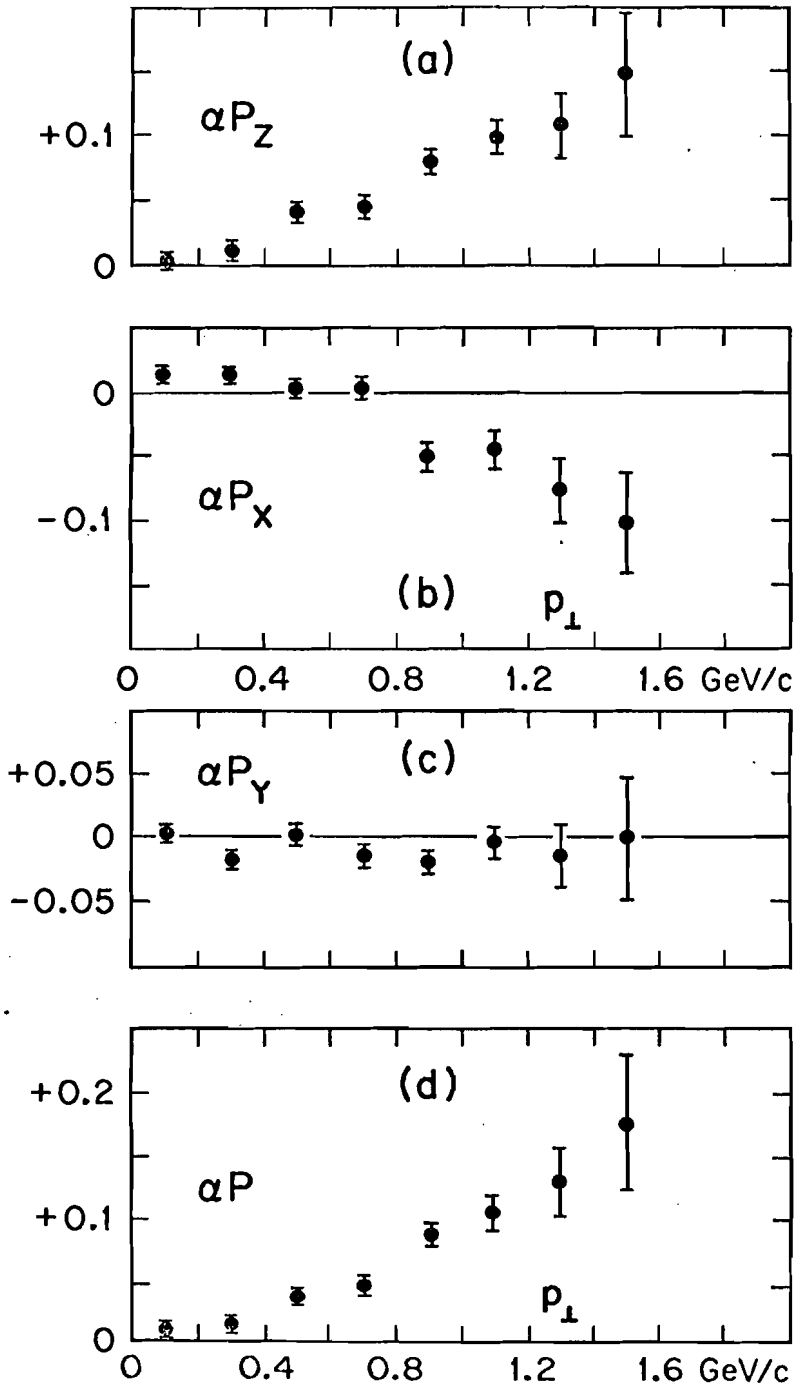

Fig. 29. Components of inclusive Λ^0 polarization times the asymmetry parameter α. (a) αP_x, (b) αP_y, (c) αP_z and (d) $|\alpha P|$.

CHAPTER V

PHENOMENOLOGICAL FITS TO THE CROSS SECTIONS

The empirical fits described in Chapter III gave a convenient representation of the data in terms of the useful kinematic variables x and p_T^2. The fits to the extrapolated cross sections were investigated more carefully in the hope of finding a more simple functional form. In some cases more than one function or set of kinematic variables could be used to successfully represent the data. In the high x region the Λ^0 data are consistent with a functional form predicted by the triple Regge Model.[39]

A. Fits To The Λ^0 Extrapolated Cross Section

The most important term in the empirical fits to the Λ^0 cross sections is the term

$$(1-x)^{c_8+c_9 p_T^2}.$$

It is a striking feature of the data that the invariant cross section has the approximate dependence:

$$Ed^3\sigma/d\vec{p}^3 = \beta\,(1-x)^{a(\theta)}$$

where β is a constant and the power a is a function only of

production angle θ and $a(\theta)$ becomes a larger negative number as θ increases.

The Λ^0 extrapolated cross sections gave a good fit to the simplified function:

$$Ed^3\sigma/d\vec{p}^3 = a_1 \exp[a_2(x-a_3)^2 + a_4(p_T^2+a_5)^{1/2}] \cdot (1-x)^{a_6+a_7 p_T^2}$$

where $a_1=21.4\pm3.2$, $a_2=-1.65\pm0.18$, $a_3=0.866\pm0.062$, $a_4=-3.79\pm0.10$, $a_5=0.304\pm0.026$, $a_6=0.804\pm0.035$, $a_7=0.999\pm0.033$ with a χ^2/degree of freedom(DF) =1.23 with 383 data points. The term $\exp[a_4(p_T^2+a_5)^{1/2}]$ is similar to the term $\exp(aE_T)$, where $E_T=(p_T^2+m^2)^{1/2}$ and m is the mass of the produced particle, which was successfully used to represent the p_T dependence of neutral strange particle production at 19 GeV.[49]

If p_T^2 in the exponent of (1-x) is replaced by the invariant transverse momentum $t = (p_a-p_c)^2$ where p_a and p_c are the 4-momenta of particles a and c in reaction a+b→c+X, the χ^2/DF decreases to 1.14 and a_5(=0.019±0.007) becomes small. Therefore the function can be further simplified by fixing a_5 and setting it equal to zero and one obtains $a_1=5.20\pm0.091$, $a_2=-1.50\pm0.18$, $a_3=0.327\pm0.018$, $a_4=-1.00\pm0.032$ $a_6=0.771\pm0.034$, $a_7=-1.46\pm0.022$ with χ^2/DF = 1.20. If either a_2 or a_3 is set equal to zero the χ^2/DF increases only slightly to 1.35. Therefore one obtains the following suprisingly simple function which gives a good fit to the

extrapolated Λ^0 data:

$$Ed^3\sigma/d\vec{p}^3=b_1\exp[b_2p_T](1-x)^{b_3+b_4t} \quad (V.1)$$

where $b_1=5.71\pm0.081$, $b_2=-1.01\pm0.031$, $b_3=1.02\pm0.008$, $b_4=-1.45\pm0.020$. If t is replaced by p_T^2 (p_T) the fit becomes very poor with $\chi^2/DF = 7.7$ (17.7). If p_T in Equation (V.1) is replaced by t one obtains a $\chi^2/DF = 3.7$. However x can be replaced by the radial scaling variable $x_R=E^*/E^*_{max}$ where E^* is the energy of the produced particle in the proton-nucleon center of mass and $E^*_{max}=(p^{*2}_{max}+m^2)^{1/2}$ is the maximum possible center of mass energy, without changing χ^2.

B. Fits To The K^0_S Extrapolated Cross Section

The function in Equation (V.1) gave a good fit to the K^0_S extrapolated data with $b_1=2.89\pm0.10$, $b_2=-0.98\pm0.11$, $b_3=4.39\pm0.055$, $b_4=-1.65\pm0.088$ and $\chi^2/DF = 1.09$ with 251 data points. The K^0_S extrapolated data can also be fit by a function of the form:

$$Ed^3\sigma/d\vec{p}^3=d_1\exp(d_2x^2+d_3x+d_4p_T)$$

with $d_1=2.02\pm0.22$, $d_2=-5.27\pm0.64$, $d_3=-2.75\pm0.54$, $d_4=-3.07\pm0.04$ with $\chi^2/DF = 1.28$.

C. Fits To The $\bar{\Lambda}^0$ Extrapolated Cross Section

The function of Equation (V.1) with b_2 fixed and set equal to zero can be used to fit the $\bar{\Lambda}^0$ data with parameter values b_1=6.82±1.2, b_3=9.82±0.36, b_4=-2.19±0.11, and χ^2/DF = 0.83 with 93 data points. The simple exponential function:

$$Ed^3\sigma/d\vec{p}^3=d_1\exp(d_2x+d_3p_T^2)$$

also gives a good fit to the $\bar{\Lambda}^0$ data with d_1=1.38±0.19, d_2=-12.2±0.51, d_3=-2.45±0.13 with χ^2/DF = 0.92.

Figures 30(a), 31(a), and 32(a) show the extrapolated cross sections for Λ^0, K_S^0, and $\bar{\Lambda}^0$ with the results of the fits to the function of Equation (V.1).

D. Fits To The Triple Regge Model

The comparison of this data to the triple Regge Model was initiated by T. Devlin.[57] It has been shown by A. H. Mueller[34] that the cross section for the inclusive process a+b→c+anything can be related to the connected part of the forward amplitude for the process $a+b+\bar{c}\rightarrow a+b+\bar{c}$. This relationship is a generalization of the well known optical theorem which relates the imaginary part of the forward elastic scattering amplitude to the total cross section. If one assumes that the amplitude for the inclusive process is dominated by the same Regge singularities as the physical three-body amplitude, it can be shown in the limit t fixed, s/M_x^2 large, and M_x^2 large, where $M_x^2 = (p_a+p_b-p_c)^2$ and p_a,

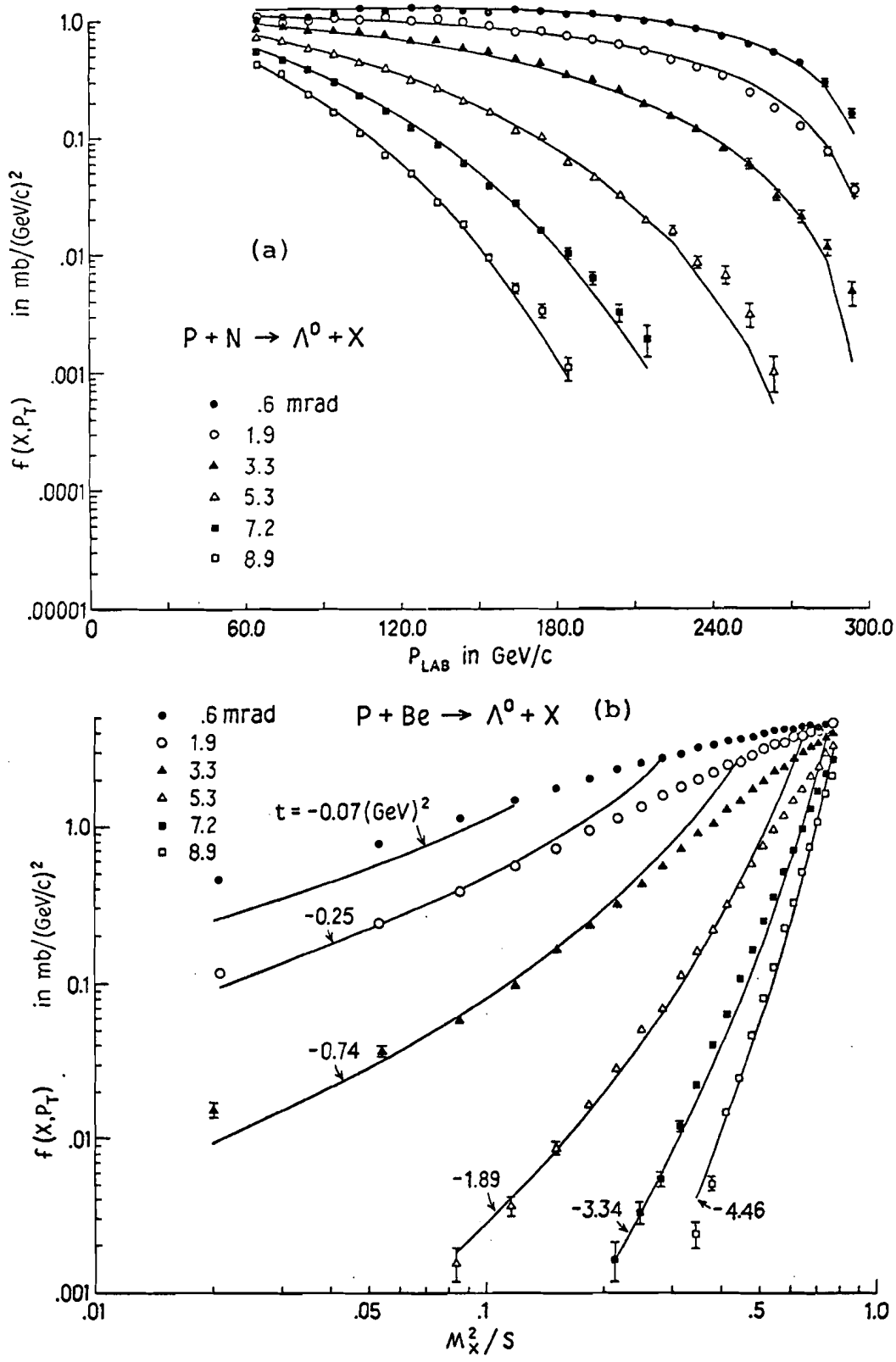

Fig. 30. Invariant cross section for Λ^0 production (a) extrapolated to A=1 and (b) for Be. The lines are results of the fits described in the text.

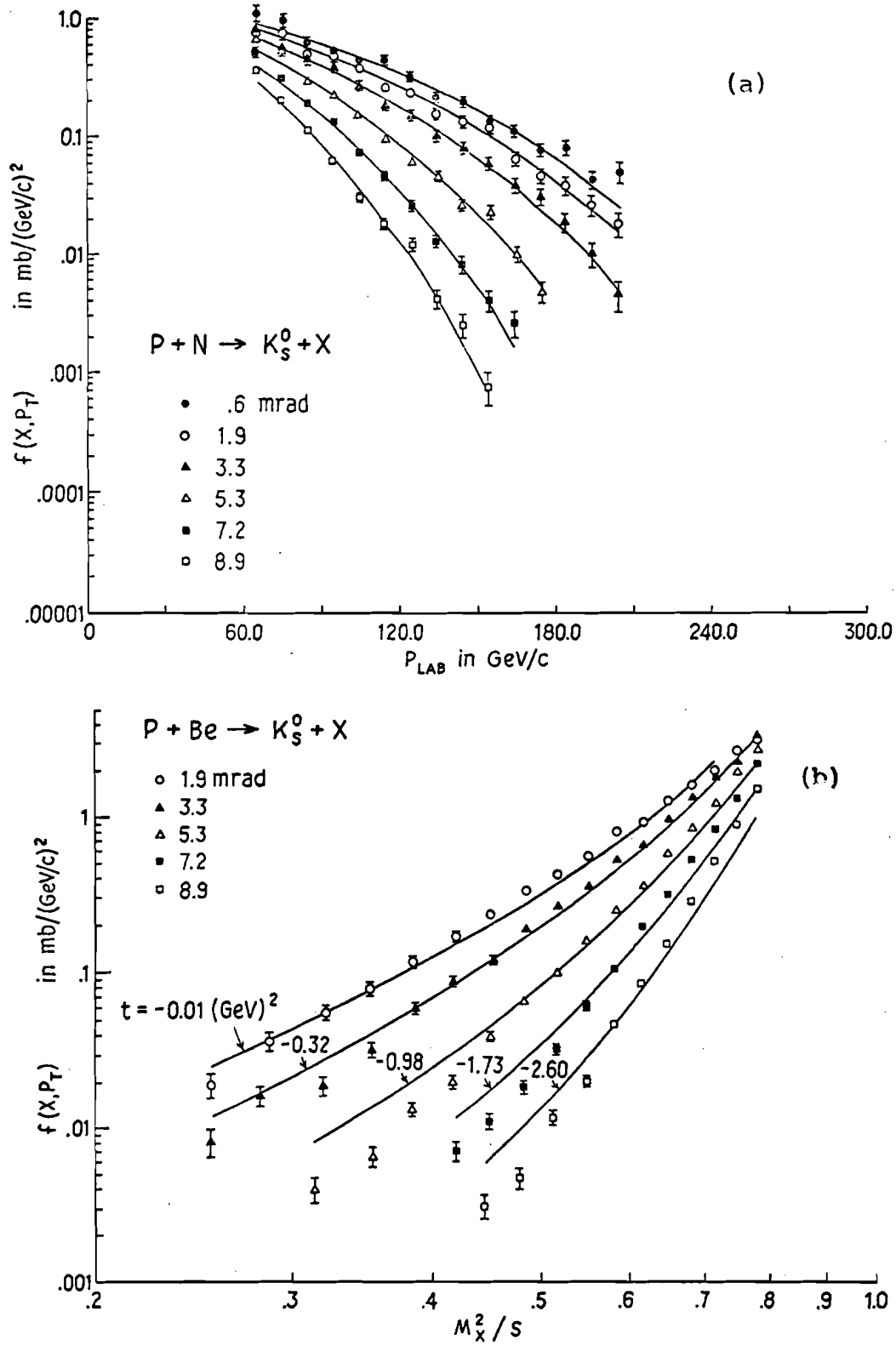

Fig. 31. Invariant cross section for K^0_S production (a) extrapolated to A=1 and (b) for Be. The lines are results of the fits described in the text.

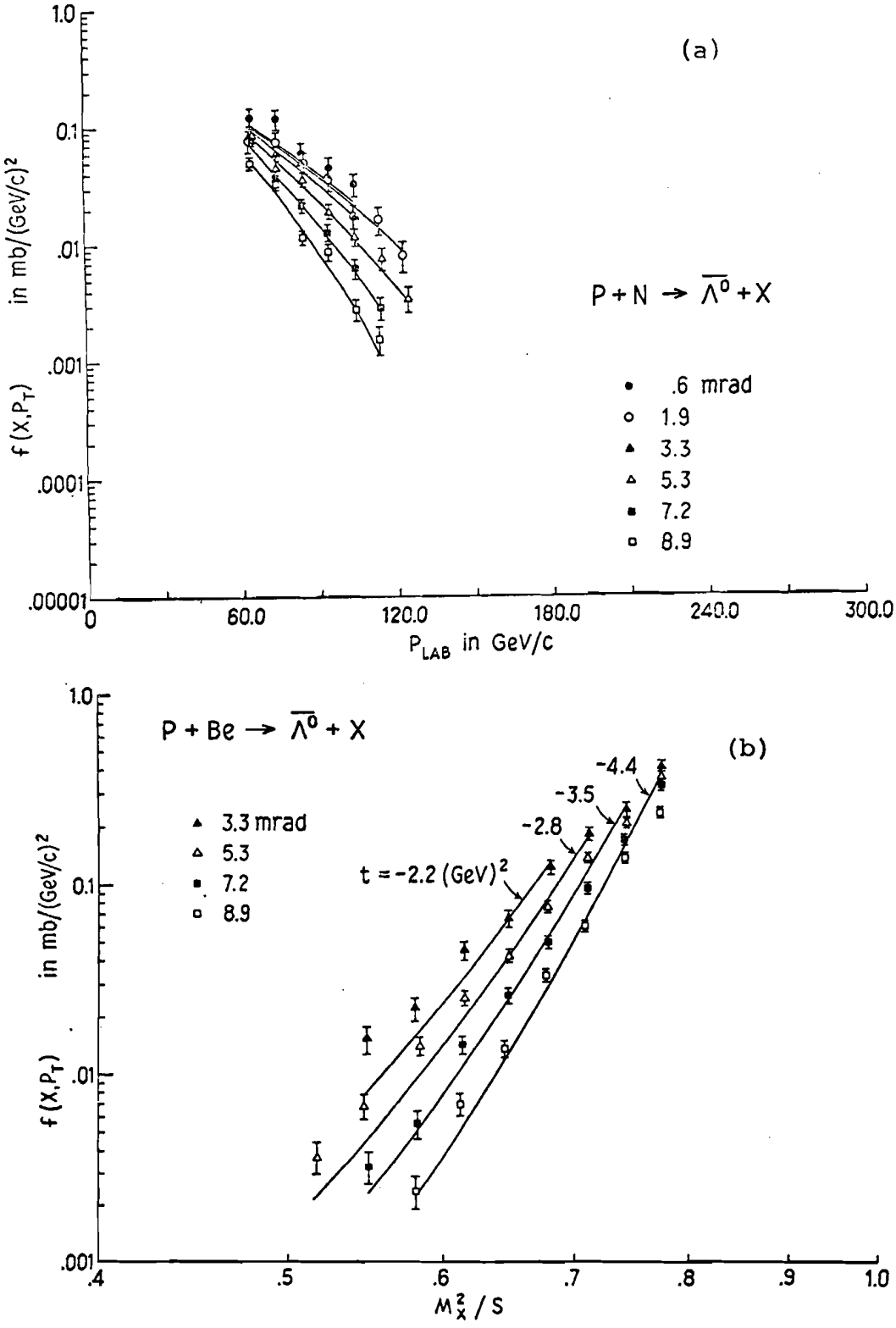

Fig. 32. Invariant cross section for $\bar{\Lambda}^0$ production (a) extrapolated to A=1 and (b) for Be. The lines are results of the fits described in the text.

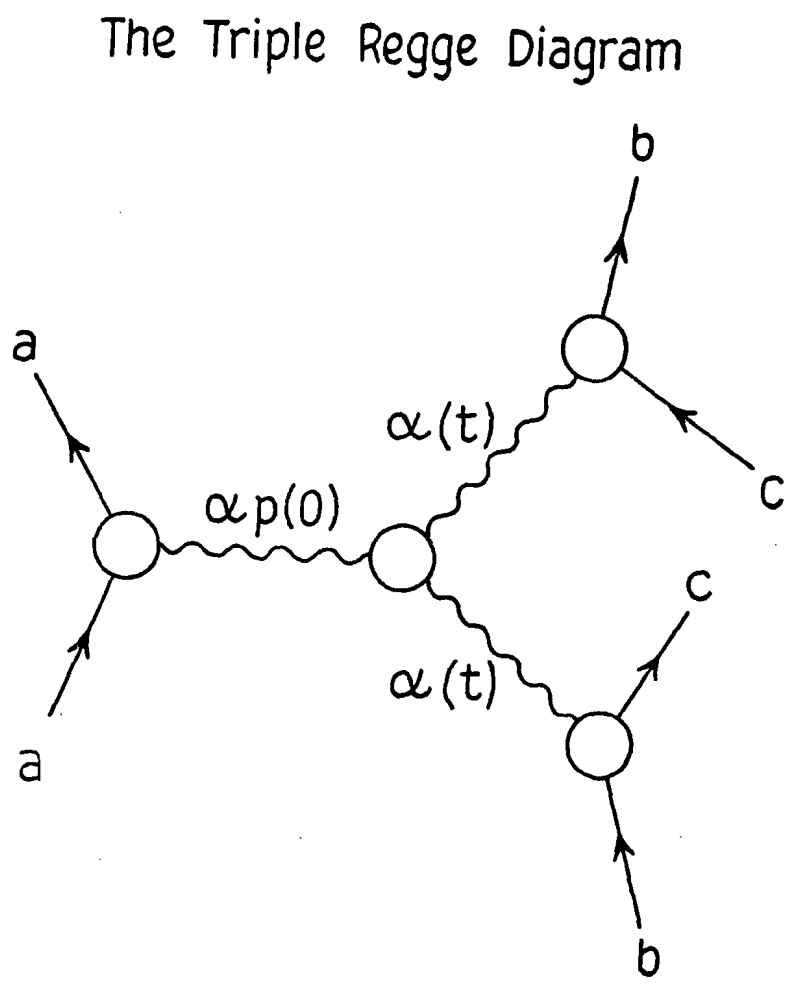

Fig. 33. The triple Regge Diagram.

p_b, and p_c are the 4- momenta of particles a, b, and c respectively, that the inclusive process is described by the triple Regge diagram shown in Figure 33.[39] The cross section for this diagram can be written:[39]

$$Ed^3\sigma/d\vec{p}^3=\beta(t)(s/M_x^2)^{2\alpha(t)-\alpha_p(0)} \qquad (V.2)$$

where $\alpha(t)$ is the leading Regge trajectory which couples to the system $(b\bar{c})$ and $\alpha_p(0)$ is the leading Regge singularity which couples to $(a\bar{a})$. If we assume the pomeron intercept is one, $\alpha_p(0)=1$. and since $M_x^2/s\approx(1-x)$ for large s and small p_T, Equation (V.2) becomes:

$$Ed^3\sigma/d\vec{p}^3=\beta(t)(1-x)^{1-2\alpha(t)}. \qquad (V.3)$$

Bubble chamber experiments[50-53] indicate that the cross sections for Λ^0 and K_s^0 production are independent of energy above 100 GeV so the triple Regge limit is expected to apply at FNAL energies. The region of x regarded as appropriate for the triple Regge limit for production by 300 GeV incident particles is $0.8<x<0.98$.[57] If this restriction is applied literally to the data of this experiment, much of the Λ^0 data and all of the K_s^0 and $\bar{\Lambda}^0$ data are outside the triple Regge limit. Figure 34 shows the relationship between t and x for constant contours in laboratory production angle for the Λ^0 Be data. t is approximately constant for $x>0.5$ for $\theta<7.2$ mr however t varies rapidly for

Table 3. Regge parameters obtained in fits to the Λ^0 cross sections.

$\bar{\theta}$ (mrad)	$\bar{t}$ $(GeV)^2$	α_i	β_i	χ^2	Data Points
"Nucleon"					
0.6	-0.07	0.15±0.03	2.4±0.3	1.8	10
1.9	-0.24	-0.10±0.04	2.4±0.4	3.6	10
3.3	-0.74	-0.46±0.04	2.1±0.2	16.	16
5.3	-1.89	-1.20±0.06	1.6±0.2	13.	17
Be					
0.6	-0.07	0.13±0.01	7.3±0.4	3.1	10
1.9	-0.25	-0.04±0.02	5.7±0.4	5.6	10
3.3	-0.74	-0.42±0.02	5.4±0.3	36.	16
5.3	-1.89	-1.24±0.03	6.2±0.4	14.	20
Pb					
0.6	-0.07	0.09±0.02	36. ±3.	5.7	10
1.9	-0.23	0.03±0.03	20. ±2.	8.6	10
3.3	-0.74	-0.39±0.03	21. ±2.	30.	16
5.3	-1.89	-1.45±0.06	57. ±8.	14.	17

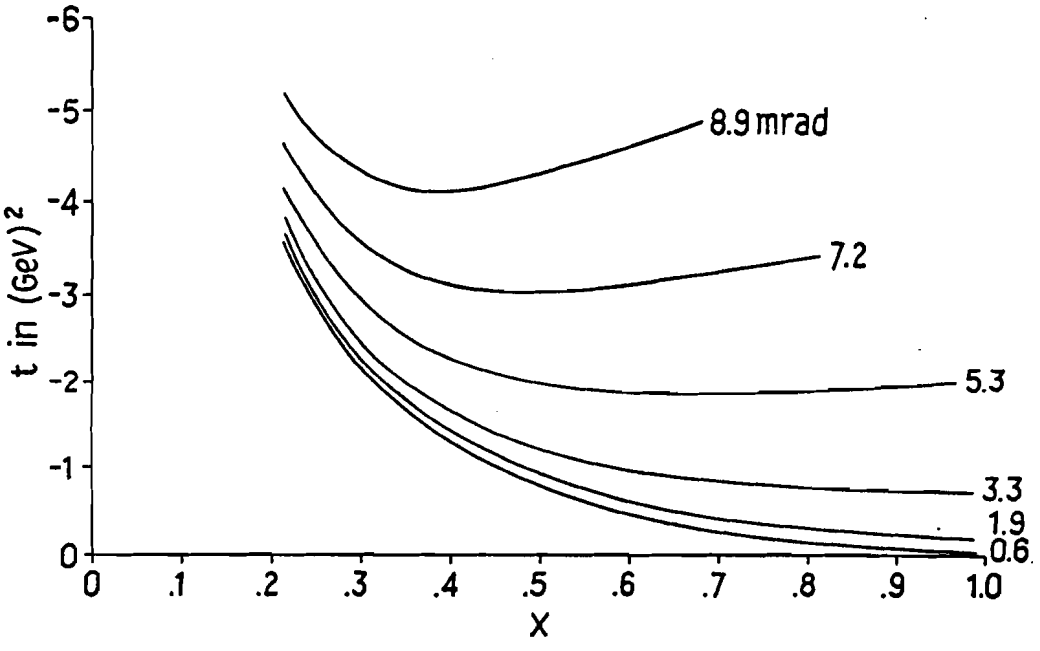

Fig. 34. t versus x at constant production angle for Λ^0 production from Be.

$x<0.5$. The empirical fits which were described in Chapter III can be used to exhibit the behavior of the invariant cross section as a function of t and M_x^2/s. The invariant cross sections for the Be data are plotted versus M_x^2/s in Figures 30(b), 31(b), and 32(b) for Λ^0, K_S^0, and $\bar{\Lambda}^0$ where the solid lines show the behavior of the empircal fits for constant t contours. The constant t values were chosen to be the average values of t for each angle except for angles less than 7.2 mr for Λ^0 for which the averages were taken over the following limited x regions: $x>0.8$ for 0.6 and 1.9 mr, $x>0.7$ for 3.3 mr, and $x>0.6$ for 5.3 mr. It can be seen from Figures 30-32 that the power of M_x^2/s predicted by Equation (V.2) is constant over a wider region of M_x^2/s for constant production angle than for constant t. The data are consistent with the behavior of Equation (V.2) only near the kinematic limit $x=1$. Similar behavior occurs for the Pb and extrapolated cross sections. Information about the Regge trajectory $\alpha(t)$ can be obtained by performing fits to data in the high x region near $x=1$ where Equation (V.2) is obeyed and where t is approximately constant.

The Be, Pb, and extrapolated Λ^0 cross sections were separately fit to the function:

$$Ed^3\sigma/d\vec{p}^3=\beta_i(1-x)^{1-2\alpha_i} \qquad (V.5)$$

where α_i and β_i were determined separately for each of the angles 0.6, 1.9, 3.3, and 5.3. The fits were performed to

the data in 5 GeV/c momentum bins and in the following x regions: $0.97>x>0.8$ for 0.6 and 1.9 mr, $0.97>x>0.7$ for 3.3 mr, and $0.97>x>0.6$ for 5.3 mr. The 3.3 mr points with laboratory momentum greater than 290 GeV/c are not consistent with a constant power of (1-x) for constant t. These points are sensitive to the high momentum background and deviate from the $(1-x)^{a(0)}$ behavior which is observed for all other angles. Therefore all points with x>.97 were eliminated from the fits so that χ^2 would reflect the quality of the fits over the region of x where Equation (V.2) is obeyed. The parameter values obtained in the fits are given in Table 3. The α_i parameters are only very weakly dependent on production target. The values of α_i for the fits to the extrapolated cross sections are plotted versus t in Figure 35.

Since the $(p\bar{\Lambda})$ system has strangeness +1 and baryon number 0, Regge trajectories which couple in Figure 33 must have these properties. Well established resonances with these properties are the $K^*(892)$, $K^{**}(1420)$, and K(498). The K^* and K^{**} define the nearly-degenerate leading Regge trajectories which are expected to dominate Λ^0 production in the triple Regge limit. These resonances are plotted in Figure 35 where $\alpha(m^2)=j$ and j is the spin and m is the mass of the resonance. The Λ^0 α_i values for t>-2 lie close to the straight line defined by the K^* and K^{**} resonances in good agreement with the theory.

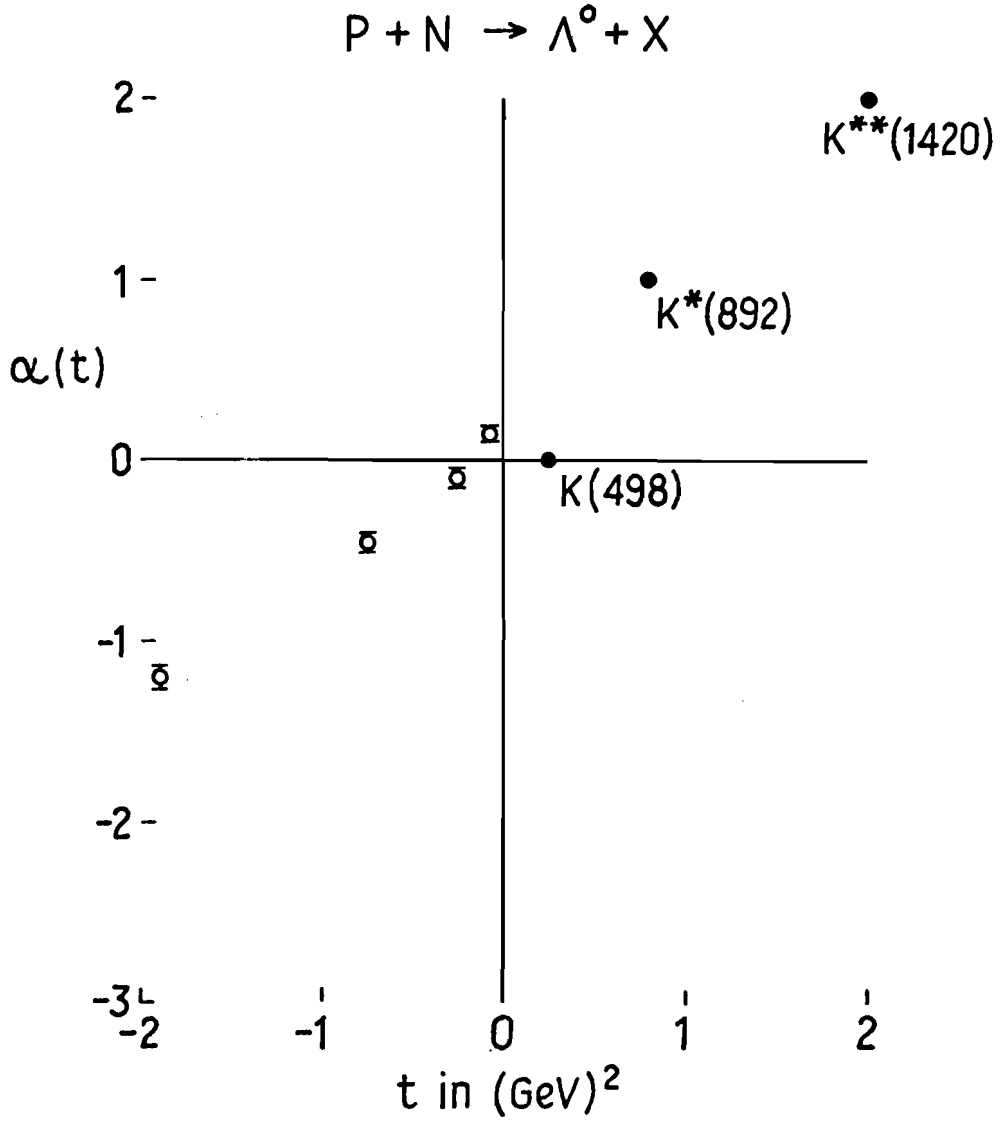

Fig. 35. α_i parameters for fits to the invariant cross section extrapolated to A=1.

Similar fits to the triple Regge Model were performed for the reaction $pp \rightarrow \Lambda^0 + X$ at 19 GeV/c[58] and the data were found to be consistent with Equation (V.2). However the $\alpha(t)$ found at the lower energy, while linear, had a steeper slope and lower intercept than that found here, and favored the K(498) trajectory. This difference could be due to possible energy dependence in the x distribution, or the application in Reference 58 of the triple Regge formula to values of M_x^2/s outside the triple Regge limit.

It is interesting that the exponent of (1-x) at fixed θ is constant over a wider region of x than the exponent of (1-x) at fixed t. It was demonstrated from the empirical fits that the exponent of (1-x) at fixed t is only constant for large x where the triple Regge Model is expected to be valid. In this region the data are consistent with the model. The behavior predicted by Equation (V.3) is remarkably similar to that found empirically and the trajectory determined by the fits is consistent with the existence of known resonances which couple in the triple Regge diagram.

CHAPTER VI

CONCLUSIONS

A host of theoretical models dealing with inclusive production have been discussed in the literature and some models have been useful in categorizing experimental results. For example the Mueller-Regge Model can be used to derive formulas which express the energy dependence of particle distributions in the fragmentation and pionization regions as well as the energy dependence of particle multiplicities. Many models predict asymptotic behavior as the energy becomes large and this appears to be experimentally verified, particularly in the fragmentation region. However many questions remain to be answered and much more theoretical and experimental work must be done. The conclusions derived from this experiment can be summarized as follows:

1) The dependence of the Λ^0 and K^0_S invariant cross sections with the target can be expressed as a power law of the form:

$$\sigma(x,p_T,A)=\sigma(x,p_T,1)A^{\alpha(x,p_T)}$$

where A is the atomic mass number of the target nucleus and the power α is a function of both x and p_T. The variation of α with p_T is consistent with the idea that the particle

interactions become more point-like as p_T increases. Target dependence appears in the cross sections at low p_T at a rapidity 5 units from the target, well into the projectile fragmentation region. The differential multiplicity is increasingly depleted at large y as A increases.

2) Λ^0 production is dominated by projectile fragmentation while K_S^0 and $\bar{\Lambda}^0$ production occurs mainly in the central region. The Λ^0 rapidity distribution exhibits a plateau at the lowest accessible values of rapidity while the K_S^0 and $\bar{\Lambda}^0$ distributions are continuously increasing as y decreases.

3) Production cross sections for strange particles are suppressed by about a factor of ten relative to non-strange particle production cross sections.

4) The p_T distributions for Λ^0, K_S^0, and $\bar{\Lambda}^0$ are similar and the particle ratios do not depend strongly on p_T and target. They appear to depend only on x. If the particle ratios are extrapolated to low x the data are consistent with more copious production of K_S^0 than Λ^0 and nearly equal production of Λ^0 and $\bar{\Lambda}^0$ near x=0.

5) The extrapolated cross sections can be described by a simple empirical function which is similar in form to that predicted by the triple Regge Model. In the region of phase space where the model is expected to be valid, it is consistent with the data.

6) Λ^0 polarization is observed in the inclusive reaction $p+Be \rightarrow \Lambda^0+X$ at an incident proton energy of 300 GeV.

This polarization can be interpreted by the triple Regge Model as arising from absorptive corrections to the triple Regge diagram. However, specific calculations using this assumption do not completely reproduce the data.[59]

The results of this experiment were found to be in general agreement with previous inclusive production experiments whenever a clear comparison could be made. A continuation of this experiment is justified by the results and the obvious next step is to repeat the experiment with a hydrogen target. Such an experiment would measure the Λ^0 polarization from a proton target and test the nucleon extrapolation performed here. Neutral strange particle production data from nuclear targets with incident p, $\bar{p}$, and $\pi^{\pm}$ at energies varing from 100 to 400 GeV has already been obtained with this apparatus at FNAL and will be presented soon. Preliminary results indicate that the Λ^0 distributions for production from 200, 300, and 400 GeV/c protons on Be at 0.6 mr are the same, thus supporting the bubble chamber results that scaling has occurred at FNAL energies.

The usefulness and experimental feasibility of the neutral hyperon beam has been reinforced by this experiment and a rich experimental program has been initiated. Experiments which will be performed or are presently in the process of analysis include the measurement of the Λ^0p total cross section at 300 and 400 GeV; measurement of the Λ^0p

elastic differential cross section; measurement of the Ξ^0 production cross section and inclusive Ξ^0 polarization; and measurement of the asymmetry parameter α_{Ξ^0} in the decay $\Xi^0 \rightarrow \Lambda^0 + \pi^0$. The inclusive Λ^0 polarization will be used to measure the Λ^0 magnetic moment and could be used for future polarized beam experiments. The neutral hyperon beam will continue to be a powerful experimental tool.

APPENDIX A

CALCULATION OF PRODUCTION ANGLE

Figure 36 shows the geometry involved where MØ and M1 are dipole bending magnets which deflect the incident proton beam onto the hyperon production target T. From the known current in M1 and the field integral measurements made in Reference 41 the bend angle α could be calculated for each nominal production angle setting. Then from the measured distances e and d (111±3 m and 5.47±Ø.Ø13 m respectively) it is easy to calculate the angle (γ) the incident proton beam makes with respect to the coordinate system defined by the proton beam with M1 and MØ off from the formula:

$$\gamma=\alpha/(1+d/e).$$

γ was calculated for each nominal setting of M1. The error in the calculation of γ was estimated to be less than ±Ø.1 mr.

The momentum components of each reconstructed neutral strange particle in the chamber coordinate system (defined by the proton beam with M1 and MØ off) were used with the calculated values of γ for each nominal M1 setting to obtain the angle (θ) the reconstructed particle made with respect to the incident proton beam. In the chamber coordinate

system the z axis points downstream along the direction of the nominal 0 mr proton beam, the y axis points upwards, and the x axis points to the left. For the sake of clarity let us define a new (primed) coordinate system obtained by performing a rotation about the x axis by angle γ so the z' axis points in the direction of the incident proton beam for a non-zero setting of M1. Then the momentum components of a reconstructed particle in the primed coordinate system will be related to the components in the chamber coordinate system as follows:

$$p_{z'}=p_z\cos\gamma-p_y\sin\gamma \quad (A.1)$$
$$p_{y'}=p_y\cos\gamma+p_z\sin\gamma$$
$$p_{x'}=p_x.$$

The angle θ is then given by:

$$\theta=\arccos(p_{z'}/p) \quad (A.2)$$

where $p^2=p_{x'}^2+p_{y'}^2+p_{z'}^2$. Equations (A.1) and (A.2) were used to calculate the production angle θ for each event.

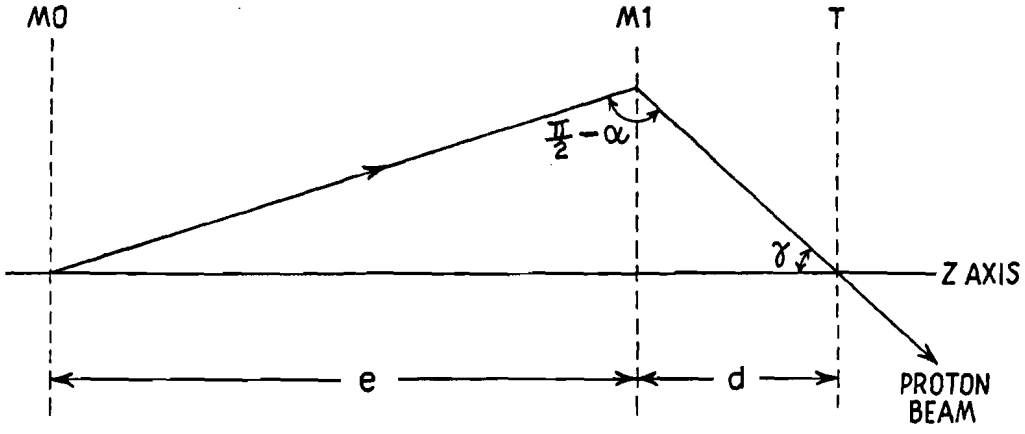

Fig. 36. The geometry used in calculation of the laboratory production angle.

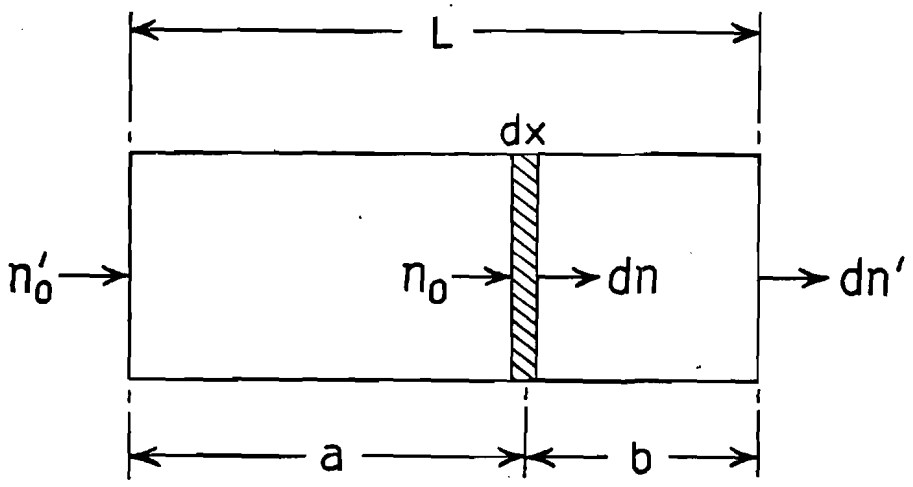

Fig. 37. Particle production from a differential target element.

APPENDIX B

THE TARGET ABSORPTION CORRECTION

The number of particles (dn) produced in the collision of n_o incident particles with a differential element of target of length dx is given by:

$$dn/n_o=(N_o\sigma/A)dx \quad (B.1)$$

where N_o=Avogadro's number, A is the atomic mass number of the target nucleus, and σ is the production cross section for the process. (See Figure 37.) The quantities which are measured are the number of produced particles leaving the target (dn') and the number (n_o') of incident particles which enter the target. The measured numbers are given in terms of the numbers in Equation (B.1) by:

$$n_o'=n_o\exp(a/l_o) \quad (B.2a)$$
$$dn'=dn\exp(-b/l) \quad (B.2b)$$

where l_o and l are the absorption lengths of the incident and produced particles respectively, and a and b are the distances defined in Figure 37. Substituting Equations (B.2) into Equation (B.1) and integrating over the length of the target (L) one obtains:

$$\sigma=(n'A/n_o'N_o)[k\exp(-L/l_o)(1-\exp(-L/k))]^{-1} \quad (B.3)$$

where $k=l_o l/(l_o-l)$. The cross section (σ') which is calculated directly from the measured numbers is given by:

$$\sigma'=n'A/n_o'N_o.$$

Therefore the corrected cross section (σ) is given by:

$$\sigma=c\sigma'$$

where

$$c=L[k\exp(-L/l_o)(1-\exp(-L/k))]^{-1}. \quad (B.4)$$

It follows from Equation (B.3) that the measured ratio (R) of the produced particle yield with the 1/2 interaction length target to the yield with the 1/4 interaction length target is given by:

$$R=\exp(-L/2l_o)(1+\exp(-L/2k)). \quad (B.5)$$

Using Equations (B.4) and (B.5) we can eliminate k and solve for c in terms of R:

$$c=[R(R-2\exp(-L/2l_o))][2\ln(R\exp(L/2l_o)-1)]^{-1}. \quad (B.6)$$

If all interactions result in the loss of the incident particle as far as particle production is concerned, $L/l_o=0.5$. However, if some interaction products produce the

observed particle, $L/l_o < 0.5$. If numbers are put into Equation (B.6), one finds that c varies less than 1% as L/l_o varies between 0 and 0.5. Therefore, we henceforth set $L/l_o = 0$ or $l_o = \infty$ and obtain the following correction for Be:

$$c = [2\ln(R-1)][R(R-2)]^{-1}. \quad (B.7)$$

To use the ratio from Be to correct the cross section for another target we use Equation (B.4) to obtain:

$$c_i = (L_i/l_i)[1-\exp(-L_i/l_i)]^{-1} \quad (B.8)$$

where L_i and l_i are the length and absorption length for target i. Assuming $l_i = \alpha l$ where α is the ratio of the proton absorption length for target i to the proton absorption length for Be we obtain:

$$c_i = (L/\alpha l)[1-\exp(-L_i/\alpha l)]^{-1}. \quad (B.9)$$

Using Equations (B.5) and (B.9) to eliminate l we obtain:

$$c_i = (2L_i/\alpha L)\ln(R-1)[(R-1)^{2L_i/\alpha L} - 1]^{-1}. \quad (B.10)$$

Equation (B10) was used to obtain the correction for the Cu and Pb targets.

APPENDIX C

DATA TABLES

The average production angle (θ) in milliradians, average laboratory momentum (p) in GeV/c, and invariant cross section ($\sigma \equiv Ed^3\sigma/d\vec{p}^3 \pm \Delta\sigma$) in mb/(GeV/c)^2 for Λ^0, K_S^0, and $\bar{\Lambda}^0$ and for the Be, Cu, and Pb targets are given in Tables 4-12. Each 10 GeV/c momentum bin has at least 20 events. The overall correction factor, $C(p,\theta)$, which was defined in Section III.B is also given for each bin. The errors ($\Delta\sigma$) in σ include statistical errors as well as the estimated error in $C(p,\theta)$. The overall normalization error was estimated to be 20% FWHM.

Table 4. Data for Λ^0 production from beryllium.

θ	p	σ	Δσ	C(p,θ)
.7	65.3	4.40	.21	1.25
.7	74.9	4.40	.18	1.26
.7	84.8	4.22	.16	1.27
.6	94.8	4.39	.16	1.29
.6	104.9	4.315	.099	1.28
.6	114.8	4.158	.092	1.28
.6	124.8	4.162	.090	1.27
.6	134.8	4.091	.088	1.27
.6	144.9	3.893	.083	1.27
.6	154.8	3.705	.079	1.27
.6	164.8	3.604	.073	1.27
.6	174.9	3.510	.069	1.27
.6	184.7	3.317	.067	1.27
.6	194.8	3.176	.065	1.27
.6	204.9	2.881	.061	1.27
.6	214.8	2.724	.056	1.27
.6	224.8	2.549	.057	1.27
.6	234.8	2.321	.053	1.28
.6	244.7	2.020	.048	1.28
.6	254.7	1.758	.044	1.28
.6	264.7	1.471	.039	1.29
.6	274.6	1.131	.033	1.29
.6	284.5	.771	.026	1.29
.6	294.3	.451	.019	1.29
.8	65.5	4.66	.35	1.25
.8	74.8	4.75	.29	1.26
.8	85.0	4.44	.24	1.27
.8	94.6	4.36	.22	1.29
.8	104.8	4.48	.16	1.28
.8	114.8	4.39	.15	1.28
.8	124.8	4.22	.14	1.27
.8	134.7	4.04	.13	1.27
.8	144.9	4.07	.12	1.27
.8	154.8	3.65	.11	1.27
.8	164.9	3.71	.11	1.27
.7	174.8	3.47	.10	1.27
.7	184.7	3.39	.10	1.27
.8	194.8	3.075	.092	1.27
.7	204.8	2.754	.086	1.27
.7	214.7	2.725	.083	1.27
.7	224.8	2.391	.078	1.27
.7	234.7	2.320	.077	1.28
.7	244.6	2.017	.071	1.28
.7	254.8	1.689	.063	1.28
.7	264.6	1.462	.058	1.29
.7	274.6	.970	.046	1.29
.7	284.7	.675	.038	1.29
.7	294.1	.342	.026	1.29
1.4	65.3	4.60	.19	1.37
1.3	75.0	4.57	.15	1.34
1.3	84.8	4.21	.12	1.32
1.3	94.9	4.33	.11	1.31
1.3	104.9	4.37	.10	1.30
1.3	114.8	4.137	.096	1.29
1.3	124.8	4.059	.092	1.28
1.3	134.7	3.728	.085	1.28
1.3	144.7	3.617	.081	1.27
1.3	154.8	3.459	.077	1.27
1.3	164.8	3.332	.071	1.27
1.3	174.8	3.080	.064	1.26
1.3	184.8	2.891	.062	1.26
1.3	194.7	2.717	.059	1.26
1.3	204.8	2.474	.055	1.26
1.3	214.8	2.259	.049	1.26
1.2	224.8	1.956	.047	1.26
1.2	234.7	1.789	.045	1.26
1.2	244.6	1.599	.041	1.26
1.2	254.6	1.295	.035	1.26
1.2	264.9	1.044	.031	1.26
1.2	274.7	.772	.025	1.26
1.1	284.4	.510	.020	1.26
1.1	294.3	.288	.015	1.26
1.6	65.1	4.63	.17	1.36
1.6	74.9	4.42	.14	1.30
1.6	84.8	4.06	.11	1.29
1.6	94.8	4.10	.11	1.28
1.5	104.8	3.96	.10	1.28
1.5	114.8	3.905	.096	1.28
1.5	124.8	3.757	.091	1.28
1.5	134.9	3.581	.077	1.28
1.5	144.8	3.411	.073	1.27
1.5	154.8	3.253	.069	1.27
1.5	164.9	3.085	.063	1.27
1.5	174.8	2.859	.057	1.27
1.5	184.8	2.712	.055	1.27
1.5	194.9	2.486	.052	1.26
1.4	204.8	2.172	.047	1.26
1.4	214.7	1.997	.042	1.26
1.4	224.8	1.798	.041	1.27
1.4	234.8	1.552	.037	1.27
1.4	244.7	1.345	.034	1.27
1.4	254.8	1.106	.029	1.27
1.4	264.7	.878	.025	1.27
1.4	274.5	.607	.019	1.27
1.3	284.5	.417	.016	1.27
1.3	294.4	.223	.011	1.27
2.0	65.1	4.55	.17	1.37
2.0	74.9	4.13	.13	1.34
2.0	84.8	4.01	.10	1.32
2.0	94.9	3.962	.098	1.31
2.0	104.9	3.768	.089	1.30
2.0	114.7	3.694	.084	1.29
2.0	124.8	3.417	.076	1.28
2.0	134.9	3.327	.074	1.28
2.0	144.7	3.126	.069	1.27
2.0	154.8	2.825	.063	1.27
2.0	164.7	2.555	.055	1.27
2.0	174.8	2.472	.052	1.26
1.9	184.8	2.211	.047	1.26
1.9	194.7	1.987	.044	1.26
1.9	204.8	1.783	.041	1.26
1.9	214.7	1.557	.035	1.26
1.9	224.7	1.324	.033	1.26
1.9	234.7	1.115	.029	1.26
1.8	244.8	.937	.026	1.26
1.8	254.7	.713	.021	1.26
1.8	264.6	.552	.018	1.26
1.8	274.5	.379	.014	1.26
1.8	284.4	.239	.011	1.26
1.7	294.1	.1166	.0073	1.26
3.4	65.0	3.85	.12	1.32
3.3	74.9	3.665	.091	1.35
3.3	84.9	3.345	.071	1.32
3.3	94.9	3.169	.065	1.31
3.3	104.8	2.946	.058	1.30
3.3	114.7	2.702	.052	1.29
3.3	124.8	2.383	.045	1.29
3.3	134.8	2.246	.043	1.28
3.3	144.8	1.936	.037	1.28
3.3	154.7	1.718	.038	1.28
3.3	164.8	1.443	.028	1.27
3.2	174.7	1.264	.024	1.27
3.2	184.7	1.027	.021	1.27

Table 4. (continued)

θ	p	σ	Δσ	C(p,θ)
3.2	194.6	.890	.019	1.26
3.2	204.6	.710	.016	1.26
3.2	214.7	.547	.013	1.26
3.1	224.6	.420	.012	1.25
3.1	234.5	.3133	.0095	1.25
3.1	244.4	.2290	.0078	1.25
3.1	254.4	.1618	.0063	1.24
3.1	264.4	.0966	.0047	1.23
3.0	274.4	.0575	.0035	1.22
3.0	283.9	.0363	.0028	1.21
3.1	294.1	.0152	.0017	1.21
3.9	65.2	3.57	.20	1.32
3.9	74.9	3.58	.15	1.36
3.8	84.8	3.02	.11	1.32
3.9	94.8	2.888	.097	1.31
3.9	104.8	2.742	.084	1.31
3.8	114.8	2.469	.073	1.30
3.8	124.7	2.176	.064	1.29
3.8	134.7	1.812	.055	1.29
3.8	144.7	1.565	.048	1.29
3.8	154.8	1.335	.045	1.29
3.8	164.7	1.120	.037	1.28
3.7	174.7	.887	.031	1.27
3.7	184.7	.721	.027	1.27
3.7	194.5	.532	.022	1.26
3.7	204.7	.465	.021	1.26
3.7	214.6	.301	.016	1.25
3.7	224.7	.258	.015	1.25
3.7	234.7	.162	.011	1.24
3.6	244.8	.1200	.0096	1.23
3.5	254.4	.0639	.0068	1.21
3.5	264.1	.0534	.0062	1.21
3.6	273.6	.0188	.0035	1.14
5.4	65.0	3.222	.074	1.37
5.3	74.8	2.907	.056	1.40
5.3	84.8	2.405	.042	1.36
5.3	94.7	2.086	.038	1.35
5.3	104.7	1.728	.030	1.34
5.3	114.6	1.451	.026	1.33
5.3	124.7	1.160	.021	1.33
5.3	134.7	.941	.017	1.32
5.2	144.6	.740	.014	1.32
5.2	154.6	.571	.013	1.32
5.2	164.6	.4153	.0085	1.31
5.2	174.6	.3150	.0067	1.30
5.2	184.6	.2170	.0052	1.29
5.2	194.6	.1571	.0042	1.28
5.1	204.5	.1104	.0034	1.26
5.1	214.5	.0687	.0025	1.24
5.1	224.4	.0503	.0021	1.22
5.1	234.5	.0282	.0015	1.17
5.1	244.4	.0164	.0011	1.10
5.0	254.2	.00865	.00079	1.00
5.0	264.6	.00362	.00052	.82
4.9	274.3	.00154	.00038	.63
7.2	64.9	2.670	.063	1.38
7.2	74.8	2.178	.044	1.40
7.2	84.7	1.674	.031	1.36
7.2	94.6	1.284	.025	1.35
7.2	104.6	.953	.019	1.34
7.2	114.6	.697	.014	1.33
7.1	124.7	.503	.011	1.32
7.1	134.5	.3473	.0080	1.32
7.1	144.6	.2429	.0061	1.33
7.1	154.5	.1606	.0048	1.33
7.1	164.5	.1060	.0033	1.28
7.1	174.5	.0625	.0023	1.25
7.1	184.5	.0400	.0018	1.21
7.0	194.5	.0220	.0013	1.13
7.0	204.5	.01190	.00092	1.02
6.9	214.4	.00547	.00065	.83
7.0	224.3	.00327	.00054	.70
6.9	234.5	.00164	.00046	.51
9.0	64.8	2.098	.047	1.40
8.9	74.7	1.613	.032	1.41
8.9	84.6	1.051	.020	1.36
8.9	94.6	.725	.015	1.34
8.9	104.5	.499	.010	1.33
8.9	114.5	.3163	.0072	1.32
8.9	124.4	.2180	.0053	1.32
8.9	134.4	.1242	.0036	1.32
8.8	144.5	.0792	.0026	1.33
8.8	154.4	.0457	.0019	1.33
8.8	164.3	.0245	.0012	1.18
8.8	174.3	.01455	.00091	1.09
8.8	184.3	.00507	.00057	.83
8.8	194.5	.00235	.00046	.60
8.7	204.9	.00064	.00042	.26

Table 5. Data for K_s^0 production from beryllium.

θ	p	σ	Δσ	C(p,θ)
.6	64.6	3.83	.30	1.25
.6	75.1	3.11	.20	1.25
.6	84.8	2.36	.14	1.25
.6	95.1	1.933	.088	1.26
.7	105.0	1.552	.069	1.25
.7	114.6	1.270	.056	1.24
.7	124.8	.984	.044	1.24
.6	134.6	.740	.035	1.23
.6	144.6	.613	.030	1.23
.6	154.9	.435	.023	1.22
.6	164.5	.358	.020	1.22
.6	174.8	.263	.016	1.22
.6	184.8	.212	.014	1.22
.6	194.5	.139	.011	1.21
.6	204.6	.1099	.0095	1.21
.6	214.6	.0758	.0075	1.21
.6	224.6	.0437	.0056	1.21
.6	235.5	.0237	.0040	1.21
.6	244.3	.0179	.0034	1.21
.6	254.3	.0124	.0028	1.21
.7	65.0	4.87	.61	1.25
.8	75.4	3.05	.34	1.25
.8	85.0	2.57	.25	1.25
.8	94.8	1.91	.18	1.26
.7	104.7	1.50	.13	1.25
.8	114.5	1.063	.095	1.24
.8	124.9	.910	.080	1.24
.7	134.6	.842	.072	1.23
.7	144.3	.492	.051	1.23
.7	154.0	.447	.046	1.22
.7	164.9	.346	.039	1.22
.8	174.5	.273	.033	1.22
.7	184.4	.213	.028	1.22
.7	195.8	.165	.024	1.21
.7	203.6	.113	.020	1.21
.7	213.8	.089	.017	1.21
1.3	65.5	3.57	.30	1.25
1.3	74.9	2.92	.20	1.25
1.3	84.8	2.26	.14	1.25
1.3	94.9	1.68	.10	1.26
1.3	104.8	1.493	.072	1.25
1.3	114.6	1.219	.058	1.24
1.3	124.5	.973	.047	1.24
1.3	134.1	.721	.037	1.23
1.3	144.9	.609	.032	1.23
1.3	154.8	.437	.025	1.22
1.2	164.8	.298	.020	1.22
1.2	174.8	.243	.017	1.22
1.3	184.9	.192	.015	1.22
1.3	194.9	.119	.011	1.21
1.3	204.4	.0644	.0078	1.21
1.2	214.3	.0447	.0063	1.21
1.2	224.5	.0265	.0047	1.21
1.3	233.8	.0289	.0049	1.21
1.2	245.6	.0170	.0037	1.21
1.6	65.3	3.51	.26	1.25
1.6	75.2	2.81	.18	1.25
1.6	85.0	2.45	.14	1.25
1.5	94.9	1.754	.099	1.26
1.5	104.8	1.403	.061	1.25
1.5	114.7	1.087	.048	1.24
1.5	124.7	.820	.037	1.24
1.5	134.9	.709	.032	1.23
1.5	144.4	.479	.024	1.23
1.5	154.5	.395	.021	1.22
1.4	164.3	.304	.017	1.22
1.5	174.4	.250	.015	1.22
1.4	184.9	.147	.011	1.22
1.4	194.2	.1090	.0089	1.21
1.4	204.5	.0779	.0073	1.21
1.4	214.4	.0549	.0059	1.21
1.4	225.4	.0423	.0051	1.21
1.3	234.0	.0208	.0035	1.21
1.3	243.7	.0131	.0027	1.21
2.0	65.3	3.21	.26	1.25
2.0	75.0	2.73	.18	1.25
2.0	85.1	2.04	.13	1.25
2.0	95.0	1.650	.097	1.26
2.0	104.9	1.308	.061	1.25
2.0	114.7	.947	.046	1.24
2.0	124.6	.821	.039	1.24
2.0	134.6	.566	.029	1.23
2.0	144.7	.433	.024	1.23
1.9	154.5	.341	.020	1.22
1.9	164.9	.238	.016	1.22
1.9	174.2	.172	.013	1.22
1.8	184.9	.119	.010	1.22
1.9	194.8	.0800	.0080	1.21
1.8	203.8	.0567	.0065	1.21
1.9	214.4	.0373	.0051	1.21
1.9	224.1	.0196	.0036	1.21
3.3	65.1	3.38	.19	1.33
3.3	74.5	2.32	.11	1.31
3.3	84.7	1.841	.078	1.28
3.4	94.9	1.365	.055	1.27
3.3	104.7	.989	.041	1.26
3.3	114.7	.678	.029	1.25
3.3	124.6	.538	.024	1.25
3.3	134.5	.365	.018	1.24
3.3	144.8	.271	.014	1.24
3.2	154.6	.193	.011	1.24
3.2	164.2	.1215	.0084	1.23
3.3	175.0	.0886	.0068	1.22
3.2	184.3	.0604	.0054	1.22
3.2	194.3	.0328	.0038	1.21
3.2	204.3	.0194	.0028	1.20
3.2	215.8	.0166	.0026	1.21
3.4	224.0	.0082	.0018	1.20
3.8	64.6	3.01	.33	1.34
3.9	74.5	2.23	.20	1.31
3.8	84.6	1.77	.13	1.29
3.8	94.8	1.335	.094	1.28
3.8	104.9	.805	.062	1.27
3.8	114.7	.611	.048	1.26
3.8	124.3	.474	.039	1.25
3.8	135.1	.307	.029	1.25
3.7	144.4	.187	.021	1.24
3.8	154.8	.176	.019	1.24
3.7	163.4	.099	.014	1.23
3.8	173.4	.0495	.0094	1.22
5.4	65.0	2.77	.12	1.37
5.3	74.7	2.005	.071	1.35
5.3	84.8	1.248	.043	1.33
5.3	94.8	.868	.029	1.32
5.3	104.8	.586	.020	1.31
5.3	114.6	.364	.014	1.30
5.3	124.6	.253	.010	1.29
5.3	134.8	.1613	.0072	1.28
5.2	144.6	.1005	.0052	1.28
5.2	154.5	.0672	.0040	1.28
5.3	164.4	.0398	.0028	1.25
5.1	174.5	.0204	.0019	1.24
5.3	184.6	.0133	.0015	1.23

Table 5. (continued)

θ	p	σ	Δσ	C(p,θ)
5.2	193.6	.0065	.0010	1.20
5.2	285.5	.00401	.00075	1.19
7.2	65.0	2.233	.096	1.38
7.2	74.8	1.345	.052	1.36
7.2	84.7	.842	.031	1.33
7.2	94.6	.534	.020	1.32
7.2	104.5	.319	.013	1.31
7.1	114.5	.1983	.0089	1.30
7.2	124.8	.1059	.0057	1.30
7.1	134.4	.0624	.0039	1.29
7.1	144.3	.0329	.0026	1.29
7.0	154.2	.0189	.0019	1.28
7.2	164.2	.0111	.0013	1.22
7.0	173.1	.0071	.0010	1.20
9.0	64.8	1.546	.067	1.38
8.9	74.7	.909	.035	1.36
8.9	84.6	.522	.020	1.33
8.9	94.6	.288	.012	1.32
8.9	104.5	.1541	.0072	1.31
8.9	114.5	.0862	.0046	1.30
8.9	124.4	.0478	.0031	1.30
8.9	133.8	.0207	.0018	1.29
8.7	144.9	.0118	.0013	1.29
8.9	154.9	.00474	.00077	1.29
8.9	164.9	.00313	.00057	1.12

Table 6. Data for $\bar{\Lambda}^0$ production from beryllium.

θ	p	σ	Δσ	C(p,θ)
.7	64.5	.488	.055	1.35
.7	74.3	.393	.038	1.33
.6	84.3	.234	.023	1.31
.6	94.3	.173	.017	1.30
.6	104.9	.116	.012	1.29
.6	114.7	.0705	.0085	1.28
.7	124.6	.0378	.0057	1.27
.6	134.9	.0304	.0049	1.26
.7	143.7	.0241	.0042	1.26
.8	64.3	.56	.12	1.35
.8	74.7	.426	.079	1.33
.8	85.0	.177	.040	1.31
.8	104.4	.138	.027	1.29
1.3	64.9	.517	.062	1.35
1.3	74.8	.343	.038	1.33
1.3	84.7	.205	.023	1.31
1.3	94.8	.127	.016	1.30
1.4	104.8	.106	.013	1.29
1.4	114.6	.0640	.0088	1.28
1.5	125.1	.0366	.0062	1.27
1.3	134.5	.0253	.0049	1.26
1.6	64.4	.510	.053	1.35
1.5	74.2	.304	.031	1.33
1.5	84.5	.203	.020	1.31
1.6	94.1	.145	.014	1.30
1.5	104.0	.0726	.0088	1.29
1.5	114.0	.0666	.0077	1.28
1.6	123.7	.0402	.0055	1.27
1.5	134.3	.0298	.0045	1.26
1.5	144.7	.0151	.0030	1.26
2.1	65.0	.421	.049	1.35
2.0	74.7	.304	.032	1.33
2.0	85.0	.195	.020	1.31
2.0	94.2	.130	.014	1.30
2.0	104.5	.0810	.0098	1.29
1.9	114.7	.0568	.0074	1.28
2.0	124.2	.0347	.0054	1.27
2.0	134.6	.0249	.0043	1.26
3.4	64.9	.414	.039	1.37
3.4	74.7	.250	.023	1.34
3.3	84.7	.185	.016	1.32
3.3	94.2	.124	.011	1.31
3.3	104.5	.0667	.0069	1.30
3.3	114.4	.0452	.0051	1.29
3.4	125.0	.0222	.0033	1.28
3.3	134.8	.0153	.0026	1.28
3.9	64.7	.307	.060	1.37
3.8	74.3	.355	.050	1.35
3.9	84.3	.257	.034	1.33
3.8	94.0	.105	.018	1.32
4.0	104.2	.066	.013	1.30
3.9	114.0	.0465	.0096	1.29
5.4	64.9	.373	.024	1.41
5.3	74.5	.212	.014	1.39
5.3	84.6	.1392	.0088	1.36
5.3	94.7	.0769	.0054	1.35
5.3	104.1	.0426	.0034	1.34
5.3	114.0	.0255	.0024	1.33
5.3	123.7	.0141	.0016	1.33
5.3	135.0	.0068	.0010	1.32
5.4	143.9	.00371	.00073	1.31
7.2	64.7	.335	.021	1.42
7.2	74.8	.173	.011	1.39
7.2	84.4	.0964	.0067	1.37
7.2	94.3	.0501	.0040	1.36
7.2	103.9	.0262	.0025	1.35
7.2	114.2	.0143	.0016	1.34
7.1	123.7	.00552	.00091	1.33
7.0	133.5	.00329	.00067	1.33
9.0	64.6	.240	.015	1.42
8.9	74.3	.1386	.0087	1.40
8.9	84.7	.0610	.0043	1.37
8.9	94.4	.0336	.0027	1.36
8.8	104.2	.0135	.0014	1.35
8.8	114.2	.00696	.00092	1.34
8.9	123.5	.00239	.00050	1.33

Table 7. Data for Λ^0 production from copper.

θ	p	σ	Δσ	C(p,θ)
.7	65.1	17.3	1.2	1.16
.6	74.8	16.79	.97	1.17
.6	84.9	14.72	.76	1.18
.6	94.9	15.35	.73	1.20
.6	104.9	14.68	.52	1.19
.6	114.7	13.17	.45	1.19
.6	124.9	13.36	.43	1.18
.6	134.9	12.19	.39	1.18
.6	144.8	11.81	.37	1.18
.6	154.7	10.31	.33	1.18
.6	164.8	10.14	.31	1.18
.6	174.8	9.80	.29	1.18
.6	184.9	8.67	.27	1.18
.6	194.8	7.78	.25	1.18
.6	204.9	7.76	.25	1.18
.6	214.9	7.07	.22	1.18
.6	224.7	6.58	.22	1.18
.6	234.8	5.98	.21	1.19
.6	244.8	5.15	.19	1.19
.6	254.8	4.67	.18	1.19
.6	264.7	3.53	.15	1.19
.6	274.5	3.00	.14	1.20
.5	284.7	2.02	.11	1.20
.6	294.6	1.225	.088	1.20
.8	64.9	20.1	1.1	1.16
.8	75.0	15.83	.75	1.17
.9	84.8	14.92	.64	1.18
.8	94.8	15.09	.62	1.20
.8	104.8	15.18	.42	1.19
.8	114.7	13.58	.36	1.19
.8	124.8	12.84	.33	1.18
.8	134.7	12.72	.32	1.18
.8	144.8	11.59	.30	1.18
.8	154.9	11.12	.28	1.18
.8	164.9	10.45	.26	1.18
.8	174.9	9.49	.23	1.18
.8	184.9	8.82	.22	1.18
.8	194.9	8.07	.20	1.18
.8	204.7	7.70	.20	1.18
.8	214.8	7.00	.18	1.18
.8	224.7	6.43	.18	1.18
.7	234.8	5.90	.17	1.19
.8	244.9	5.25	.16	1.19
.8	254.8	4.40	.14	1.19
.7	264.6	3.67	.12	1.19
.7	274.7	2.63	.10	1.20
.7	284.8	1.864	.084	1.20
.7	294.4	1.188	.067	1.20
1.3	65.2	20.2	1.1	1.27
1.3	74.8	18.46	.81	1.25
1.2	85.0	15.80	.60	1.23
1.3	94.8	16.33	.55	1.22
1.3	104.7	14.74	.47	1.21
1.3	114.8	14.01	.42	1.20
1.3	124.7	12.64	.37	1.19
1.2	134.8	12.33	.36	1.19
1.2	144.7	11.05	.32	1.18
1.3	154.8	10.17	.29	1.18
1.2	164.8	9.81	.28	1.18
1.2	174.8	8.79	.25	1.17
1.2	184.8	8.39	.24	1.17
1.2	194.8	7.70	.22	1.17
1.2	204.7	6.81	.21	1.17
1.2	214.8	5.98	.18	1.17
1.2	224.7	5.60	.18	1.17
1.2	234.8	4.90	.17	1.17
1.2	244.8	4.25	.15	1.17
1.2	254.7	3.51	.13	1.17
1.2	264.7	2.84	.12	1.17
1.1	274.6	2.055	.098	1.17
1.1	284.5	1.384	.080	1.17
1.1	294.1	.854	.064	1.17
1.6	64.9	18.11	.79	1.26
1.6	74.9	17.17	.62	1.21
1.5	84.8	15.46	.49	1.19
1.5	94.7	14.87	.44	1.19
1.5	104.7	14.34	.40	1.19
1.5	114.9	13.45	.37	1.19
1.5	124.8	12.41	.34	1.19
1.5	134.7	12.10	.29	1.19
1.5	144.9	10.40	.26	1.18
1.5	154.8	9.91	.24	1.18
1.5	164.8	9.05	.22	1.18
1.5	174.9	8.20	.19	1.18
1.5	184.8	7.40	.18	1.18
1.5	194.7	6.68	.17	1.17
1.5	204.8	6.07	.16	1.17
1.4	214.8	5.47	.14	1.17
1.4	224.8	4.76	.13	1.18
1.4	234.7	4.04	.12	1.18
1.4	244.8	3.56	.11	1.18
1.4	254.7	2.883	.095	1.18
1.4	264.7	2.076	.078	1.18
1.3	274.7	1.551	.065	1.18
1.3	284.4	1.114	.055	1.18
1.3	294.2	.551	.037	1.18
2.0	65.2	20.1	1.0	1.27
2.0	74.8	16.57	.70	1.25
2.0	84.9	15.29	.54	1.23
1.9	94.7	14.36	.47	1.22
2.0	104.8	13.74	.41	1.21
1.9	114.8	12.62	.37	1.20
1.9	124.8	11.38	.33	1.19
1.9	134.7	10.07	.29	1.19
1.9	144.8	9.76	.28	1.18
1.9	154.8	8.54	.24	1.18
1.9	164.8	7.88	.22	1.18
1.9	174.7	7.42	.21	1.17
1.9	184.8	6.50	.19	1.17
1.8	194.8	5.78	.17	1.17
1.9	204.8	5.24	.16	1.17
1.8	214.7	4.47	.14	1.17
1.8	224.8	3.97	.13	1.17
1.8	234.7	3.31	.12	1.17
1.8	244.7	2.79	.11	1.17
1.8	254.9	2.174	.092	1.17
1.8	264.5	1.706	.080	1.17
1.7	274.5	1.232	.066	1.17
1.7	284.4	.742	.051	1.17
1.8	294.1	.415	.037	1.17
9.1	64.9	9.65	.35	1.33
9.1	74.6	6.61	.22	1.34
9.1	84.5	4.44	.14	1.29
9.1	94.6	3.11	.10	1.28
9.1	104.5	1.916	.068	1.26
9.1	114.7	1.199	.048	1.25
9.1	124.5	.759	.035	1.25
9.1	134.6	.479	.026	1.25
9.1	144.3	.304	.019	1.26
9.1	154.6	.179	.014	1.27
9.1	164.9	.0948	.0093	1.10
9.1	174.3	.0480	.0063	.97
9.0	184.0	.0136	.0038	.63

Table 8. Data for K^0_S production from copper.

θ	p	σ	Δσ	C(p,θ)	θ	p	σ	Δσ	C(p,θ)
.7	65.2	16.6	2.0	1.16	1.4	224.1	.096	.019	1.12
.6	75.2	11.3	1.2	1.16	1.9	65.3	11.4	1.3	1.16
.6	84.8	8.65	.81	1.16	2.0	75.3	8.65	.81	1.16
.6	95.4	6.42	.53	1.17	2.0	85.1	6.82	.57	1.16
.6	104.4	3.87	.35	1.16	1.9	95.1	7.02	.44	1.17
.6	114.8	4.13	.33	1.15	1.9	104.7	4.55	.31	1.16
.6	124.3	2.99	.26	1.15	1.9	114.9	3.20	.23	1.15
.6	134.9	2.14	.20	1.14	1.9	124.1	2.54	.19	1.15
.6	144.6	1.55	.16	1.14	2.0	135.2	1.64	.14	1.14
.6	154.9	1.43	.14	1.14	1.9	144.9	1.26	.11	1.14
.6	165.2	1.00	.11	1.13	1.9	154.8	1.080	.099	1.14
.6	175.0	.637	.088	1.13	2.0	164.1	.960	.089	1.13
.6	184.4	.490	.075	1.13	1.9	174.4	.597	.067	1.13
.6	194.7	.368	.063	1.13	1.8	184.0	.380	.052	1.13
.5	204.7	.241	.050	1.12	1.8	195.3	.281	.043	1.13
.6	215.1	.240	.048	1.12	1.9	205.6	.243	.039	1.12
.7	65.0	14.3	1.4	1.16	9.1	65.1	6.09	.48	1.32
.8	73.8	10.77	.88	1.16	9.1	74.5	2.95	.22	1.30
.8	85.1	7.35	.56	1.16	9.1	84.5	1.97	.14	1.27
.8	94.5	6.79	.47	1.17	9.1	94.2	1.261	.091	1.26
.8	104.6	5.05	.30	1.16	9.1	104.6	.675	.057	1.25
.8	115.2	3.52	.22	1.15	9.1	114.3	.381	.038	1.24
.8	124.6	3.18	.19	1.15	9.1	125.5	.144	.021	1.24
.8	134.2	2.35	.15	1.14	9.1	134.8	.115	.017	1.23
.8	145.0	1.84	.13	1.14	9.1	143.3	.057	.012	1.23
.8	154.3	1.40	.10	1.14					
.8	164.9	.994	.083	1.13					
.9	174.6	.703	.067	1.13					
.8	184.2	.561	.058	1.13					
.8	194.2	.430	.049	1.13					
.8	203.6	.264	.037	1.12					
.9	213.4	.214	.033	1.12					
.8	224.8	.149	.027	1.12					
.6	235.3	.095	.021	1.12					
1.3	65.2	14.3	1.6	1.16					
1.2	75.2	10.21	.97	1.16					
1.3	84.7	8.32	.70	1.16					
1.2	95.1	6.16	.45	1.17					
1.3	105.0	4.79	.35	1.16					
1.2	114.8	3.89	.28	1.15					
1.3	124.3	3.03	.22	1.15					
1.2	134.7	2.31	.18	1.14					
1.2	144.6	1.55	.14	1.14					
1.2	154.6	1.11	.11	1.14					
1.2	164.1	.99	.10	1.13					
1.2	174.7	.743	.083	1.13					
1.2	185.5	.480	.064	1.13					
1.1	194.6	.355	.054	1.13					
1.2	205.2	.285	.047	1.12					
1.2	214.1	.246	.043	1.12					
1.5	65.0	14.9	1.3	1.16					
1.5	75.1	10.15	.76	1.16					
1.5	85.2	7.92	.54	1.16					
1.5	95.1	6.12	.34	1.17					
1.5	104.4	4.56	.26	1.16					
1.5	115.1	3.36	.19	1.15					
1.5	124.7	2.80	.16	1.15					
1.5	134.6	2.24	.13	1.14					
1.5	144.4	1.395	.097	1.14					
1.5	154.6	1.082	.081	1.14					
1.5	165.1	.947	.073	1.13					
1.5	174.6	.703	.060	1.13					
1.4	184.6	.467	.047	1.13					
1.4	194.3	.301	.036	1.13					
1.5	204.2	.255	.033	1.12					
1.5	213.8	.119	.022	1.12					

Table 9. Data for $\bar{\Lambda}^0$ production from copper.

θ	p	σ	Δσ	C(p,θ)
.6	74.7	1.21	.23	1.24
.7	85.3	.67	.14	1.21
.6	94.6	.475	.098	1.20
.8	104.4	.310	.070	1.19
.9	64.7	2.49	.32	1.26
.9	73.9	1.10	.16	1.24
.8	85.0	.71	.10	1.21
.9	94.9	.579	.078	1.20
.8	104.9	.318	.051	1.19
.8	114.3	.169	.034	1.18
.7	124.5	.124	.027	1.18
1.3	64.0	2.05	.36	1.26
1.2	74.5	1.03	.19	1.24
1.3	85.3	.82	.13	1.21
1.1	95.1	.565	.093	1.20
1.3	105.6	.285	.058	1.19
1.4	113.8	.243	.049	1.18
1.6	64.8	1.90	.25	1.26
1.6	74.9	1.08	.14	1.23
1.6	84.6	.700	.090	1.21
1.5	94.4	.479	.063	1.20
1.6	104.2	.353	.048	1.19
1.5	113.9	.212	.034	1.18
1.6	123.9	.147	.026	1.18
1.6	134.0	.109	.021	1.17
1.9	64.5	1.82	.30	1.26
2.0	73.2	1.58	.22	1.24
2.0	84.8	.76	.12	1.21
1.9	93.7	.478	.078	1.20
2.0	104.8	.338	.058	1.19
1.9	113.7	.158	.036	1.18
9.1	64.5	1.16	.12	1.35
9.2	73.8	.604	.067	1.33
9.2	84.7	.195	.029	1.31
9.1	94.0	.122	.020	1.30

Table 10. Data for Λ^0 production from lead.

θ	p	σ	Δσ	C(p,θ)
.6	64.9	35.8	2.3	1.10
.6	75.0	32.1	1.7	1.11
.6	84.8	29.5	1.4	1.12
.6	94.8	28.9	1.3	1.14
.6	104.9	24.81	.84	1.13
.6	114.8	24.03	.77	1.12
.6	125.0	22.18	.70	1.12
.6	134.8	21.97	.67	1.12
.6	144.8	20.55	.62	1.12
.6	154.7	19.38	.58	1.12
.6	164.9	16.78	.50	1.12
.5	174.8	16.32	.48	1.12
.6	184.8	15.53	.46	1.12
.5	194.8	13.73	.42	1.12
.5	204.7	12.43	.39	1.12
.6	214.8	11.70	.38	1.12
.5	224.8	10.48	.35	1.12
.5	234.8	9.89	.34	1.13
.5	244.8	8.70	.31	1.13
.5	254.8	7.79	.29	1.13
.5	264.6	6.35	.26	1.13
.5	274.6	4.50	.21	1.14
.5	284.3	3.11	.17	1.14
.5	294.4	2.01	.14	1.14
.8	65.1	37.9	2.4	1.10
.8	74.7	35.0	1.9	1.11
.8	84.9	29.6	1.5	1.12
.7	95.0	30.3	1.4	1.14
.7	104.7	27.29	.92	1.13
.7	114.7	24.74	.81	1.12
.7	124.8	23.89	.75	1.12
.7	134.6	21.70	.68	1.12
.7	144.6	19.75	.62	1.12
.7	154.8	18.92	.58	1.12
.7	164.9	17.69	.53	1.12
.7	174.6	16.30	.49	1.12
.7	184.8	15.02	.46	1.12
.7	195.0	12.94	.42	1.12
.7	204.9	12.54	.41	1.12
.7	214.7	11.09	.37	1.12
.7	224.7	10.08	.35	1.12
.7	234.8	9.73	.35	1.13
.6	244.8	8.67	.32	1.13
.7	254.8	7.63	.30	1.13
.6	264.6	5.95	.26	1.13
.6	274.6	4.49	.22	1.14
.6	284.6	2.88	.17	1.14
.6	294.4	1.87	.14	1.14
1.3	65.2	37.2	2.0	1.20
1.3	74.9	35.5	1.5	1.18
1.3	84.8	31.2	1.1	1.16
1.3	94.9	27.62	.94	1.15
1.3	104.8	27.02	.84	1.14
1.2	114.9	24.88	.75	1.13
1.3	124.9	21.87	.65	1.13
1.3	134.7	20.27	.60	1.13
1.2	144.7	19.91	.57	1.12
1.2	154.7	17.97	.52	1.12
1.2	164.7	15.97	.46	1.12
1.2	174.8	14.54	.42	1.11
1.2	184.8	14.12	.40	1.11
1.2	194.7	12.27	.37	1.11
1.2	204.7	11.43	.35	1.11
1.2	214.8	10.08	.31	1.11
1.2	224.9	8.89	.30	1.11
1.2	234.9	7.76	.27	1.11
1.2	244.7	6.62	.25	1.11
1.2	254.6	5.67	.22	1.11
1.2	264.6	4.17	.19	1.11
1.1	274.6	3.54	.17	1.11
1.1	284.5	2.26	.13	1.11
1.1	294.4	1.42	.11	1.11
1.5	65.0	35.9	1.9	1.20
1.6	74.9	33.0	1.4	1.15
1.5	84.8	29.5	1.1	1.13
1.5	94.8	28.33	.98	1.13
1.5	104.8	24.60	.82	1.13
1.5	114.8	23.32	.75	1.12
1.5	124.8	21.24	.67	1.13
1.5	134.7	19.43	.57	1.13
1.5	144.7	17.71	.52	1.12
1.5	154.9	16.76	.49	1.12
1.5	164.8	14.90	.42	1.12
1.5	174.7	13.95	.40	1.12
1.4	184.8	12.09	.36	1.12
1.4	194.8	10.67	.33	1.11
1.4	204.8	10.05	.32	1.11
1.4	214.7	8.82	.28	1.11
1.4	224.9	8.07	.28	1.12
1.4	234.6	6.64	.24	1.12
1.4	244.8	5.79	.22	1.12
1.4	254.7	4.27	.18	1.12
1.4	264.7	3.74	.17	1.12
1.3	274.9	2.37	.13	1.12
1.3	284.4	2.06	.12	1.12
1.3	294.1	1.136	.091	1.12
2.0	65.3	36.0	1.8	1.20
2.0	75.0	32.7	1.3	1.18
2.0	84.9	28.77	.98	1.16
2.0	94.9	26.02	.83	1.15
2.0	104.7	24.41	.73	1.14
1.9	114.7	21.56	.63	1.14
1.9	124.7	19.97	.57	1.13
1.9	134.8	17.93	.51	1.13
1.9	144.7	16.76	.48	1.12
1.9	154.7	14.66	.42	1.12
1.9	164.7	13.77	.39	1.12
1.9	174.7	12.29	.35	1.11
1.9	184.8	10.95	.32	1.11
1.9	194.6	9.41	.29	1.11
1.8	204.7	8.22	.26	1.11
1.9	214.7	7.08	.23	1.11
1.8	224.9	6.23	.22	1.11
1.8	234.8	4.99	.19	1.11
1.8	244.6	4.11	.17	1.11
1.7	254.9	3.39	.15	1.11
1.8	264.5	2.84	.14	1.11
1.7	274.3	1.90	.11	1.11
1.7	284.8	1.255	.087	1.11
1.7	295.0	.643	.062	1.11
3.4	64.8	34.8	1.4	1.17
3.4	74.8	28.83	.97	1.20
3.4	84.7	24.32	.71	1.17
3.4	94.7	21.97	.61	1.16
3.4	104.8	18.77	.50	1.15
3.4	114.8	16.47	.43	1.15
3.3	124.7	14.63	.38	1.14
3.3	134.7	12.51	.33	1.14
3.3	144.9	10.96	.29	1.14
3.3	154.7	9.07	.27	1.14
3.3	164.8	7.19	.21	1.13
3.3	174.6	5.98	.18	1.13
3.3	184.7	5.06	.16	1.12

Table 10. (continued)

θ	p	σ	Δσ	C(p,θ)
3.2	194.7	4.04	.14	1.12
3.2	204.8	3.11	.12	1.11
3.2	214.5	2.45	.10	1.11
3.2	224.7	1.818	.085	1.10
3.2	234.4	1.260	.069	1.09
3.1	244.7	1.019	.061	1.09
3.1	254.6	.698	.050	1.07
3.0	265.1	.476	.040	1.06
3.1	274.6	.249	.028	1.03
3.0	284.5	.194	.025	1.04
3.0	293.9	.082	.016	1.03
5.4	65.1	26.65	.99	1.25
5.3	74.7	23.14	.71	1.29
5.3	84.7	18.10	.50	1.25
5.3	94.6	15.10	.41	1.24
5.3	104.6	12.16	.32	1.23
5.3	114.7	9.49	.26	1.22
5.3	124.5	7.52	.21	1.22
5.3	134.6	5.71	.17	1.21
5.3	144.7	4.56	.14	1.22
5.3	154.6	3.36	.12	1.22
5.3	164.6	2.591	.094	1.20
5.2	174.5	1.590	.069	1.18
5.2	184.5	1.335	.061	1.17
5.2	194.7	.911	.049	1.15
5.1	204.7	.640	.040	1.13
5.2	214.5	.414	.031	1.09
5.2	224.9	.260	.024	1.04
5.1	234.3	.155	.018	.97
5.1	245.2	.058	.011	.77
4.9	254.4	.0372	.0091	.68
5.0	263.4	.0221	.0074	.59
7.3	64.7	25.88	.84	1.28
7.3	74.7	19.98	.56	1.30
7.3	84.6	13.54	.36	1.25
7.3	94.7	10.10	.27	1.24
7.3	104.5	7.39	.20	1.23
7.3	114.7	5.24	.15	1.22
7.3	124.4	3.79	.12	1.22
7.3	134.6	2.500	.088	1.22
7.2	144.6	1.732	.069	1.23
7.3	154.3	1.218	.056	1.23
7.2	164.5	.717	.039	1.16
7.2	174.4	.432	.028	1.12
7.2	184.7	.282	.022	1.07
7.2	194.2	.131	.014	.94
7.1	204.5	.077	.011	.82
7.1	214.9	.0242	.0078	.50
7.2	225.8	.0083	.0072	.26
9.1	64.8	20.40	.64	1.29
9.1	74.7	13.77	.39	1.31
9.0	84.7	8.75	.25	1.25
9.0	94.5	5.94	.17	1.24
9.0	104.5	4.22	.13	1.23
9.0	114.4	2.625	.089	1.21
9.0	124.5	1.774	.066	1.21
9.0	134.4	1.024	.046	1.21
9.0	144.7	.652	.035	1.23
9.0	154.2	.431	.027	1.24
9.0	164.6	.223	.018	1.07
8.9	174.7	.116	.012	.95
8.9	184.6	.0447	.0079	.71
8.8	194.1	.0108	.0065	.32
9.0	205.0	.0009	.0064	.04

Table 11. Data for K_S^0 production from lead.

θ	p	σ	Δσ	C(p,θ)
.6	65.2	22.7	2.9	1.10
.6	75.6	16.8	1.7	1.10
.6	84.6	16.1	1.4	1.10
.6	94.8	13.2	1.1	1.11
.6	104.5	9.47	.70	1.10
.5	114.4	5.85	.49	1.09
.6	124.2	5.03	.41	1.09
.6	134.2	4.40	.36	1.08
.6	144.7	3.21	.29	1.08
.5	154.8	2.36	.23	1.08
.5	164.2	1.96	.20	1.08
.6	174.3	1.55	.17	1.07
.5	184.2	.87	.12	1.07
.6	194.4	.74	.11	1.07
.7	204.9	.343	.074	1.07
.7	65.4	21.8	2.9	1.10
.7	74.6	22.4	2.2	1.10
.8	85.1	13.9	1.3	1.10
.8	94.6	11.5	1.0	1.11
.8	104.5	9.48	.73	1.10
.7	114.6	6.83	.55	1.09
.8	124.3	5.64	.46	1.09
.7	134.2	4.47	.38	1.08
.7	144.6	2.91	.28	1.08
.7	154.0	2.37	.24	1.08
.8	164.3	1.51	.18	1.08
.7	174.0	1.33	.17	1.07
.7	184.4	.85	.13	1.07
.8	195.2	.64	.11	1.07
.8	205.6	.355	.078	1.07
.6	214.0	.409	.082	1.07
1.3	65.1	24.9	2.9	1.10
1.3	75.2	19.1	1.8	1.10
1.3	84.6	16.2	1.3	1.10
1.3	95.1	11.13	.81	1.11
1.3	105.1	8.86	.62	1.10
1.2	114.8	6.03	.46	1.09
1.2	125.1	4.75	.37	1.09
1.2	134.7	4.13	.32	1.08
1.3	144.5	3.42	.27	1.08
1.2	155.1	2.18	.20	1.08
1.2	164.5	1.46	.16	1.08
1.2	174.9	1.08	.13	1.07
1.3	184.5	.86	.11	1.07
1.2	194.4	.593	.092	1.07
1.2	203.8	.435	.077	1.07
1.1	214.5	.277	.059	1.07
1.5	65.3	22.8	2.6	1.10
1.5	75.3	17.9	1.7	1.10
1.6	84.8	15.0	1.2	1.10
1.5	94.8	10.57	.85	1.11
1.5	104.9	7.83	.57	1.10
1.5	114.7	6.49	.47	1.09
1.5	125.1	4.72	.36	1.09
1.5	134.5	3.32	.28	1.08
1.5	145.2	2.41	.22	1.08
1.5	154.9	1.71	.18	1.08
1.5	164.4	1.70	.17	1.08
1.4	174.6	1.13	.13	1.07
1.3	184.3	.628	.095	1.07
1.4	195.7	.552	.086	1.07
1.5	203.0	.330	.065	1.07
1.5	214.2	.278	.058	1.07
2.0	65.0	25.1	2.6	1.10
2.0	74.9	17.3	1.5	1.10
1.9	84.6	15.0	1.2	1.10
2.0	94.9	9.67	.76	1.11
1.9	104.8	7.76	.53	1.10
1.9	114.6	5.99	.41	1.09
2.0	124.3	4.96	.34	1.09
1.9	134.1	3.62	.27	1.08
1.9	144.5	2.36	.20	1.08
2.0	154.7	1.54	.15	1.08
1.9	164.8	1.52	.15	1.08
1.9	174.4	1.11	.12	1.07
1.9	183.9	.592	.085	1.07
1.8	194.0	.392	.067	1.07
1.8	204.3	.288	.056	1.07
3.4	64.5	27.1	2.2	1.19
3.3	74.9	18.8	1.2	1.17
3.4	84.8	14.38	.84	1.14
3.4	94.9	8.61	.53	1.13
3.4	104.6	6.43	.39	1.13
3.4	114.5	4.47	.29	1.12
3.3	124.6	3.35	.23	1.11
3.4	134.5	2.34	.18	1.11
3.3	144.8	1.56	.13	1.10
3.3	154.1	1.05	.10	1.10
3.3	164.5	.624	.075	1.09
3.3	174.3	.481	.058	1.08
3.2	183.6	.323	.050	1.08
3.2	194.1	.181	.036	1.07
3.3	204.2	.159	.033	1.07
5.4	64.6	18.7	1.4	1.27
5.3	75.3	12.57	.80	1.25
5.3	84.9	9.78	.56	1.22
5.3	95.0	6.00	.35	1.21
5.3	104.2	3.99	.25	1.20
5.3	114.9	2.45	.17	1.19
5.3	125.0	1.91	.14	1.19
5.3	135.0	.951	.087	1.19
5.3	144.3	.685	.070	1.18
5.3	155.2	.312	.044	1.18
5.2	165.5	.291	.040	1.15
5.4	174.9	.163	.029	1.14
7.3	64.7	18.1	1.2	1.28
7.3	74.7	10.95	.64	1.26
7.3	84.7	7.00	.39	1.23
7.3	95.1	3.87	.23	1.22
7.3	104.6	2.60	.16	1.21
7.3	114.3	1.54	.11	1.21
7.2	125.0	.781	.071	1.20
7.3	134.2	.594	.057	1.20
7.3	144.2	.242	.034	1.19
7.2	154.3	.173	.027	1.19
7.2	164.3	.087	.018	1.11
9.0	65.1	12.45	.84	1.28
9.0	74.7	8.00	.47	1.26
9.0	84.8	4.75	.27	1.24
9.0	94.4	2.63	.16	1.23
9.0	104.8	1.57	.11	1.22
9.0	114.1	.817	.068	1.21
9.0	125.1	.354	.040	1.20
9.0	134.4	.209	.029	1.20
9.0	144.3	.111	.019	1.20
8.8	154.1	.067	.014	1.19

Table 12. Data for $\bar{\Lambda}^0$ production from lead.

θ	p	σ	Δσ	C(p,θ)
.6	64.3	3.64	.68	1.19
.6	74.5	2.22	.40	1.17
.6	84.3	1.64	.27	1.15
.6	94.8	1.19	.20	1.14
.5	104.2	.73	.14	1.13
.8	66.0	2.98	.61	1.19
.7	74.7	3.94	.55	1.17
.8	85.1	1.87	.30	1.15
.8	93.5	.75	.16	1.14
.7	104.5	.90	.16	1.13
1.4	65.0	4.18	.66	1.19
1.4	74.5	3.02	.43	1.17
1.4	85.8	1.19	.21	1.15
1.3	93.9	.95	.16	1.14
1.2	105.2	.52	.10	1.13
1.1	114.0	.508	.094	1.12
1.5	64.8	4.43	.67	1.19
1.5	74.6	2.00	.34	1.17
1.5	84.8	1.57	.24	1.15
1.6	93.4	.95	.16	1.14
1.4	105.3	.50	.10	1.13
1.6	114.5	.370	.078	1.12
1.9	63.9	4.81	.66	1.19
1.9	74.5	2.30	.34	1.17
2.2	85.2	1.42	.21	1.15
2.0	94.8	.85	.14	1.14
1.9	103.9	.75	.11	1.13
1.8	113.6	.360	.072	1.12
1.8	122.7	.291	.060	1.12
3.5	64.7	4.13	.49	1.22
3.5	74.3	2.02	.26	1.20
3.4	84.6	1.29	.16	1.18
3.4	94.3	.70	.10	1.17
3.4	104.3	.480	.074	1.16
5.4	65.4	3.10	.33	1.30
5.4	74.6	1.94	.21	1.28
5.4	84.7	1.00	.12	1.26
5.4	94.8	.577	.074	1.25
5.3	104.4	.277	.045	1.24
5.3	114.7	.148	.030	1.23
5.3	124.7	.109	.024	1.22
7.3	65.4	2.65	.26	1.31
7.3	74.4	1.65	.16	1.29
7.3	84.5	.852	.089	1.27
7.3	93.8	.367	.049	1.26
7.2	104.4	.208	.032	1.25
7.2	114.0	.146	.024	1.24
9.1	64.3	2.30	.21	1.32
8.9	74.5	1.08	.11	1.30
9.1	84.4	.657	.067	1.28
9.0	94.2	.233	.033	1.26
9.0	104.7	.130	.022	1.25
9.1	113.4	.061	.013	1.24

REFERENCES

1. C. Quigg and J. L. Rosner, Phys. Rev. D14, 160 (1976).
2. C. Geweniger et al., Phys. Lett. 57B, 193 (1975).
3. S. Gjesdal et al., Phys. Lett. 40B, 152 (1972).
4. F. Eisele et al., Phys. Lett. 60B, 297 (1976).
5. F. Dydak et al., Nucl. Phys. B118, 1 (1977).
6. G. Zech et al., submitted to Nucl. Phys.
7. V. Hungerbuhler et al., Phys. Rev. D12, 1203 (1975).
8. V. Hungerbuhler et al., Phys. Rev. D10, 2051 (1974).
9. V. Hungerbuhler et al., Phys. Rev. Lett. 30, 1234 (1973).
10. J. Badier et al., Phys. Lett. 39B, 414 (1972).
11. R. Majka et al., Phys. Rev. Lett. 37, 413 (1976).
12. J. J. Blaising et al., Phys. Lett. 58B, 121 (1975).
13. J. Badier et al., Phys. Lett. 41B, 387 (1972).
14. W. Tanenbaum et al., Phys. Rev. D12, 1871 (1975).
15. W. Tanenbaum et al., Phys. Rev. Lett. 33, 175 (1974).
16. D. Decamp, Phys. Lett. 66B, 295 (1977).
17. D. Horn, Phys. Reports 4C, 1 (1972); and references contained therein.
18. W. Busza et al., Phys Rev. Lett. 34, 836 (1975).
19. Fishbane and Trefil, Phys. Rev. D3, 238 (1971).
20. K. Gottfried, Phys. Rev. Lett. 32, 957 (1974).

21. P. Fishbane and J. Trefil, Phys. Lett. 51B, 139 (1974).

22. J. Dias De Deus, Nucl. Phys. B10, 146 (1976).

23. H. Fukushima, Nuovo Cimento 34A, 445 (1976).

24. J. W. Cronin et al., Phys. Rev. D11, 3105 (1975).

25. R. P. Feynman, Phys. Rev. Lett. 23, 1415 (1969).

26. U. Amaldi et al., Nucl. Phys. B86, 403 (1975).

27. H. A. Kastrup, Phys. Rev. 147, 1130 (1966); E. W. Anderson and G. B. Collins, Phys. Rev. Lett. 19, 201 (1967); G. Mack, Phys. Lett. 26B, 515 (1968).

28. E. Fermi, Phys. Rev. 81, 683 (1951); 92, 452 (1953); 93, 1434 (1954).

29. R. Hagedorn, Nuovo Cimento Suppl.3, 147, (1965); R. Hagedorn and J. Ranft, Nuovo Cimento Suppl.6, 169 (1968); J. Ranft, Phys. Lett. 31B, 529 (1970); R. Hagedorn, Nucl. Phys. B24, 93 (1970).

30. S. Z. Belenkji and L. D. Landau, Nuovo Cimento Suppl.3, 15 (1956).

31. P. Carruthers and Minh Duong Van, Phys. Lett. 41B, 597 (1972); Phys. Rev. D8, 859 (1973).

32. D. Amati et al., Nuovo Cimento 26, 896 (1962); C. Risk and J. H. Friedman, Phys. Rev. Lett. 27, 353 (1971).

33. D. Silverman and C. I. Tan, Phys. Rev. D2, 233 (1970); T. T. Chou, Phys. Rev. Lett. 27, 1247 (1971); Phi Salin and G. H. Thomas, Nucl. Phys. B38, 375 (1972).

34. A. H. Mueller, Phys. Rev. D2, 2963 (1972).

35. K. Fialkowski, Phys. Lett. 41B, 379 (1972); K. Fialkowski and H. Miettinen, Phys. Lett. 43B, 61 (1973).

36. R. K. Adair, Phys. Rev. D5, 1105 (1972).

37. H. Cheng and T. T. Wu, Phys. Rev. Lett. 24, 1456 (1970).

38. V. V. Anisovich et al., Nucl. Phys. B55, 474 (1973); J. Kogut and L. Susskind, Phys. Reports 8, 76 (1973).

39. C. E. Detar et al., Phys. Rev. Lett. 26, 675 (1971).

40. Particle Data Group, Phys. Lett. 50B, 1 (1974).

41. D. J. Mellema and A V. Tollestrup, CSTL internal Report (1973).

42. E. F. Clayton et al., Nucl. Phys. B95, 1305 (1975).

43. Particle Data Group, Rev. Mod. Phys. 48, 574 (1976).

44. S. P. Denisov et al., Nucl. Phys. B61, 62 (1973).

45. Grote, Hagedorn, and Ranft, Atlas of Particle Spectra, CERN, (1970).

46. J. Whitmore, Phys. Reports 10C, 273 (1974).

47. Whitmore et al., Phys. Rev. D11, 3124 (1975).

48. V. Blobel et al., DESY 73/36 (1973); V. Blobel et al., Nucl. Phys. B69, 454 (1974).

49. H. Boggild et al., Nucl. Phys. B57, 77 (1973).

50. G. Charlton et al., Phys. Rev. Lett. 30, 574 (1973); 29, 1759 (1972).

51. F. Dao et al., Phys. Rev. Lett. 30, 1151 (1973).

52. A. Sheng et al., Phys. Rev. D11, 1733 (1975).

53. J. Chapman et al., Phys. Lett. 47B, 465 (1973).

54. G. Bunce et al., Phys. Rev. Lett. 36, 1113 (1976).

55. O. Overseth and R. Roth, Phys. Rev. Lett. 19, 319 (1967).

56. K. Heller et al., submitted to Phys. Lett.

57. T. Devlin et al., submitted to Nucl. Phys.

58. K. Alpgard et al., Nucl. Phys. B105, 349 (1976).

59. K. J. M. Moriarty et al., Lett. Nuovo Cimento 17, 366 (1976).